ALMA MATER STUDIORUM
UNIVERSITÀ DI BOLOGNA

DOTTORATO DI RICERCA IN

NANOSCIENZE PER LA MEDICINA E PER L'AMBIENTE

Ciclo 38

**Settore Concorsuale:** 03/A1 - CHIMICA ANALITICA

**Settore Scientifico Disciplinare:** CHIM/01 - CHIMICA ANALITICA

# BIOANALYTICAL TECHNOLOGIES EMPLOYING LUMINESCENCE FOR ASTROBIOLOGY, FOOD SAFETY, AND CLINICAL APPLICATIONS

**Presentata da:** Elisa Lazzarini

**Coordinatore Dottorato**

Matteo Calvaresi

**Supervisore**

Mara Mirasoli

**Co-supervisore**

Donato Calabria

Esame finale anno 2026

# *Abstract*

This Ph.D. research investigates the design and development of advanced biosensor technologies for applications in clinical diagnostics, food safety, and space exploration. The work focuses on integrating biosensing systems with innovative fabrication techniques, such as wax printing, 3D printing, and paper-based microfluidics, to create sustainable and high-performance Point-of-Care (POC) devices enabling rapid and decentralized analysis.

A 3D-printed electrochemical ECL biosensor was developed for glucose detection using a luminol/$H_2O_2$ system and carbon black-doped PLA electrodes. The device operates with a 1.5 V battery and is readable via smartphone. The incorporation of glucose oxidase within an agarose hydrogel enabled the fabrication of preloaded, ready-to-use sensors that required only sample addition. The biosensor demonstrated effective glucose detection and promising potential for real sample analysis, highlighting the flexibility of 3D-printed electrochemical platforms.

To enable accurate microbial monitoring in water, a DNA-based aptamer biosensor for ATP detection was also developed. In this system, ATP binding activates a catalytic DNAzyme, generating a chemiluminescent signal. Integration into origami microfluidic paper-based devices (μPADs) allowed portable, on-paper detection suitable for POC applications.

The research further explores type III CRISPR–Cas systems as RNA-guided diagnostic platforms. A chemiluminescent assay was designed in which Csx1 RNase activation degrades a G-quadruplex (G4) RNA probe, reducing the luminol/$H_2O_2$-based signal and enabling sensitive, equipment-free nucleic acid detection.

Finally, within the BOREALIS project (Biofilm Onboard Radiation Exposure Assessment Lab In Space), supported by the Italian Space Agency, microfluidic lab-on-chip systems were optimized for controlled biofilm growth under space conditions.

Overall, this work demonstrates how innovative fabrication methods and molecular sensing strategies can converge to produce next-generation biosensors for healthcare, food security, and astrobiological research.

# *Contents*

# *Chapter 1*

## *Introduction*

## 1.1 Introduction to biosensors

Biosensors lie at the dynamic intersection of biology, chemistry, physics, material sciences and engineering, representing a cornerstone of multidisciplinary innovation [1]. Designed as efficient, cost-effective alternatives to traditional analytical techniques, such as spectrophotometry and chromatography, these devices enable both qualitative and quantitative measurements without the need for complex laboratory equipment [2], [3]. Broadly defined, a sensor detects changes in physical parameters (e.g., temperature, pressure, motion, or electrical signals) and converts them into readable outputs [4]. Sensors are categorized based on factors such as power source (active/passive), interaction type (contact/non-contact), signal output (analog/digital), and the property measured [5], [6]. Within this diverse group, biosensors, a term introduced by Cammann [7] and standardized by IUPAC (International Union of Pure and Applied Chemistry) [8], [9], constitute a distinct class that leverages biological components for detection. Their origins date back to the 1960s, when Leland C. Clark developed the first enzyme-based electrodes for measuring oxygen and hydrogen peroxide, pioneering glucose sensing technology [10]. In particular, a biosensor is a concise analytical tool or probe, visually depicted in Figure 1.1, consisting of three principal components: a biological recognition element (e.g., enzyme, antibody, or nucleic acid), a transducer, which converts the biological interaction into a signal, and an electronic system which quantifies and interprets the signal. The biological recognition element specifically binds the target molecule, initiating the generation of a measurable signal through the transducer. This signal is then converted into a quantifiable output by the electronic component [11].

This process allows biosensors to detect even trace amounts of chemical and biological substances in complex samples with high sensitivity and selectivity, making them essential for a variety of applications.

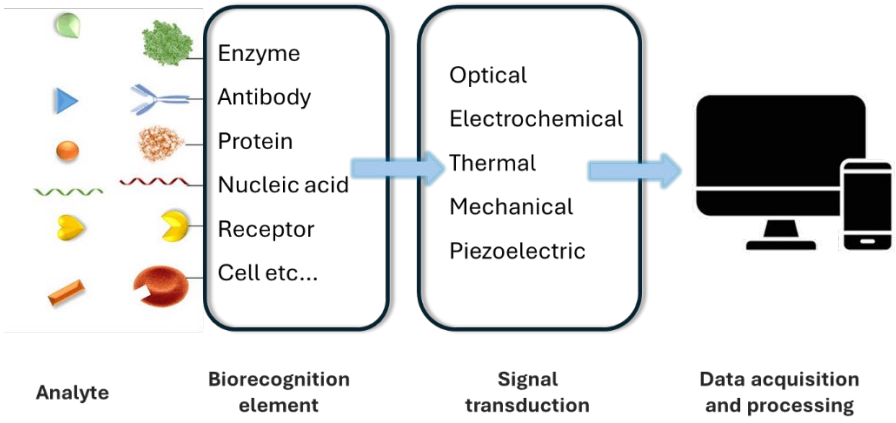


***Figure 1.1.*** *Schematic representation of biosensor components.*

To ensure optimal performance, biosensors must meet several critical criteria:

- Selectivity, the ability to identify a specific analyte despite the presence of interfering substances, also in complex samples [12].
- Sensitivity, defined by detection limits and the signal-to-concentration relationship, ensuring accurate quantification across a wide range [13].
- Specificity, the capacity to distinguish the target analyte from structurally similar compounds, such as metabolites or isomers [12].
- Short response time, because rapid detection is vital, especially in point-of-care or screening applications.
- Reproducibility, consistent performance across repeated tests [14].
- Stability, the resistance to degradation over time or under varying environmental conditions, crucial for continuous monitoring. Factors such as bioreceptor affinity and long-term integrity influence this parameter [11], [15].
- Portability, to make them suitable to be used outside the traditional laboratory settings. This feature is also related to the miniaturization of the system and makes it capable of providing rapid results without the need for sophisticated equipment or trained personnel [16].
- Linearity, related to the accuracy of the measured response, providing a proportional response over a specific range of analyte concentrations [17].

One of the greatest advantages of biosensors is their accessibility. Their ease of use, portability, and reliability make them ideal even for non-experts in field applications, bypassing the logistical challenges of sample transport and lab-based analysis. As a result, biosensors are widely applied across multiple sectors such as in medical diagnostics where they offer fast, accurate disease detection, glucose monitoring, and biomarker identification, empowering patients and enhancing healthcare delivery [18]. In environmental monitoring for example, biosensors detect pollutants and toxins in air, water, and soil, enabling timely interventions. In food industry they ensure safety by identifying spoilage indicators and contaminants and in pharmaceutical and industrial settings they support process control and product quality [19].

Recent advances have also seen the integration of biosensors with smartphones, merging diagnostic capabilities with digital technologies. These smartphone-enabled platforms leverage mobile computing power and connectivity to deliver fast, affordable, and user-friendly diagnostics [20], [21].

Key advantages include:

- Broader accessibility to underserved populations,
- Portability, ideal for point-of-care or remote monitoring,
- Affordability and intuitive operation via familiar interfaces,
- Connectivity for real-time data sharing with healthcare providers or databases [22], [23].

### 1.1.1 Enzymatic biosensors

Enzymatic biosensors are among the most extensively used classes of biosensors, owing to their high specificity, sensitivity, and versatility in detecting a wide range of analytes. Their popularity is further enhanced by the ease of production and low manufacturing costs. These advantages have led to their widespread application in fields such as medical diagnostics, food safety, environmental monitoring, and industrial process control [24].

Enzyme-based biosensors utilize enzymes as biological recognition elements, capable of binding to and interacting with target analytes through their natural catalytic activity. As biological catalysts, enzymes accelerate biochemical reactions by lowering the activation energy required to reach the transition state, thereby facilitating product formation [25]. For biosensing purposes, enzymes can be isolated from living cells and immobilized on sensor surfaces. Crucially, they participate in reactions without being consumed, allowing for reuse in repeated analyses.

The immobilization strategy is crucial and must be tailored to the specific enzyme to avoid compromising its structure, activity, or stability. Improper immobilization can limit both sensor performance and enzyme reusability. In addition, several other strategies are used to enhance the stability and ensures safe and effective long-term use, including protein engineering [26], the use of naturally thermostable microbial enzymes [27], [28], and the addition of stabilizing agents [29].

Each enzyme contains a catalytic (active) site where specific substrates bind, forming a transient enzyme-substrate complex. This intermediate is converted into a product molecule through the enzyme’s catalytic action. The catalytic site is typically stabilized by a structural protein unit, which creates a favorable microenvironment for substrate interaction.

In some cases, enzymes may also require non-protein components known as cofactors, either organic or inorganic molecules, that are essential for their full catalytic activity [30].

Environmental factors such as pH, temperature, and reactant concentration significantly influence enzymatic reaction rates. The kinetics of these reactions are most commonly described by the Michaelis-Menten model, which assumes that the enzyme-substrate complex can either proceed to product formation or dissociate back into its original components [31]. The model is represented by the equation:

$$V = \frac{Vmax\ [S]}{Km + [S]}$$

Where $V$ is the reaction rate of an enzyme-catalyzed reaction; $Vmax$ is the maximum reaction rate at saturating substrate concentrations; [S] is the substrate concentration; $Km$ is the Michaelis–Menten constant, defined as the substrate concentration at half of $v_{max}$.

The $K_m$ value provides insights into the enzyme's affinity for its substrate and is influenced by the presence of inhibitors. Enzyme activity can be diminished by these substances, which are classified as either reversible or irreversible inhibitors. Reversible inhibitors bind temporarily to enzymes and include competitive, non-competitive, and uncompetitive types. Competitive inhibitors bind to the active site, directly competing with the substrate, thereby increasing $K_m$ as more substrate is needed to reach saturation. Non-competitive inhibitors bind to a site other than the active site, altering the enzyme's conformation and reducing its catalytic efficiency. In this case, $v_{max}$ decreases while $K_m$ remains unchanged. Uncompetitive inhibitors, which are less common, bind only to the enzyme-substrate complex, stabilizing it and decreasing both $v_{max}$ and $K_m$. Their effect becomes more significant at high substrate concentrations. In contrast, irreversible inhibitors bind covalently to the enzyme, often at the active site, permanently altering its structure and rendering it catalytically inactive. These are often referred to as poisons due to their potent and lasting toxic effects [32].

From an analytical perspective, enzyme-based biosensors offer significant advantages: they allow for rapid, accurate chemical analyses with high substrate specificity, enabling detection at very low concentrations using minimal sample volumes, thereby conserving reagents. Enzymes also enhance the selectivity of chemiluminescent (CL) and electrochemiluminescent (ECL) detection methods. To expand the range of detectable molecules, cascade systems of coupled enzymes can be constructed. In these systems, the initial analyte is enzymatically converted into a product, which is then further transformed by additional enzymes into a measurable compound [33].

Commonly used enzymes in this context include oxidases such as glucose oxidase and xanthine oxidase, which generate hydrogen peroxide ($H_2O_2$) [34], [35]. Moreover, enzyme-based biosensors are capable of detecting either the catalysis or inhibition of enzymatic activity by a target analyte, through the measurement of species generated or consumed in the reaction. These biosensors may involve a single enzyme or a cascade of enzymatic reactions [12].

A landmark in enzyme biosensing was the development of the first glucose enzymatic biosensor by Dr. Leland Clark [36]. Since then, glucose biosensors have become a cornerstone of biosensing technology, particularly in the medical and environmental sectors. In 2021, Abbott launched the FreeStyle Libre 3, a real-time continuous glucose monitoring (CGM) system that delivers automatic, minute-by-minute glucose readings directly to a smartphone. This wearable device, worn on the upper arm for up to 14 days, is factory-calibrated and does not require fingerstick validation, offering a discreet and user-friendly solution for glucose monitoring [37].

These glucose biosensors rely on glucose oxidase (GO), a glycoprotein notable for its water dispersibility and high stability, making it ideal for continuous glucose monitoring. GO catalyzes the oxidation of β-D-glucose to D-glucono-δ-lactone and hydrogen peroxide ($H_2O_2$) in the presence of oxygen (Figure 1.2). It can be derived from various fungal or bacterial sources, including industrial strains engineered for improved activity and stability. For expanded functionality, the GO reaction is often coupled with other enzymes in modern applications. In the medical field, GO is used in innovative cancer nanotherapies by creating hypoxic, ROS-rich environments [38]. In the food industry, it supports wine analysis when combined with enzymes and gold nanoparticles, showcasing its versatility [39].

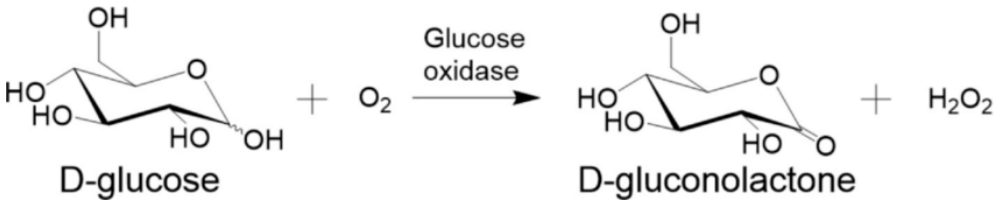


***Figure 1.2.*** *Oxidation reaction of glucose catalyzed by glucose oxidase.*

## 1.2 Immobilization methods in biosensors

Immobilization not only ensures close proximity between the biomolecule (enzymes, antibodies, nucleic acids, etc.) and the transducer, but also enhances the stability of the biomolecule, allowing for repeated use of the biosensor. Biomolecules can be immobilized either directly onto the transducer surface or onto supporting materials that are subsequently attached to the transducer [40]. During the immobilization process, ensuring that the active site of the biomolecule remains accessible to its target is a primary concern, alongside maintaining its conformational stability and biological activity. An effective immobilization method must be rapid, efficient, and should prevent leaching of the biomolecule from the support. The most suitable technique should be chosen according to the biomolecule, the supporting material and/or transducer, the properties of the target molecule, and the physicochemical environment. Biomolecules can be immobilized via direct or indirect methods [11], [41]. Direct immobilization involves physical or chemical attachment of the biomolecule onto the transducer's surface, whereas indirect immobilization employs support matrices or carriers (such as nanoparticles, polymers, or membranes) that are anchored onto the transducer and subsequently loaded with biomolecules. Indirect methods often enhance surface area and biocompatibility, facilitating higher loading capacity and improved sensor performance.

Several immobilization strategies are commonly utilized (Figure 1.3):

- Physical adsorption exploits weak intermolecular forces (electrostatic interactions, hydrogen bonding, hydrophobic interactions, van der Waals forces) to anchor biomolecules. While this method is straightforward and preserves molecular structure, it often results in weak and reversible binding, causing potential leaching and sensor instability during repeated use.
- Covalent bonding creates stable chemical linkages between functional groups on biomolecules (e.g., amine, carboxyl, thiol groups) and activated groups on the transducer or support (such as carboxyl, aldehyde, or epoxy groups). This strong attachment improves sensor durability and reduces biomolecule leaching but may risk partial loss of bioactivity due to chemical modification or steric hindrance.
- Entrapment involves physically enclosing biomolecules within porous matrices (such as hydrogels, sol-gels, or polymer networks). This provides a protective microenvironment enhancing biomolecule stability and activity but can introduce diffusion barriers for analyte molecules, potentially affecting sensor response time and sensitivity.

- Cross-linking employs bifunctional reagents (e.g., glutaraldehyde) to form intermolecular bridges between biomolecules or between biomolecules and supports. This approach enhances structural rigidity and operational stability but must be carefully controlled to avoid excessive cross-linking, which can reduce biomolecular flexibility and activity.
- Affinity exploits specific interactions, such as (strept)avidin-biotin or lectin-sugar, to achieve site-specific, oriented enzyme immobilization for enhanced biosensor performance.

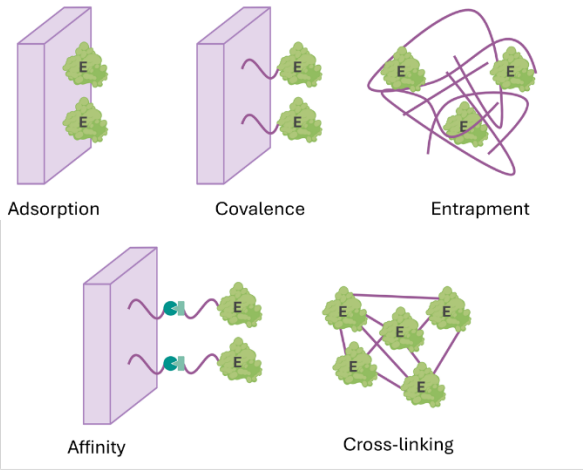


***Figure 1.3.*** *Schematic representation of common immobilization techniques in the biosensing field.*

Beyond immobilization methods, the choice of support materials plays a pivotal role. Nanomaterials such as gold nanoparticles, carbon nanotubes, graphene oxide, and conductive polymers are frequently employed to improve electron transfer kinetics and provide large surface areas for biomolecule loading. Additionally, biocompatible hydrogels and membranes can maintain a favorable microenvironment, preserving the three-dimensional structure and functionality of the immobilized biomolecules [42].

Optimizing immobilization protocols involves balancing several factors, including biomolecule orientation, density, stability, and accessibility of active sites, all of which affect the biosensor's analytical performance. Advanced characterization techniques such as atomic force microscopy (AFM), surface plasmon resonance (SPR), quartz crystal microbalance (QCM), and electrochemical impedance spectroscopy (EIS) are routinely applied to evaluate immobilization quality and sensor surface properties [43].

Another widely adopted technique is the use of self-assembled monolayers (SAMs), a simple yet effective method that enables precise control over the composition, orientation, and surface density of immobilized biomolecules [44].

In the context of enzymes, various advanced immobilization techniques have been developed to address denaturation and poor storage stability. Common approaches such as freeze-drying (lyophilization) and physical adsorption are effective in maintaining enzymatic structure, while the use of stabilizing additives during lyophilization can further improve activity and durability [45].

In conclusion, effective biomolecule immobilization is essential for developing robust, sensitive, and selective biosensors. Continuous advances in immobilization chemistry and nanomaterials are enabling the creation of next-generation biosensors with enhanced performance for applications in clinical diagnostics, environmental monitoring, and food safety.

## 1.3 Paper and Hydrogel: Suitable Materials for Bioassays

### 1.3.1 Paper in biosensing

In the context of sustainable innovation, the design of rapid detection tools increasingly demands a careful balance between technological advancement and environmental responsibility. Achieving this balance involves embracing green design principles, such as simplified sample pre-treatment, device miniaturization for on-site applications, simultaneous detection of multiple analytes, and significant reductions in sample volume, reagent toxicity, and waste generation. These eco-conscious strategies are essential for developing next-generation analytical devices that are not only efficient and portable but also aligned with global sustainability goals [46].

With respect to this, paper has gained significant attention in analytical and clinical chemistry due to its numerous advantages, including low cost, simple fabrication, flexible substrate properties, rapid response time, and minimal consumption of samples and reagents [47]. Moreover, the waste generated from the analysis is minimal, offering advantages in the sampling process as well as in waste management and disposal.

Paper is a porous, hydrophilic, and lightweight material. As a fibrous substrate, it is flexible and can be easily modified to create patterns of varying complexity, depending on the specific biosensor application. Its porosity enables fluid absorption and transport through capillary action, eliminating the need for external power sources or pumping systems. This property is particularly advantageous for use in lateral flow assays (LFAs) and microfluidic paper-based analytical devices (μPADs), where the capillary-driven movement of the analyte through the paper matrix is essential for successful detection [48].

Additionally, the intrinsic porosity of paper facilitates efficient reagent storage. Typically, a few microliters of the analytical reagents are deposited onto the porous matrix, where they are immobilized via van der Waals interactions, hydrogen bonding, or covalent attachment through surface engineering. This strategy enables the fabrication of reagent-free PAD-based (bio)sensors, which are pre-loaded with the necessary reagents and ready for target analyte detection without the need for additional reagent addition during analysis.

A variety of techniques and processes, ranging from chemical modification to physical deposition, can be employed to tailor the intrinsic properties of paper, rendering it suitable for further functionalization or direct use in various applications. Several methods have been reported in the literature for confining liquids to defined regions on paper substrates. These include photolithography, inkjet printing, etching, plasma treatment, mechanical cutting, wax printing, screen printing, and laser processing.

From a technical perspective, paper can be easily cut and folded, enabling the creation of various sensor configurations. The incorporation of origami (paper folding) and kirigami (paper cutting) techniques in the fabrication of microfluidic paper-based analytical devices (μPADs) has enabled the development of three-dimensional (3D) paper-based systems. These innovative configurations offer high application flexibility and make it possible to perform complex, multistep analytical procedures, including complete immunoassays, entirely on paper.

Various types of paper materials can be employed in the design of biosensing devices, enabling customization according to the specific requirements of the intended application [49]. The most commonly used renewable paper-based substrates, such as filter paper, blotting paper, glossy paper, office paper, and nitrocellulose (NC) membranes, are typically derived from cellulose sources like wood or cotton, processed through compression and chemical treatment of cellulosic fibers. Filter paper, the most widely used substrate due to its excellent wicking ability, uniform thickness, and high reagent absorption. For instance, Whatman grade 1 (pore size ~11 μm) is valued for capillary flow, while grade 4 (pore size ~25 μm) suits applications requiring higher retention. Alternatively, nitrocellulose (NC) membranes is preferred for lateral flow assays due to their high protein-binding capacity [50]. Produced via cellulose nitration, NC allows for strong biomolecule immobilization but is more fragile and unsuitable for wax printing. Popular types include HF-90, HF-135, and HF-180, differing in porosity and pore size. Paper-based biosensing systems have been developed for the detection of glucose [51], cholesterol [52], proteins, and cancer biomarkers, offering rapid, accessible, and non-invasive diagnostic tools [53].

In environmental monitoring, paper-based sensors have been effectively employed to detect contaminants in water, soil, and air, including heavy metals, pesticides, toxins, and microbial pathogens [54], [55]. Likewise, in the food industry, these sensors play a crucial role in monitoring food freshness and detecting chemical residues or pathogenic contamination, thus ensuring product quality and safety throughout the supply chain.

### 1.3.2 Hydrogels in biosensing

Over the past few years, hydrogels, a class of materials characterized by their high water content and three-dimensional network structure, have emerged as versatile and indispensable tools in the field of biosensing. Their ability to incorporate foreign substances while maintaining a favorable environment for biosensing events makes them particularly valuable [56]. These remarkable materials offer a unique combination of biocompatibility, tunable physical properties, and the capacity to absorb and release water, rendering them ideal for a wide range of biosensing applications.

Hydrogels consist of hydrophilic polymer networks capable of retaining substantial amounts of water, which grants them a soft and flexible nature, similar to that of natural tissues. This property makes them especially suitable for various biological applications and helps preserve the native structure of biomolecules, an essential prerequisite for achieving feasibility, specificity, and sensitivity in biosensing [57].

These polymers can be either synthetic or derived from natural sources, such as collagen, hyaluronic acid, or alginate, providing researchers with a wide variety of options to tailor hydrogel formulations for specific biosensing requirements [58].

The fundamental characteristics of hydrogels highlight their exceptional suitability for biosensing applications. These materials are inherently biocompatible, meaning they are well-tolerated by living organisms, a vital feature that reduces the risk of adverse reactions when hydrogels come into contact with biological samples or tissues [59].

Additionally, their high water content closely resembles the natural environment of cells and biological fluids, enabling efficient analyte exchange between the hydrogel and its surroundings. This capability is particularly important in biosensing, where precise control of the microenvironment is often critical [57]. Furthermore, the three-dimensional porous structure of hydrogels allows for easy functionalization with various recognition elements, such as antibodies, enzymes, or DNA

probes. This property facilitates the selective detection of specific analytes, resulting in biosensors that are both highly specific and sensitive [42].

The versatility of hydrogels is evident in the wide range of applications reported in the literature. For example, hydrogel-based glucose sensors incorporate glucose oxidase enzymes within the hydrogel matrix to detect fluctuations in glucose concentration [60]. Other applications include the monitoring of pH and ion concentrations in biological fluids, which are valuable in both environmental and healthcare contexts [61]. Hydrogels are also employed in embedded biosensors designed for controlled drug delivery, where drugs are released in response to specific stimuli such as changes in pH or temperature [62]. Moreover, hydrogels functionalized with antibodies or aptamers enable the detection of specific proteins or biomarkers in complex biological samples, serving important diagnostic and biomedical functions. In recent years, hydrogel-based wearable sensors have gained prominence for their ability to continuously monitor various physiological parameters, including hydration levels and lactate concentrations, among others.

In conclusion, hydrogels represent outstanding functional materials for the development of biosensors. Nonetheless, despite their significant advancements in biosensing applications, several challenges remain, including issues related to stability, long-term performance, and integration into miniaturized devices. Researchers are actively addressing these challenges by refining hydrogel formulations, investigating novel functionalization methods, and designing innovative sensor architectures.

## 1.4 Functional Nucleic Acids (FNA)

Functional nucleic acids (FNAs), especially DNA aptamers and DNA-based synthetic enzymes (DNAzymes), have been widely explored as key elements in biosensor development due to their distinctive properties. FNAs are nucleic acid molecules that exhibit ligand-binding and/or catalytic functions, and can be categorized as either natural or synthetic. Natural FNAs include RNA enzymes (ribozymes) and regulatory RNA elements (riboswitches), while synthetic FNAs comprise ribozymes, DNAzymes, and both DNA and RNA aptamers. FNAs are emerging as essential components in point-of-care (POC) biosensors, owing to their unique advantages such as high binding affinity and specificity, outstanding chemical stability, ease of synthesis and modification, and compatibility with several signal amplification and transduction mechanisms [63].

Aptamers are short strands of DNA or RNA, typically ranging from 25 to 100 nucleobases, that are selected in vitro from a combinatorial library using the SELEX process (Systematic Evolution of Ligands by EXponential enrichment). Once selected, these aptamers demonstrate high specificity and selectivity toward their target molecules, often exhibiting strong binding affinities with dissociation constants ($K_D$) in the nanomolar to picomolar range [64].

Compared to antibodies, aptamers offer several significant advantages. They are thermally and chemically stable and can be easily synthesized chemically. This synthetic accessibility enables the introduction of a variety of functional groups, such as electrochemical or fluorescent labels, or surface-grafting moieties, in a regioselective manner, adding versatility and functionality to their use in biosensors [65].

One of the most fascinating characteristics of aptamers is their ability to undergo conformational changes upon binding to their target. These structural shifts can lead to the formation of well-defined three-dimensional (3D) secondary structures, such as loops, G-quadruplexes (G4), or kissing hairpins, all of which can be exploited for signal transduction purposes [66].

Among these, G-quadruplex structures are particularly noteworthy. They are formed by the folding of guanine-rich sequences into stacked tetrads of Hoogsteen hydrogen-bonded guanine bases, stabilized by various loop-forming segments. Due to their structural polymorphism, including parallel, antiparallel, and hybrid topologies, G4 structures have become increasingly popular in the design of aptamer-based biosensors, or aptasensors [67].

An increasing number of aptamers are known to form G-quadruplex (G4) structures upon target binding, making them highly effective for the detection of a broad range of biological targets. G4-based aptasensors have been successfully applied to identify various macromolecules, including proteins such as thrombin, growth factors, insulin, and cancer biomarkers, as well as complex biological entities like exosomes and circulating tumor cells.

Beyond macromolecules, G4-based aptasensors have shown high sensitivity in detecting small molecules like 8-hydroxy-2′-deoxyguanosine, antibiotics, bisphenol A, mycotoxins, and metal ions, including toxic heavy metals such as arsenic, mercury, and lead [68].

G-quadruplexes (G4s) can be stabilized by various metal ions, including $K^+$, $Na^+$, $NH_4^+$ and $Pb^{2+}$ [69]. The binding affinity of these cations to G4s generally depends on several factors, such as ionic radius, hydration effects, and coordination behavior. Meanwhile, G4s can also effectively bind to hemin (iron (III)-protoporphyrin IX) and exhibit catalytic properties in peroxidation reactions similar to horseradish peroxidase (HRP), forming what are known as G4 DNAzymes (and G4 RNAzymes) [70].

Compared to natural protein peroxidases, G4 DNAzymes and RNAzymes offer several advantages, including small size, ease of synthesis, straightforward manipulation, and suitability for rational allosteric design. These features make them a powerful catalytic toolkit for applications in biosensing, biomaterials, and biomolecular devices. G4 DNAzymes have been extensively utilized as signal generators in the development of various biosensors and molecular machines, as well as promising biocatalysts in both aqueous and non-aqueous environments [71].

## 1.5 Optical detection methods

Biosensors can be categorized not only by the nature of their biorecognition elements but also by the type of transducer systems they use. These include electrochemical, optical, thermal, electronic, gravimetric, magnetic, and acoustic transducers [11]. Optical biosensors, in particular, generate a signal by detecting changes in electromagnetic radiation caused by a specific biochemical interaction. Common types of optical biosensors include colorimetric, fluorescence-based, bio-chemiluminescent, surface plasmon resonance (SPR), and optical fiber-based devices [72]. Technological advancements in miniaturization and instrumentation, combined with the non-invasive nature of these methods, make them well-suited for real-time applications.

### 1.5.1 Chemiluminescence

Chemiluminescence (CL) is the emission of light as a result of a chemical reaction, generally the oxidation of a luminophore or substrate [73]. This reaction generates an intermediate compound in an electronically excited state, which emits a photon ($h\nu$) as it returns to its ground state via radiative decay. Unlike photoluminescence, which requires an external excitation source, the excitation in CL arises from the chemical reaction itself, specifically through solution mixing and the reaction kinetics. Because no external light source is needed, CL offers the advantages of low background noise and high sensitivity.

The quantum yield ($\Phi_{CL}$) of a chemical luminescent reaction is defined by the following equation:

$$\Phi_{CL}=\Phi_R \cdot \Phi_{ES} \cdot \Phi_F$$

where $\Phi_R$ is the chemical yield of the reaction, $\Phi_{ES}$ is the fraction of the product entering the excited state, and $\Phi_F$ is the fluorescent quantum yield. This equation expresses the overall efficiency of a chemiluminescent reaction, which depends on several factors: the effectiveness of the chemical reaction itself, the efficiency of converting chemical energy into electronic excitation (i.e., energy transfer), and the fraction of excited molecules that emit photons. As a result, chemiluminescent quantum yields are generally lower than those observed in photoluminescence. Furthermore, light emission from a chemical reaction can occur only under specific conditions [74]:

- The reaction must be sufficiently exothermic to populate an electronically excited singlet state. This condition can be expressed through the free energy requirement:

  $$\Delta G \geq \frac{hc}{\lambda ex} = \frac{28600}{\lambda ex}$$

  Based on the above, the energy required by a chemiluminescence reaction producing photons in the visible (400 – 700 nm) range is around 40 – 70 kcal $mol^{-1}$ [75].

- The excited state must be accessible along the reaction coordinate.

- The electronically excited state must offer a favorable pathway for energy release. This can happen either when the reaction product itself is fluorescent or when energy transfer (intra-or intermolecular) populates an excited state.

The intensity of light emitted in a chemiluminescent reaction is proportional to the concentration of the analyte, making this technique highly attractive for analytical applications and enabling accurate quantitative analysis. By the 20th century, chemiluminescence had become a subject of intensive study. Researchers developed synthetic luminophores, such as luminol, which became widely used in both scientific research and forensic science. In the 1970s and 1980s, the sensitivity and simplicity of chemiluminescent reactions led to their integration into clinical diagnostics, immunoassays, and environmental monitoring. The oxidation of luminol, a diprotic acid with pKa values of 6 and 13, respectively, occurs under alkaline conditions and in the presence of $H_2O_2$ and genereates the corresponding radical anion in its excited state, which releases a photon while decaying to the ground state, as shown in the Figure 1.4 [76].

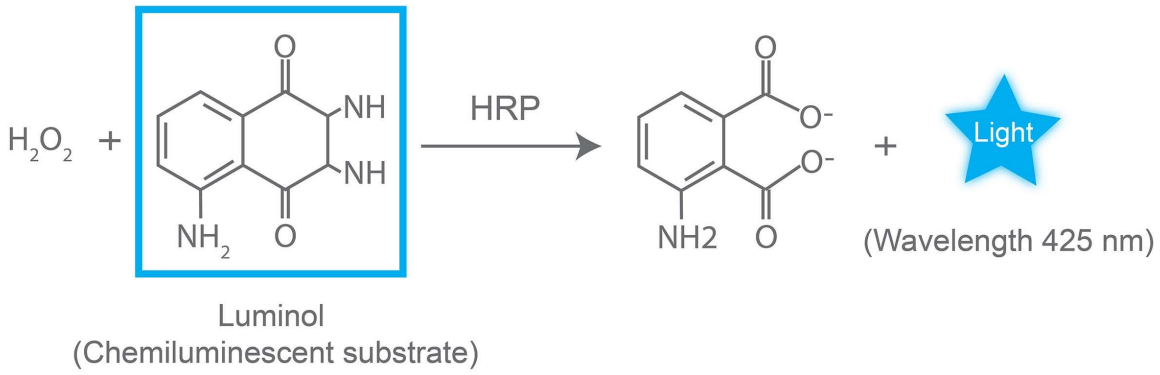


***Figure 1.4.*** *Chemiluminescent HRP-catalyzed oxidation of luminol.*

A blue light is emitted at 425nm with a relatively low quantum yield of 1%. The reaction is typically catalyzed by the metalloenzyme horseradish peroxidase (HRP), which is widely used as a label in immunometric assays due to its high catalytic efficiency and ability to amplify detection signals through rapid substrate turnover [77]. HRP catalyzes the oxidation of various organic chromogenic or luminescent substrates and by $H_2O_2$. Furthermore, reaching the steady-state phase of chemiluminescent (CL) emission allows for the establishment of consistent experimental conditions and enables accurate quantitative analysis of the labeled probe [78].

This is due to the direct correlation between steady-state light intensity and enzyme activity. The analytical performance of the HRP-catalyzed oxidation of luminol can be significantly enhanced by adding specific enhancers to the CL reaction mixture. These include compounds such as *p*-iodophenol, 4-(1-imidazolyl)phenol, other *p*-phenol derivatives, sodium 3-(10-phenothiazinyl)propane-1-sulfonate (SPTZ), *p*-phenylphenol and sodium tetraphenylborate (used as synergistic enhancers), as well as potassium ferricyanide, which acts as an electron mediator [79]. These additives amplify and stabilize the CL signal, thereby improving the sensitivity and reliability of the analytical method. Chemiluminescence detection techniques hold significant analytical value due to their ability to produce light without the need for photoexcitation, in contrast to fluorescence-based methods. This intrinsic property minimizes issues related to light scattering, background fluorescence, and fluctuations in light source intensity. As a result, the instrumentation required for chemiluminescence measurements is relatively simple, as it does not require an excitation source or wavelength selection components.

Moreover, when chemiluminescence detection is integrated with imaging systems, such as charge-coupled device (CCD) or complementary metal-oxide semiconductor (CMOS) cameras, or arrays of thin-film photosensors, it becomes possible to design highly adaptable setups for sample reading.

This flexibility is particularly advantageous for microarray formats, where spot arrangement on modified surfaces can be optimized, provided that cross-talk between spots is adequately controlled. Another major advantage of chemiluminescence is its broad dynamic range, which facilitates the analysis of samples with widely varying analyte concentrations [80]. However, one of the main limitations of this technique lies in the potential interference from the sample matrix, which may unpredictably enhance or inhibit the chemiluminescent reaction. Such effects can compromise signal reliability and lead to wrong results. Additionally, due to the high sensitivity of chemiluminescent labels, careful control of non-specific binding is crucial to minimize background noise. Therefore, surface functionalization strategies are critical to ensuring assay performance and accuracy. Finally, when chemiluminescence detection is used in flow-based systems, the temporal behavior of the emitted signal must be considered. Depending on the chemistry involved, photon emission can range from rapid "flash-type" signals to slower, sustained "glow-type" responses. This temporal instability, combined with the diffusion of light-emitting species in solution, can lead to reduced spatial resolution and must be accounted for during experimental design.

### 1.5.2 Electrochemiluminescence

Electrochemiluminescence (ECL) is a powerful luminescence technique that combines the high sensitivity of chemiluminescence with the precise control offered by electrochemical reactions [75]. As an excited-state electrochemical process, ECL involves redox reactions that generate an electronically excited state in a luminophore, resulting in the emission of photons. ECL exhibits two distinctive characteristics: first, the experimental noise is primarily dictated by the detector, since no external excitation light is required, unlike in fluorescence; second, the emission layer is determined by the very short lifetimes of the radical intermediates generated during the redox processes [81]. These features contribute to a significantly improved signal-to-noise ratio compared to photoluminescence, due to the reduction of light scattering and background luminescence. A pivotal breakthrough in the development of analytical ECL was achieved by Bard and co-workers, who first demonstrated ECL generation using a coreactant [82]. This discovery marked a turning point, transforming ECL from a scientific curiosity into a robust analytical platform with widespread applications and notable commercial success.

In practical and commercial ECL systems, the most commonly employed components are tripropylamine (TPrA), used as a sacrificial oxidative-reductive coreactant, and tris(2,2'-bipyridine)ruthenium(II) ($[Ru(bpy)_3]^{2+}$), which serves as the luminescent species.

First developed by Bard and co-workers, this system remains the benchmark for ECL studies due to its stability, reproducibility, and well-understood reaction mechanism [83]. Another widely used co-reactant in ECL is hydrogen peroxide ($H_2O_2$), which plays a dominant role in numerous luminol-based ECL systems. Luminol is one of the most extensively employed luminophores in ECL due to its intrinsic high sensitivity, broad linear dynamic range, and ability to undergo electrochemical oxidation to produce light. Upon application of an appropriate potential, luminol is oxidized, generating reactive intermediates that lead to photon emission. Because of its remarkable sensitivity toward $H_2O_2$, luminol-$H_2O_2$-based ECL systems are primarily used for the quantitative detection of hydrogen peroxide. This has made them particularly useful in applications involving enzymatic reactions where $H_2O_2$ is a by-product [84].

The efficiency of ECL ($\Phi_{ECL}$) is a product of two key factors: the yield of excited states ($\Phi_{ex}$), influenced by reaction kinetics, thermodynamics, and experimental conditions, and the probability of photon emission ($\Phi_{PL}$), an intrinsic property affected by the solvent and quenching interactions.

$$\Phi_{ECL} = \Phi_{PL} \cdot \Phi_{ex}$$

For excited states to form, the energy supplied by reactants must exceed the excited state's energy, a principle explained by Marcus theory, which asserts that ultrafast electron transfer outpaces vibrational energy dissipation, favoring excited product formation. Understanding and optimizing these factors are crucial for enhancing ECL's performance in diverse analytical applications.

## 1.6 Portable optical detectors

Traditional benchtop instrumentation, although precise and versatile, is generally unsuitable for biosensor applications, which demand portability, low power consumption, and compact design. To meet these requirements, biosensor systems rely on miniaturized electronics and integrated platforms capable of signal amplification, filtering, and data processing in real time. This shift has led to the development of specialized instrumentation, often based on microcontroller units (MCUs), application-specific integrated circuits (ASICs), or lab-on-a-chip technologies. In optical biosensors, detection is frequently performed using CCD (charge-coupled device) sensors or even CMOS cameras embedded in smartphones, enabling low-cost, portable, and user-friendly solutions. These compact systems allow biosensors to be deployed in point-of-care diagnostics, environmental monitoring, and wearable devices, where conventional lab equipment would be impractical or inaccessible.

The two primary types of solid-state image sensors, Charge-Coupled Devices (CCDs) and Complementary Metal-Oxide-Semiconductor (CMOS) sensors, differ fundamentally in their architecture and signal readout. CCDs are based on p-doped metal-oxide-semiconductor (MOS) capacitors, while CMOS sensors utilize p- and n-doped MOS field-effect transistors (MOSFETs). These image sensors, at their core, are arrays of point photodetectors called pixels, the smallest units capable of spatial resolution. Despite variations, their fundamental structure commonly includes top-mounted microlenses to focus light onto photodiodes, enhancing the fill factor. A mosaic color filter array, typically following a 1:2:1 Bayer pattern, enables color resolution by separating incoming light into RGB channels. The widely adopted pinned photodiode (PPD), invented in 1980, features a p-type layer that stabilizes surface potential, resulting in lower noise, higher quantum efficiency, and reduced dark current. Finally, integrated electronic components, including amplifiers and analog-to-digital converters (ADCs), transform collected photons into digitized voltage signals for storage and output.

CCDs were the first solid-state image sensors, invented in 1969. They operate by generating an electric charge when photons strike an array of connected capacitors, which is then sequentially transferred along the array to a common readout point for conversion into a voltage. This common readout and minimal in-pixel circuitry contribute to a high fill factor, leading to excellent photon collection efficiency, superior image quality, and low noise. Modern cooled back-side illuminated CCDs can achieve a quantum efficiency of up to 90%, read-out noise lower than 5 $e^-$, dark count rates of 0.001 $e^-/s$, and formats as large as 4096 x 4096 pixels with sizes down to 4 x 4 µm [85]. Furthermore, CCDs are often cooled devices to minimize thermal noise, especially in applications requiring high sensitivity. However, the sequential charge transfer process makes CCDs inherently slower in readout speed and more power-intensive. Despite these drawbacks, CCDs' superior image quality and strong low-light performance make them ideal for demanding applications like astronomy, professional photography, and medical imaging.

CMOS Image Sensors, developed in the mid-1990s using an active pixel sensor (APS) architecture where each pixel incorporates its own transistor, emerged to overcome CCDs' challenges with charge transfer, manufacturing difficulties, and performance at low temperatures or high frame rates [86]. CMOS transistors, by combining PMOS and NMOS elements, achieve reduced electrical resistance across a broader voltage range, resulting in lower power consumption, less heat generation, and consequently, reduced noise. Early CMOS sensors were front-side illuminated (FSI), but newer generations employ back-side illumination (BSI) by positioning photodiodes above interconnects to significantly boost photon collection efficiency. PureCel®Plus Technology significantly enhances

CMOS performance through innovations like buried color filter array (BCFA), deep trench isolation (DTI), and composite metal grid (CMG), leading to superior image quality by improving light capture, reducing crosstalk, and boosting sensitivity [75].

Unlike CCDs, CMOS image sensors feature individual readout circuits within each pixel, enabling faster, parallel data readout with lower power consumption and random access to pixel information. While this pixel-level circuitry historically meant a smaller photon capture area compared to CCDs, advancements like BSI have brought their signal-to-noise ratio to comparable levels. Their power efficiency, faster readout speeds, and greater data handling flexibility make CMOS image sensors ideal for battery-powered portable devices such as smartphones and cameras, and particularly well-suited as optical readers for Point-of-Care (POC) biosensors where portability and rapid real-time processing are critical [75]. Both CCD and CMOS sensors can be utilized in optics-free or "contact imaging" setups, where the sensor is placed directly in contact with the bioassay surface, allowing closer proximity to the sample for improved detection with minimized light crosstalk.

Beyond these established technologies, hydrogenated amorphous silicon (a-Si:H) photodiodes represent another crucial class of photosensors, particularly relevant for integrated optoelectronic and biosensing platforms. Unlike crystalline silicon-based CCDs and CMOS sensors, a-Si:H photodiodes are fabricated from non-crystalline silicon, enabling low-temperature deposition on a wide variety of substrates, including flexible and large-area ones. Typically realized in a p-i-n configuration, these devices rely on an intrinsic a-Si:H layer as the main photoactive region, ensuring efficient charge carrier generation and collection. This fabrication versatility facilitates their direct integration into Lab-on-Chip systems and thin-film electronic circuits, offering compact, cost-effective, and scalable solutions for optical detection. Their broad spectral response in the visible range (approximately 350–750 nm), high quantum efficiency, low dark current, and robustness under radiation exposure make them highly suitable for demanding environments and long-term operation. These characteristics position a-Si:H photodiodes as a versatile and complementary technology in the evolving landscape of advanced optical and biosensing devices [87].

## 1.7 Principles of microfluidics

Microfluidics studies the manipulation of fluids in micrometer-scale channels, allowing devices to precisely control small sample volumes for multiple applications in the biological sciences. This unique capability has established microfluidics as a key enabling technology in areas such as biomedical diagnostics and biosensor development, where efficient sample handling and

miniaturization are critical. These devices typically comprise inlets for introducing fluids, outlets for removing them, microchannels for guiding, mixing, and separating fluids, and chambers for holding samples or facilitating chemical or biological reactions. Fluid flow within microfluidic systems can be driven passively by capillary forces in the microchannels or actively using external forces, such as pressure applied through syringe pumps. To further control fluid movement, additional components like valves and flow resistors can be integrated into the system [88].

The first microfluidic systems were manufactured using silicon, glass, and polydimethylsiloxane (PDMS). More recently, thermoplastics and inexpensive paper have been adopted as alternative materials, with paper-based microfluidics gaining attention for its cost-effectiveness and sustainability. Paper is inherently porous and hydrophilic, offering a natural structural and fluidic substrate for the fabrication of microchannels [89], [90]. In paper-based devices, fluid transport is ruled by capillary action, and a variety of complex phenomena, such as wicking, absorption, and lateral flow, must be considered during design. The choice of paper substrate, ranging from filter and chromatography papers to nitrocellulose or specialized office and glossy papers, affects key parameters such as pore size, thickness, flow rate, and reagent retention, which in turn influence reaction efficiency, signal generation, and assay reproducibility. Devices such as paper-based analytical devices (μPADs) and lateral flow assays (LFAs) have been widely employed in diagnostics, with the pregnancy rapid diagnostic test (RDT) strip serving as the most well-known example [91]. Advanced designs, including origami-inspired folded devices, enable multiplexed or sequential analyses without external pumps by exploiting the capillarity and folding geometry of the paper substrate. Beyond paper, PDMS- and thermoplastic-based microfluidic devices have enabled more sophisticated lab-on-a-chip platforms, supporting applications such as pathogen detection, protein quantification, DNA analysis, and even cell culture to replicate microenvironmentsts. The flexibility in material choice and device design continues to expand the capabilities and accessibility of microfluidics for a wide range of biomedical and biosensing applications [92].

## 1.8 Fabrication Techniques

### 1.8.1 Wax printing

Wax printing is a widely used technique for fabricating paper-based microfluidic devices, offering a cost-effective and straightforward approach. This method involves printing wax patterns onto paper substrates using a solid ink printer, followed by heating to melt the wax, creating hydrophobic barriers that define fluidic channels. The resulting microfluidic paper-based analytical devices (μPADs) are

suitable for various applications, including diagnostics, environmental monitoring, and educational purposes. The wax printing process begins with designing the desired pattern using vector graphic software, such as Adobe Illustrator. The design is then printed onto filter paper using a solid ink printer, such as the Xerox Phaser 8560. After printing, the paper is heated to allow the wax to melt and penetrate the paper fibers, forming stable hydrophobic barriers. This technique is advantageous due to its simplicity, low cost, and the ability to produce devices without the need for cleanroom facilities or specialized equipment [93].

Wax-printed μPADs are widely used for colorimetric assays, pathogen detection, and environmental monitoring. The technique's simplicity and versatility enable rapid prototyping and customization, while recent improvements in resolution allow more complex fluidic designs and enhanced device performance. Its low cost and accessibility make wax printing an ideal method for developing portable analytical devices in research and education.

### 1.8.2 3D printing

Three-dimensional (3D) printing, first introduced in 1986 with Chuck Hull's patent for stereolithography (SLA), has evolved into a transformative technology in biosensor development, enabling the fabrication of complex, customizable, and cost-effective devices [94]. As an additive manufacturing technique, 3D printing builds objects layer by layer based on digital files from magnetic resonance imaging (MRI), computed tomography (CT) scans, or computer-aided design (CAD) models. A standard tessellation language (STL) file is generated from these data, allowing the object to be sliced into thin horizontal cross-sections for printing. Layer deposition can be calibrated according to geometry, design, and material by adjusting parameters such as layer thickness, temperature, printing supports, and print speed. After printing, supports are removed, and devices are washed and cured, with additional post-processing applied when specific material properties are required.

SLA utilizes liquid photopolymer resins cured by ultraviolet (UV) light, and has been applied in biomanufacturing and biosensing, including the patterning of microbes in 3D hydrogels and the fabrication of optical colorimetric biosensors for pathogen detection. Other common techniques include Fused Deposition Modeling (FDM), which extrudes thermoplastic materials like polylactic acid (PLA) layer by layer, and Selective Laser Sintering (SLS), which fuses powder-based materials with a laser. These approaches allow the integration of microfluidic channels, electrodes, and sensing

elements into a single platform, supporting portable, multifunctional, and wearable biosensors for real-time biomarker detection, environmental monitoring, and health diagnostics.

Recent advances include the use of graphene, conductive polymers, and nanocomposites to enhance sensitivity and selectivity, while biocompatible materials have expanded applications in wearable devices. Overall, 3D printing offers rapid prototyping, high precision, material and cost savings, design flexibility, and the ability to produce complex or flexible structures. Research continues to focus on developing eco-friendly materials to address sustainability challenges, while challenges such as stabilizing biorecognition elements and standardizing medical-grade materials remain [95], [96].

## 1.9 References


[1] P. Mehrotra, "Biosensors and their applications - A review," *J Oral Biol Craniofac Res*, vol. 6, no. 2, pp. 153–159, May 2016, doi: 10.1016/j.jobcr.2015.12.002.

[2] T. M. Swager and K. A. Mirica, "Introduction: Chemical Sensors," *Chem Rev*, vol. 119, no. 1, pp. 1–2, Jan. 2019, doi: 10.1021/ACS.CHEMREV.8B00764.

[3] F. G. Bănică, "Chemical Sensors and Biosensors: Fundamentals and Applications," *Chemical Sensors and Biosensors: Fundamentals and Applications*, Aug. 2012, doi: 10.1002/9781118354162.

[4] A. A. . Ensafi, "Electrochemical biosensors," p. 390, 2019.

[5] R. M. White, "A sensor classification scheme," *IEEE Trans Ultrason Ferroelectr Freq Control*, vol. 34, no. 2, pp. 124–126, 1987, doi: 10.1109/T-UFFC.1987.26922.

[6] P. J. Dobson, "Nanosensors: Physical, Chemical, and Biological, by Vinod Kumar Khanna," *Contemp Phys*, vol. 53, no. 4, pp. 391–392, Jul. 2012, doi: 10.1080/00107514.2012.689351.

[7] K. Cammann, "Bio-sensors based on ion-selective electrodes," *Fresenius' Zeitschrift für Analytische Chemie*, vol. 287, no. 1, pp. 1–9, Jan. 1977, doi: 10.1007/BF00539519/METRICS.

[8] D. R. Thvenot, K. Toth, R. A. Durst, and G. S. Wilson, "Electrochemical biosensors: Recommended definitions and classification (Technical Report)," *Pure and Applied Chemistry*, vol. 71, no. 12, pp. 2333–2348, Jan. 1999, doi: 10.1351/PAC199971122333/MACHINEREADABLECITATION/RIS.

[9] "The IUPAC Compendium of Chemical Terminology," *The IUPAC Compendium of Chemical Terminology*, 2025, doi: 10.1351/GOLDBOOK.

[10] L. C. Clark and C. Lyons, "ELECTRODE SYSTEMS FOR CONTINUOUS MONITORING IN CARDIOVASCULAR SURGERY," *Ann N Y Acad Sci*, vol. 102, no. 1, pp. 29–45, Oct. 1962, doi: 10.1111/J.1749-6632.1962.TB13623.X.

[11] V. Naresh and N. Lee, "A Review on Biosensors and Recent Development of Nanostructured Materials-Enabled Biosensors," *Sensors 2021, Vol. 21, Page 1109*, vol. 21, no. 4, p. 1109, Feb. 2021, doi: 10.3390/S21041109.

[12] B. Bucur, C. Purcarea, S. Andreescu, and A. Vasilescu, "Addressing the Selectivity of Enzyme Biosensors: Solutions and Perspectives," *Sensors 2021, Vol. 21, Page 3038*, vol. 21, no. 9, p. 3038, Apr. 2021, doi: 10.3390/S21093038.

[13] A. P. F. Turner, "Biosensors: sense and sensibility," *Chem Soc Rev*, vol. 42, no. 8, pp. 3184–3196, Mar. 2013, doi: 10.1039/C3CS35528D.

[14] "ICH M10 on bioanalytical method validation - Scientific guideline | European Medicines Agency (EMA)." Accessed: Oct. 02, 2025. [Online]. Available: https://www.ema.europa.eu/en/ich-m10-bioanalytical-method-validation-scientific-guideline

[15] D. Bhatia, S. Paul, T. Acharjee, and S. S. Ramachairy, "Biosensors and their widespread impact on human health," *Sensors International*, vol. 5, p. 100257, Jan. 2024, doi: 10.1016/J.SINTL.2023.100257.

[16] X. Ding, B. Srinivasan, and S. Tung, "Development and Applications of Portable Biosensors," *SLAS Technol*, vol. 20, no. 4, pp. 365–389, Aug. 2015, doi: 10.1177/2211068215581349.

[17] N. Bhalla, P. Jolly, N. Formisano, and P. Estrela, "Introduction to biosensors," *Essays Biochem*, vol. 60, no. 1, p. 1, Jun. 2016, doi: 10.1042/EBC20150001.

[18] M. Mascini and S. Tombelli, "Biosensors for biomarkers in medical diagnostics," *Biomarkers*, vol. 13, no. 7–8, pp. 637–657, 2008, doi: 10.1080/13547500802645905.

[19] C. W. Huang, C. Lin, M. K. Nguyen, A. Hussain, X. T. Bui, and H. H. Ngo, "A review of biosensor for environmental monitoring: principle, application, and corresponding achievement of sustainable development goals," *Bioengineered*, vol. 14, no. 1, p. 58, 2023, doi: 10.1080/21655979.2022.2095089.

[20] E. Xing, H. Chen, X. Xin, H. Cui, Y. Dou, and S. Song, “Recent Advances in Smart Phone-Based Biosensors for Various Applications,” *Chemosensors 2025, Vol. 13, Page 221*, vol. 13, no. 7, p. 221, Jun. 2025, doi: 10.3390/CHEMOSENSORS13070221.

[21] V. Oncescu, M. Mancuso, and D. Erickson, “Cholesterol testing on a smartphone,” *Lab Chip*, vol. 14, no. 4, pp. 759–763, Jan. 2014, doi: 10.1039/C3LC51194D.

[22] A. Roda, E. Michelini, M. Zangheri, M. Di Fusco, D. Calabria, and P. Simoni, “Smartphone-based biosensors: A critical review and perspectives,” *TrAC Trends in Analytical Chemistry*, vol. 79, pp. 317–325, May 2016, doi: 10.1016/J.TRAC.2015.10.019.

[23] A. C. Sun and D. A. Hall, “Point-of-Care Smartphone-based Electrochemical Biosensing,” *Electroanalysis*, vol. 31, no. 1, pp. 2–16, Jan. 2019, doi: 10.1002/ELAN.201800474.

[24] M. Thompson, K. Sonowal, P. Protim Borthakur, and K. Pathak, “Advances in Enzyme-Based Biosensors: Emerging Trends and Applications,” *Engineering Proceedings 2025, Vol. 106, Page 5*, vol. 106, no. 1, p. 5, Aug. 2025, doi: 10.3390/ENGPROC2025106005.

[25] S. Hornig, M. Michael, A. Grinyer, and J. Turner, “Introduction to enzymes and their applications,” *Introduction to Pharmaceutical Biotechnology, Volume 2*, pp. 1-1-1–29, Sep. 2018, doi: 10.1088/978-0-7503-1302-5CH1.

[26] I. Victorino da Silva Amatto *et al.*, “Enzyme engineering and its industrial applications,” *Biotechnol Appl Biochem*, vol. 69, no. 2, pp. 389–409, Apr. 2022, doi: 10.1002/BAB.2117.

[27] J. Atalah, P. Cáceres-Moreno, G. Espina, and J. M. Blamey, “Thermophiles and the applications of their enzymes as new biocatalysts,” *Bioresour Technol*, vol. 280, pp. 478–488, May 2019, doi: 10.1016/J.BIORTECH.2019.02.008.

[28] N. E. Ibrahim and K. Ma, “Industrial Applications of Thermostable Enzymes from Extremophilic Microorganisms,” *Current Biochemical Engineering (Discontinued)*, vol. 4, no. 2, pp. 75–98, Apr. 2017, doi: 10.2174/2212711904666170405123414.

[29] C. Silva, M. Martins, S. Jing, J. Fu, and A. Cavaco-Paulo, “Practical insights on enzyme stabilization,” *Crit Rev Biotechnol*, vol. 38, no. 3, pp. 335–350, Apr. 2018, doi: 10.1080/07388551.2017.1355294.

[30] “Coenzyme - an overview | ScienceDirect Topics.” Accessed: Oct. 03, 2025. [Online]. Available: https://www.sciencedirect.com/topics/medicine-and-dentistry/coenzyme

[31] “I principi di biochimica di Lehninger - David L Nelson, Michael M Cox | Zanichelli.” Accessed: Oct. 03, 2025. [Online]. Available: https://www.zanichelli.it/ricerca/prodotti/principi-di-biochimica-di-lehninger

[32] “Enzyme Inhibition - Types of Inhibition - TeachMePhysiology.” Accessed: Oct. 03, 2025. [Online]. Available: https://teachmephysiology.com/biochemistry/molecules-and-signalling/enzyme-inhibition/

[33] J. Eilertsen and S. Schnell, “A Kinetic Analysis of Coupled (or Auxiliary) Enzyme Reactions,” *Bull Math Biol*, vol. 80, no. 12, pp. 3154–3183, Dec. 2018, doi: 10.1007/S11538-018-0513-4/FIGURES/13.

[34] J. A. Bauer, M. Zámocká, J. Majtán, and V. Bauerová-Hlinková, “Glucose Oxidase, an Enzyme ‘Ferrari’: Its Structure, Function, Production and Properties in the Light of Various Industrial and Biotechnological Applications,” *Biomolecules*, vol. 12, no. 3, p. 472, Mar. 2022, doi: 10.3390/BIOM12030472.

[35] D. A. Kostić, D. S. Dimitrijević, G. S. Stojanović, I. R. Palić, A. S. Dordević, and J. D. Ickovski, “Xanthine Oxidase: Isolation, Assays of Activity, and Inhibition,” *J Chem*, vol. 2015, no. 1, p. 294858, Jan. 2015, doi: 10.1155/2015/294858.

[36] J. D. Newman and S. J. Setford, “Enzymatic biosensors,” *Mol Biotechnol*, vol. 32, no. 3, pp. 249–268, 2006, doi: 10.1385/MB:32:3:249.

[37] “FreeStyle Libre 3 System | FreeStyle Libre US.” Accessed: Oct. 03, 2025. [Online]. Available: https://www.freestyle.abbott/us-en/products/freestyle-libre-3.html?utm_source=chatgpt.com

[38] S. Li *et al.*, “Recent advances in glucose oxidase-based nanocarriers for tumor targeting therapy,” *Heliyon*, vol. 9, no. 10, p. e20407, Oct. 2023, doi: 10.1016/J.HELIYON.2023.E20407.

[39] C. Garcia-Hernandez, C. Garcia-Cabezon, F. Martin-Pedrosa, and M. L. Rodriguez-Mendez, “Analysis of musts and wines by means of a bio-electronic tongue based on tyrosinase and glucose oxidase using polypyrrole/gold nanoparticles as the electron mediator,” *Food Chem*, vol. 289, pp. 751–756, Aug. 2019, doi: 10.1016/j.foodchem.2019.03.107.

[40] M. Asal, Ö. Özen, M. Şahinler, H. T. Baysal, and İ. Polatoğlu, “An overview of biomolecules, immobilization methods and support materials of biosensors,” *Sensor Review*, vol. 39, no. 3, pp. 377–386, May 2019, doi: 10.1108/SR-04-2018-0084.

[41] S. Liébana and G. A. Drago, “Bioconjugation and stabilisation of biomolecules in biosensors,” *Essays Biochem*, vol. 60, no. 1, pp. 59–68, Jun. 2016, doi: 10.1042/EBC20150007.

[42] A. Herrmann, R. Haag, and U. Schedler, “Hydrogels and Their Role in Biosensing Applications,” *Adv Healthc Mater*, vol. 10, no. 11, p. 2100062, Jun. 2021, doi: 10.1002/ADHM.202100062.

[43] M. Sharafeldin and J. J. Davis, “Characterising the biosensing interface,” *Anal Chim Acta*, vol. 1216, p. 339759, Jul. 2022, doi: 10.1016/J.ACA.2022.339759.

[44] S. Ferretti, S. Paynter, D. A. Russell, K. E. Sapsford, and D. J. Richardson, “Self-assembled monolayers: a versatile tool for the formulation of bio-surfaces,” *TrAC Trends in Analytical Chemistry*, vol. 19, no. 9, pp. 530–540, Sep. 2000, doi: 10.1016/S0165-9936(00)00032-7.

[45] V. Karunnanithy *et al.*, “Effectiveness of Lyoprotectants in Protein Stabilization During Lyophilization,” *Pharmaceutics*, vol. 16, no. 10, p. 1346, Oct. 2024, doi: 10.3390/PHARMACEUTICS16101346/S1.

[46] N. Seddaoui, N. Colozza, L. Gullo, and F. Arduini, “Paper as smart support for bioreceptor immobilization in electrochemical paper-based devices,” *Int J Biol Macromol*, vol. 253, p. 127409, Dec. 2023, doi: 10.1016/J.IJBIOMAC.2023.127409.

[47] M. M. Calabretta *et al.*, “Paper-Based Immunosensors with Bio-Chemiluminescence Detection,” *Sensors 2021, Vol. 21, Page 4309*, vol. 21, no. 13, p. 4309, Jun. 2021, doi: 10.3390/S21134309.

[48] C. Parolo and A. Merkoçi, “Paper-based nanobiosensors for diagnostics,” *Chem Soc Rev*, vol. 42, no. 2, pp. 450–457, Dec. 2012, doi: 10.1039/C2CS35255A.

[49] S. Kumar, J. B. Kaushal, and H. P. Lee, “Sustainable Sensing with Paper Microfluidics: Applications in Health, Environment, and Food Safety,” *Biosensors 2024, Vol. 14, Page 300*, vol. 14, no. 6, p. 300, Jun. 2024, doi: 10.3390/BIOS14060300.

[50] Y. Zhang, A. K. Khan, D. See, and J. Y. Ying, “Enhancing Protein Adsorption for Improved Lateral Flow Assay on Cellulose Paper by Depleting Inert Additive Films Using Reactive Plasma,” *ACS Appl Mater Interfaces*, vol. 15, no. 5, pp. 6561–6571, Feb. 2023, doi: 10.1021/ACSAMI.2C21501.

[51] X. Luo, J. Xia, X. Jiang, M. Yang, and S. Liu, “Cellulose-Based Strips Designed Based on a Sensitive Enzyme Colorimetric Assay for the Low Concentration of Glucose Detection,” *Anal*

*Chem*, vol. 91, no. 24, pp. 15461–15468, Dec. 2019, doi: 10.1021/ACS.ANALCHEM.9B03180.

[52] N. Ruecha, R. Rangkupan, N. Rodthongkum, and O. Chailapakul, "Novel paper-based cholesterol biosensor using graphene/polyvinylpyrrolidone/polyaniline nanocomposite," *Biosens Bioelectron*, vol. 52, pp. 13–19, Feb. 2014, doi: 10.1016/j.bios.2013.08.018.

[53] P. Bhardwaj *et al.*, "Paper-based point of care diagnostics for cancer biomarkers," *Sensors & Diagnostics*, vol. 3, no. 4, pp. 504–535, Apr. 2024, doi: 10.1039/D3SD00340J.

[54] F. Arduini, S. Cinti, V. Caratelli, L. Amendola, G. Palleschi, and D. Moscone, "Origami multiple paper-based electrochemical biosensors for pesticide detection," *Biosens Bioelectron*, vol. 126, pp. 346–354, Feb. 2019, doi: 10.1016/j.bios.2018.10.014.

[55] I. M. El-Sewify, A. Radwan, and H. M. E. S. Azzazy, "Multi-responsive paper chemosensors based on mesoporous silica nanospheres for quantitative sensing of heavy metals in water," *RSC Adv*, vol. 13, no. 10, pp. 6433–6441, Feb. 2023, doi: 10.1039/D3RA00369H.

[56] C. Cie´slik *et al.*, "Advancements in Hydrogels: A Comprehensive Review of Natural and Synthetic Innovations for Biomedical Applications," *Polymers 2025, Vol. 17, Page 2026*, vol. 17, no. 15, p. 2026, Jul. 2025, doi: 10.3390/POLYM17152026.

[57] T. C. Ho *et al.*, "Hydrogels: Properties and Applications in Biomedicine," *Molecules*, vol. 27, no. 9, p. 2902, May 2022, doi: 10.3390/MOLECULES27092902.

[58] M. M. Rana and H. De la Hoz Siegler, "Evolution of Hybrid Hydrogels: Next-Generation Biomaterials for Drug Delivery and Tissue Engineering," *Gels*, vol. 10, no. 4, p. 216, Apr. 2024, doi: 10.3390/GELS10040216.

[59] D. Revathi, S. Panda, K. Deshmukh, N. Khotele, V. R. K. Murthy, and S. K. K. Pasha, "Smart hydrogels for sensing and biosensing – Preparation, smart behaviours, and emerging applications – A comprehensive review," *Polym Test*, vol. 150, p. 108912, Sep. 2025, doi: 10.1016/J.POLYMERTESTING.2025.108912.

[60] D. Calabria *et al.*, "Smartphone-Based Chemiluminescence Glucose Biosensor Employing a Peroxidase-Mimicking, Guanosine-Based Self-Assembled Hydrogel," *Biosensors 2023, Vol. 13, Page 650*, vol. 13, no. 6, p. 650, Jun. 2023, doi: 10.3390/BIOS13060650.

[61] A. Bhat, J. M. Amanor-Boadu, and A. Guiseppi-Elie, “Toward Impedimetric Measurement of Acidosis with a pH-Responsive Hydrogel Sensor,” *ACS Sens*, vol. 5, no. 2, pp. 500–509, Feb. 2020, doi: 10.1021/ACSSENSORS.9B02336.

[62] N. A. Peppas and D. S. Van Blarcom, “Hydrogel-based biosensors and sensing devices for drug delivery,” *Journal of Controlled Release*, vol. 240, pp. 142–150, Oct. 2016, doi: 10.1016/J.JCONREL.2015.11.022.

[63] W. Xu *et al.*, “Functional Nucleic Acid Nanomaterials: Development, Properties, and Applications,” *Angew Chem Int Ed Engl*, vol. 60, no. 13, p. 6890, Mar. 2020, doi: 10.1002/ANIE.201909927.

[64] Y. X. Wu and Y. J. Kwon, “Aptamers: The ‘evolution’ of SELEX,” *Methods*, vol. 106, pp. 21–28, Aug. 2016, doi: 10.1016/J.YMETH.2016.04.020.

[65] S. Y. Toh, M. Citartan, S. C. B. Gopinath, and T. H. Tang, “Aptamers as a replacement for antibodies in enzyme-linked immunosorbent assay,” *Biosens Bioelectron*, vol. 64, pp. 392–403, Feb. 2015, doi: 10.1016/J.BIOS.2014.09.026.

[66] C. Roxo, W. Kotkowiak, and A. Pasternak, “G-Quadruplex-Forming Aptamers—Characteristics, Applications, and Perspectives,” *Molecules 2019, Vol. 24, Page 3781*, vol. 24, no. 20, p. 3781, Oct. 2019, doi: 10.3390/MOLECULES24203781.

[67] M. I. Umar, D. Ji, C. Y. Chan, and C. K. Kwok, “G-Quadruplex-Based Fluorescent Turn-On Ligands and Aptamers: From Development to Applications,” *Molecules 2019, Vol. 24, Page 2416*, vol. 24, no. 13, p. 2416, Jun. 2019, doi: 10.3390/MOLECULES24132416.

[68] J. Dejeu, A. Van der Heyden, N. Spinelli, E. Defrancq, and L. Coche-Guérente, “Recent progress in the design of G-quadruplex–based electrochemical aptasensors,” *Curr Opin Electrochem*, vol. 30, p. 100812, Dec. 2021, doi: 10.1016/J.COELEC.2021.100812.

[69] X. Zhang *et al.*, “Impact of NH4+ on the catalytic activity of G-quadruplex/hemin DNAzyme for chemiluminescent sensing,” *Anal Bioanal Chem*, pp. 1–10, Apr. 2025, doi: 10.1007/S00216-025-05842-Y/TABLES/2.

[70] J. Chen *et al.*, “Highly active G-quadruplex/hemin DNAzyme for sensitive colorimetric determination of lead(II),” *Microchimica Acta*, vol. 186, no. 12, pp. 1–8, Dec. 2019, doi: 10.1007/S00604-019-3950-3/TABLES/3.

[71] S. Khan, B. Burciu, C. D. M. Filipe, Y. Li, K. Dellinger, and T. F. Didar, "DNAzyme-Based Biosensors: Immobilization Strategies, Applications, and Future Prospective," *ACS Nano*, vol. 15, no. 9, pp. 13943–13969, Sep. 2021, doi: 10.1021/ACSNANO.1C04327.

[72] A. K. Singh, S. Mittal, M. Das, A. Saharia, and M. Tiwari, "Optical biosensors: a decade in review," *Alexandria Engineering Journal*, vol. 67, pp. 673–691, Mar. 2023, doi: 10.1016/J.AEJ.2022.12.040.

[73] P. S. Francis and C. F. Hogan, "Luminescence," *Comprehensive Analytical Chemistry*, vol. 54, pp. 343–373, Jan. 2008, doi: 10.1016/S0166-526X(08)00613-2.

[74] A. . Roda, "Chemiluminescence and bioluminescence : past, present and future," p. 590, 2011, Accessed: Oct. 13, 2025. [Online]. Available: https://books.google.com/books/about/Chemiluminescence_and_Bioluminescence.html?hl=it&id=xnIoDwAAQBAJ

[75] R. Abbasi, X. Hu, A. Zhang, I. Dummer, and S. Wachsmann-Hogiu, "Optical Image Sensors for Smart Analytical Chemiluminescence Biosensors," *Bioengineering 2024, Vol. 11, Page 912*, vol. 11, no. 9, p. 912, Sep. 2024, doi: 10.3390/BIOENGINEERING11090912.

[76] C. A. Marquette and L. J. Blum, "Applications of the luminol chemiluminescent reaction in analytical chemistry," *Anal Bioanal Chem*, vol. 385, no. 3, pp. 546–554, Jun. 2006, doi: 10.1007/S00216-006-0439-9.

[77] M. Hamid and Khalil-ur-Rehman, "Potential applications of peroxidases," *Food Chem*, vol. 115, no. 4, pp. 1177–1186, Aug. 2009, doi: 10.1016/J.FOODCHEM.2009.02.035.

[78] A. Roda and M. Guardigli, "Analytical chemiluminescence and bioluminescence: latest achievements and new horizons," *Anal Bioanal Chem*, vol. 402, no. 1, pp. 69–76, Jan. 2012, doi: 10.1007/S00216-011-5455-8.

[79] G. Chen *et al.*, "A review of enhancers for chemiluminescence enzyme immunoassay," *Food Agric Immunol*, vol. 28, no. 2, pp. 315–327, Mar. 2017, doi: 10.1080/09540105.2016.1272550.

[80] W. R. G. Baeyens *et al.*, "Chemiluminescence-based detection: principles and analytical applications in flowing streams and in immunoassays," *J Pharm Biomed Anal*, vol. 17, no. 6–7, pp. 941–953, Sep. 1998, doi: 10.1016/S0731-7085(98)00062-4.

[81] V. Gupta, F. Falciani, B. R. Layman, M. L. Hill, S. Rapino, and J. E. Dick, "Real-Time Visualization of Endogenous H2O2 Production in Mammalian Spheroids by

Electrochemiluminescence," *Chemical & Biomedical Imaging*, vol. 3, no. 5, pp. 310–321, May 2025, doi: 10.1021/CBMI.4C00105.

[82] A. Zanut *et al.*, "Insights into the mechanism of coreactant electrochemiluminescence facilitating enhanced bioanalytical performance," *Nat Commun*, vol. 11, no. 1, p. 2668, Dec. 2020, doi: 10.1038/S41467-020-16476-2.

[83] G. Valenti, A. Zanut, A. Fiorani, M. Marcaccio, S. Rapino, and F. Paolucci, "Novel Mechanism Insight for Enhanced Electrochemiluminescence Signal," *ECS Meeting Abstracts*, vol. MA2021-01, no. 61, p. 1617, May 2021, doi: 10.1149/MA2021-01611617MTGABS.

[84] C. Mwanza and S. N. Ding, "Newly Developed Electrochemiluminescence Based on Bipolar Electrochemistry for Multiplex Biosensing Applications: A Consolidated Review," *Biosensors 2023, Vol. 13, Page 666*, vol. 13, no. 6, p. 666, Jun. 2023, doi: 10.3390/BIOS13060666.

[85] A. Roda *et al.*, "Progress in chemical luminescence-based biosensors: A critical review," *Biosens Bioelectron*, vol. 76, pp. 164–179, Feb. 2016, doi: 10.1016/j.bios.2015.06.017.

[86] E. R. Fossum, "CMOS active pixel image sensors," *Nucl Instrum Methods Phys Res A*, vol. 395, no. 3, pp. 291–297, Aug. 1997, doi: 10.1016/S0168-9002(97)00812-7.

[87] D. Caputo *et al.*, "Microfluidic chip with integrated a-Si:H photodiodes for chemiluminescence-based bioassays," *IEEE Sens J*, vol. 13, no. 7, pp. 2595–2602, 2013, doi: 10.1109/JSEN.2013.2256889.

[88] K. Yang, H. Peretz-Soroka, Y. Liu, and F. Lin, "Novel Developments of Mobile Sensing Based on the Integration of Microfluidic Devices and Smartphone," *Lab Chip*, vol. 16, no. 6, p. 943, Mar. 2016, doi: 10.1039/C5LC01524C.

[89] S. M. Scott and Z. Ali, "Fabrication Methods for Microfluidic Devices: An Overview," *Micromachines 2021, Vol. 12, Page 319*, vol. 12, no. 3, p. 319, Mar. 2021, doi: 10.3390/MI12030319.

[90] R. García-Azuma, K. Werner, C. Revilla-Monsalve, O. Trinidad, N. F. Altamirano-Bustamante, and M. M. Altamirano-Bustamante, "Unveiling the state of the art: a systematic review and meta-analysis of paper-based microfluidic devices," *Front Bioeng Biotechnol*, vol. 12, p. 1421831, Aug. 2024, doi: 10.3389/FBIOE.2024.1421831/BIBTEX.

[91] D. M. Kinyua, D. M. Memeu, C. N. Mugo Mwenda, B. Della Ventura, and R. Velotta, “Advancements and Applications of Lateral Flow Assays (LFAs): A Comprehensive Review,” *Sensors 2025, Vol. 25, Page 5414*, vol. 25, no. 17, p. 5414, Sep. 2025, doi: 10.3390/S25175414.

[92] A. G. Niculescu, C. Chircov, A. C. Bîrcă, and A. M. Grumezescu, “Fabrication and Applications of Microfluidic Devices: A Review,” *Int J Mol Sci*, vol. 22, no. 4, p. 2011, Feb. 2021, doi: 10.3390/IJMS22042011.

[93] E. B. Strong, S. A. Schultz, A. W. Martinez, and N. W. Martinez, “Fabrication of Miniaturized Paper-Based Microfluidic Devices (MicroPADs),” *Scientific Reports 2019 9:1*, vol. 9, no. 1, pp. 1–9, Jan. 2019, doi: 10.1038/s41598-018-37029-0.

[94] M. Whitaker, “The history of 3D printing in healthcare,” *https://doi.org/10.1308/147363514X13990346756481*, vol. 96, no. 7, pp. 228–229, Jun. 2015, doi: 10.1308/147363514X13990346756481.

[95] G. Remaggi, A. Zaccarelli, and L. Elviri, “3D Printing Technologies in Biosensors Production: Recent Developments,” *Chemosensors*, vol. 10, no. 2, p. 65, Feb. 2022, doi: 10.3390/CHEMOSENSORS10020065/S1.

[96] A. S. Kulkarni, S. Khandelwal, Y. Thakre, J. Rangole, M. B. Kulkarni, and M. Bhaiyya, “A Review on 3D-Printed Miniaturized Devices for Point-of-Care-Testing Applications,” *Biosensors (Basel)*, vol. 15, no. 6, p. 340, Jun. 2025, doi: 10.3390/BIOS15060340.

# *Chapter 2*

*Thesis proposal*

This Ph.D. research explores the development of advanced biosensor technologies tailored for diverse applications, including clinical diagnostics, food safety, and space exploration. The thesis investigates how biosensors can be integrated with innovative fabrication techniques, such as wax printing and 3D printing, to produce Point-of-Care (POC) devices that are both high-performing and sustainable. By enabling rapid and decentralized analysis, they facilitate early diagnosis and allow autonomous monitoring. Chapter 3 focuses on the development of 3D-printed electrochemical devices for point-of-care testing. A miniaturized ECL biosensor was created for glucose detection using a luminol/$H_2O_2$ system with carbon black-doped PLA electrodes, powered by a 1.5V battery and read via smartphone. Incorporation of glucose oxidase in an agarose hydrogel allowed the production of preloaded devices requiring only sample addition. The biosensor successfully detected glucose and demonstrated potential for real sample analysis, highlighting the versatility of 3D-printed electrochemical platforms. In Chapter 4, accurate microbial monitoring in water was addressed by developing a DNA-based aptamer biosensor for ATP detection, a key marker of cell viability. In this system, ATP binding activates a catalytic DNAzyme domain, producing a chemiluminescent signal. Integration with origami microfluidic paper-based devices (μPADs) preloaded with reagents enabled on-paper, portable detection, suitable for point-of-care applications. Chapter 5 focused on type III CRISPR-Cas systems, recognized as one of the most promising platforms for CRISPR RNA-guided diagnostics (CRISPR-dx). Guided by crRNA, type III CRISPR-Cas complexes generate cOA signalling molecules that activate Csx1 RNase, enabling sensitive nucleic acid detection. In this work, a chemiluminescent (CL) assay was developed, in which a G-quadruplex (G4) RNA probe catalyses a luminol/$H_2O_2$ reaction in the presence of hemin. Upon activation by the target RNA, Csx1 degrades the G4 probe, reducing the chemiluminescent signal, enabling sensitive and portable nucleic acid detection without external light sources. Finally, Chapter 6 discusses the BOREALIS project (Biofilm Onboard Radiation Exposure Assessment Lab In Space), a CubeSat mission supported by the Italian Space Agency, that aims to study the effects of space conditions on microbial biofilms, evaluate protective strategies against radiation, and investigate secondary particle formation from cosmic radiation-satellite material interactions. In this context, protocols were optimized for producing bacterial biofilms in lab-on-chip devices, employing microfluidic circuits to deliver oxygen and nutrients along defined channels, ensuring proper biofilm growth and maintenance under controlled laboratory conditions.

# *Chapter 3*

## *Smartphone-based 3D-printed electrochemiluminescence enzyme biosensor for reagentless glucose quantification in real matrices*

---

*Reproduced from: "**Smartphone-based 3D-printed electrochemiluminescence enzyme biosensor for reagentless glucose quantification in real matrices**"*
*Donato Calabria, Elisa Lazzarini, Andrea Pace, Ilaria Trozzi, Martina Zangheri, Stefano Cinti, Marinella Difonzo, Giovanni Valenti, Massimo Guardigli, Francesco Paolucci, Mara Mirasoli*

***Biosensors and Bioelectronics**, 227, (2023), 115146*
*https://doi.org/10.1016/j.bios.2023.115146*

## 3.1 Introduction

Three-dimensional (3D) printing, which relies on the layer-by-layer addition of materials (additive manufacturing), is gaining increasing interest in the biosensors field, as it enables easy, rapid, reproducible, and low-cost prototyping and production of device components, even of complex geometries. The fast and almost direct design-to-object workflow provides great flexibility in the design and optimization of the analytical system [1], [2]. In addition, 3D printing is considered an environmental-friendly process as it generates minimal waste and enables in-house production, thus reducing the environmental impacts of transportation and storage.

3D printing has been used for manufacturing a variety of biosensor components, such as microfluidic chips [3], [4], [5], [6], analytical cartridges [7], [8], optical components [9], [10], smartphone interfaces [11], [12], [13], analytical device components [14], [15], [16], and wearable devices [17]. More recently, energy storage devices and electrodes for electroanalytical applications have been also produced [18], [19], [20], [21], employing commercially available or in-house fabricated conductive thermoplastic materials, obtained by incorporating into polymers conductive nanomaterials such as carbon nanotubes, carbon black, and graphene. This approach has helped to overcome some limitations due to the manual fabrication of electrochemical biosensors (e.g., poor reproducibility), as well as to improve the overall analytical performance [18], [20].

Electrochemiluminescence (ECL), a luminescent phenomenon induced by an electrochemical stimulus on a specific molecular system [22], [23], is one of the leading transduction techniques in biosensing [24], [25], [26]. As compared with photoluminescence and chemiluminescence, it provides superior temporal and spatial control of light emission, very low background, high sensitivity, broad dynamic range, and rapid measurement [27], [28], [29], [30], [31], [32]. In addition, ECL is less sensitive to electrical interferences and can exploit simplified electric circuit devices, since photon emission is measured instead of current [33]. Owing to these characteristics, ECL is particularly appealing for the development of portable biosensing devices [26], [34], [35], [36], [37]. In the last two decades, integration of biosensors into smartphone-based systems has been demonstrated a unique opportunity for widespread availability of portable devices [38], [39]. Delaney et al. first proposed a smartphone-based microfluidic biosensor exploiting the mobile phone camera for ECL measurement [40], paving the way for an ever-increasing number of publications in this field [34], [41], [42], [43].

Despite of its potential advantages, 3D printing has been poorly exploited in ECL [6], [44], [45], [46], [47] and only a few biosensing devices exploiting 3D-printed electrodes have been proposed so far [48], [49], [50]. Herein we combined 3D printing technology with ECL transduction for developing a smartphone-based biosensor for glucose detection in biological samples.

The biosensor relied on the glucose oxidation catalysed by glucose oxidase (GO), followed by the ECL detection of the produced hydrogen peroxide. Luminol was employed as the ECL reagent, taking advantage of its low oxidation potential and high emission yield [33], [51], [52], [53]. With respect to previously published work [48], [49], our biosensor displays improved features for point-of-care application, such as a simple electrical circuit and a ready-to-use format, in which all the reagents are prestored into the device.

## 3.2 Materials and methods

### 3.2.1 Reagents and materials

Glucose oxidase (GO, from *Aspergillus niger*, ≥ 250 U $mg^{-1}$ solid), luminol (5-amino-2,3-dihydro-1,4-phthalazindione sodium salt), hydrogen peroxide (30% (v/v) aqueous solution), β-D-glucose, and agarose were purchased from Merck KGaA (Darmstadt, Germany). All the other chemicals employed were of the highest purity available. Artificial serum was prepared following a published composition [54] to which 35 g $L^{-1}$ Human Serum Albumin was added.

The enzymatic colorimetric assay (Glucose Colorimetric Detection Kit) in the 96-well microplate format used as a reference method for assessing glucose concentration of real samples was bought from Life Technologies Corporation (Thermo Fisher Scientific, Frederick, MD).

The conductive Protopasta composite PLA (PLA loaded with about 20% of carbon black, resistivity 15 Ω cm) and the conventional PLA polymers were from Protoplant Inc. (Vancouver, WA) and MakerBot Industries (New York, NY), respectively.

### 3.2.2 Data analysis and processing

Quantitative analysis of ECL images was performed using the freeware ImageJ v.1.53s software (National Institutes of Health, Bethesda, MD). GraphPad Prism v.8.3.0 software (GraphPad Software, San Diego, CA) was employed for data graphing and regression analysis.

### 3.2.3 Electroanalytical device

The ECL device components (Figures 3.1a and 3.1b) were designed using SketchUp Pro 2021 CAD software (Trimble Inc., Sunnyvale, CA) and manufactured from PLA polymer, either conductive (for working and auxiliary electrodes) or non-conductive (for spacer), using a commercial Fused Deposition Modelling (FDM) 3D printer (MakerBot Replicator 2X, MakerBot Industries).

The components were then assembled using a cyanoacrylate-based glue and a plastic layer with transparent pressure-sensitive adhesive was applied to the bottom of the ECL device to create the measurement cell (about 100 µL of volume).

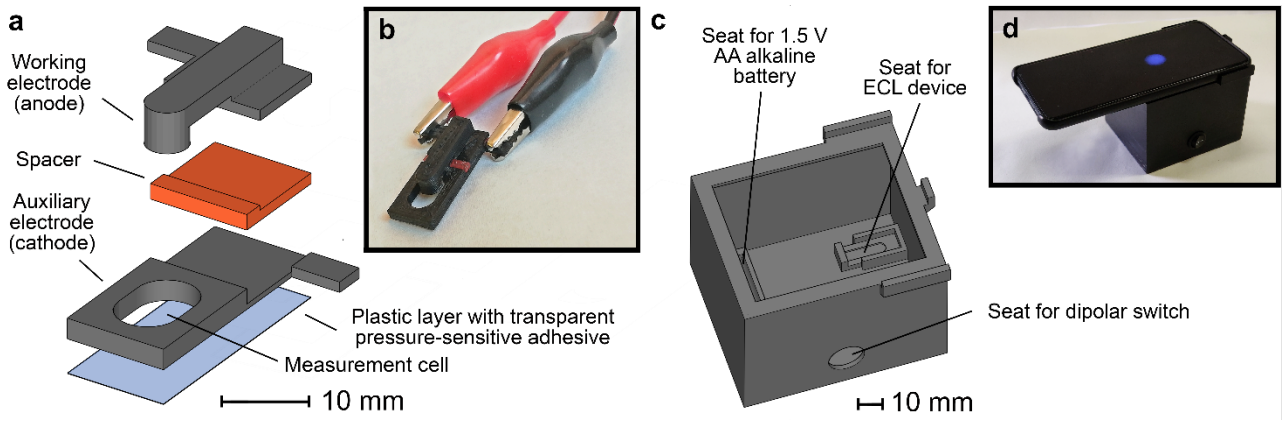


***Figure 3.1.*** *(a) Scheme and (b) photograph of the 3D-printed ECL device. Black and orange components were produced in conductive and non-conductive PLA polymer, respectively. (c) Scheme of the 3D-printed dark box used to perform ECL measurements with the hydrogel-based ECL device employing a smartphone for the detection of the ECL emission and (d) photograph of the analytical system during a measurement.*

### 3.2.4 Cyclic voltammetry measurements

Cyclic voltammetry (CV)/ECL and electrochemical measurements were conducted with a SP-300 potentiostat (Biologic, Seyssinet-Pariset, France) using the electroanalytical device described below together with an Ag/AgCl external reference electrode. The ECL signal was measured with a R928 photomultiplier tube (Hamamatsu Photonics K.K., Shizuoka, Japan) supply with 750 V and placed at a fixed height from the electrochemical cell, inside a dark box. A high-voltage power supply socket assembly with a transimpedance amplifier (C6271, Hamamatsu Photonics K.K.) was employed to the photomultiplier, using an external trigger connection to the potentiostat DAC module. Light/current/potential curves were recorded by collecting the amplified photomultiplier output signal with the ADC module of the potentiostat.

### 3.2.5 Analytical system for the solution based ECL device

The ECL emission was acquired with an ATIK 11000 Charge-Coupled Device (CCD) camera (ATIK Cameras, New Road, Norwich) equipped with a dark box to avoid interference from ambient light during the measurement. The camera employed a large format; high resolution Kodak KAI 11002

monochrome sensor cooled down to 5°C by a two-stage Peltier element to reduce thermal noise. The CCD sensor was coupled with a 25 × 25 $mm^2$ fibre optic faceplate in a contact imaging configuration as previously described [55]. For ECL measurements, the ECL device was positioned inside the dark box in correspondence with the fibre optic faceplate and a 1.5 V voltage was applied to the electrodes using a variable voltage DC power supply.

### 3.2.6 Assay procedures for the solution-based ECL device

For the quantification of hydrogen peroxide, 40 µL of $H_2O_2$ standard solution or water (for blank) were dispensed in the measurement cell of the ECL device. Then, 40 µL of a 10 mmol $L^{-1}$ luminol solution in 0.2 mol $L^{-1}$ carbonate buffer (pH 10.8) was added prior to application of the voltage. The ECL emission was measured over a period of 100 s acquiring a series of 20 consecutive images (exposure time 5 s). The voltage was applied to the ECL device 20 s after the starting of the acquisition, thus the first four images could be used for evaluation of the background signal. For the quantification of glucose, 40 µL of glucose standard solution, water (for blank) or sample (if necessary, appropriately diluted with water to obtain a glucose concentration within the assay calibration range) were dispensed in the measurement cell, followed by 10 µL of a 1.25 U $\mu L^{-1}$ GO solution in 0.1 mol $L^{-1}$ phosphate buffer (pH 7.0). After a 15 min-incubation period, 40 µL of a 10 mmol $L^{-1}$ luminol solution in 0.2 mol $L^{-1}$ carbonate buffer (pH 10.8) was added and the ECL emission was measured as described before.

For each experiment the acquired images were analysed to evaluate the signal, i.e., the sum of the pixel intensities over the region of interest (ROI) area corresponding to the anode of the ECL device. The background (e.g., due to thermal and readout noise of the CCD camera as well as to CL emission from the spontaneous oxidation of luminol) was calculated as the mean of the signals obtained for the first four images of the sequence, then the kinetic profile of the ECL emission was generated by plotting the background-subtracted ECL emission intensity vs. time. Finally, the ECL signal of each experiment was calculated by integrating the ECL emission kinetic profile over the 20 – 80 s time interval. The assay calibration curves were generated by graphing the blank-subtracted ECL signals obtained for $H_2O_2$ (or glucose) standard solutions vs. the logarithm of analyte concentration and fitting the experimental data by a first-order polynomial equation, and the concentrations of unknown $H_2O_2$ (or glucose) samples were calculated by interpolation of their blank-subtracted ECL signals on the calibration curve.

### 3.2.7 Hydrogel-based ECL biosensor

The hydrogel-based ECL biosensor for the measurement of $H_2O_2$ was produced by dispensing in the measurement cell 100 µL of a hot 0.1 mol $L^{-1}$ carbonate buffer solution (pH 10.8) containing 0.8% (m/v) agarose and 5 mmol $L^{-1}$ luminol. After cooling to room temperature, a luminol-functionalized agarose hydrogel was obtained. The ECL device for the measurement of glucose was obtained in a similar way, except that the solution dispensed into the device also contained 0.125 U $\mu L^{-1}$ of GO (the enzyme was added just before dispensation of the solution into the device to avoid thermal degradation).

### 3.2.8 Analytical system for the hydrogel-based ECL biosensor

Detection of the ECL emission was performed with a Samsung S20 smartphone (Samsung, Seoul, South Korea) using the proprietary camera app. A 3D-printed dark box produced in black PLA (Figures 3.1c and 3.1d) prevented interference from ambient light during the ECL measurement and ensured the correct positioning of the ECL device with respect to the smartphone camera (the device was positioned with the auxiliary electrode at the top, so that the ECL emission at the working electrode would be visible by the camera). A 1.5V AA alkaline battery and a bipolar switch allowed generation and control of the ECL emission.

### 3.2.9 Assay procedures for the hydrogel-based ECL biosensor

The plastic adhesive layer was removed to expose the bottom surface of the hydrogel, then the device was inserted in the black box with the auxiliary electrode at the top. For the quantification of hydrogen peroxide in the luminol-functionalized ECL biosensor, 40 µL of $H_2O_2$ standard solution or water (for blank) were dispensed on the hydrogel. After 15 min the solution was absorbed into the hydrogel, and two image acquisitions (60 s exposure time, ISO 3200 sensitivity) were performed with the smartphone. The first image was acquired without applied voltage, while the second one was acquired with the 1.5 V voltage applied to the ECL device. For the quantification of glucose in the luminol/GO-functionalized ECL biosensor, 40 µL of glucose standard solution, water (for blank) or sample (if necessary, diluted with water) were dispensed on the hydrogel, then the measure was performed as described before.

For each experiment the acquired images were analysed to evaluate the signal (the first image provided for the value of the background, which was subtracted from the signal calculated for the second image to obtain the actual ECL signal of the experiment). Then, the $H_2O_2$ (or glucose)

calibration curves were generated by graphing the logarithm of the blank-subtracted ECL signal vs. the logarithm of analyte concentration and fitting the experimental data by a first-order polynomial equation, and the concentrations of unknown $H_2O_2$ (or glucose) samples were calculated by interpolation of their blank-subtracted ECL signals on the calibration curve.

## 3.3 Results and discussion

### 3.3.1 Solution-based ECL device

The ECL device employed a simple two-electrode configuration without any reference electrode [56], [57], [58]. Although in such configuration the potential of the working electrode cannot be controlled, this approach simplified both the ECL device and the analytical system (ECL measurements could be performed using a low-cost variable voltage power supply or even a 1.5V alkaline battery). The 3D printing technology allowed to produce a device with a complex shape (which included a measurement cell in which reagents and sample could be directly dispensed), using PLA, a (bio)polyester that is considered an environment-friendly material.

#### 3.3.1.1 Optimization of experimental conditions

To characterize the ECL device we firstly studied the ECL emission as a function of the applied potential (with respect to an Ag/AgCl external reference electrode) in CV experiments. In agreement with literature data [52], [59], [60] the ECL emission vs. potential profile (Figure 3.2a) presented a peak starting at about 0.7 – 0.75 V vs. Ag/AgCl due to the oxidation of both luminol and $H_2O_2$. A summary of the reactions leading to the ECL signal generation, as hypothesized by Zhou et al. [60], is reported in Scheme 3.1. Taking into consideration such result, the ECL measurements in the device were performed by applying a 1.5 V voltage between the electrodes.

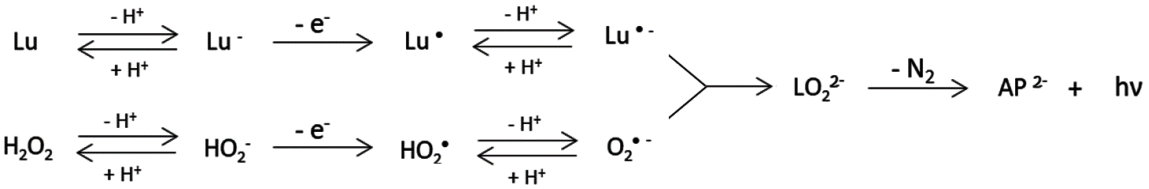


***Scheme 3.1.*** *Sequence of reactions leading to the generation of ECL emission by luminol and $H_2O_2$ in a carbonate buffer solution (pH 10.8) according to the mechanism proposed in Zhou et al.[60] Lu: luminol, Lu-: luminol anion, Lu•: luminol radical, Lu•-: luminol radical, $Lu^{\bullet-}$: luminol radical anion, $H_2O_2$: hydrogen peroxide, $HO_2^-$: hydrogen peroxide anion, $HO_2^\bullet$: hydrogen peroxide radical, $O_2^{\bullet-}$: superoxide radical anion, $LO_2^{2-}$: luminol peroxide compound, $AP^{2-}$: 3-aminophthalate dianion.*

Imaging measurements were also performed during CV/ECL experiments to assess the spatial localization of the ECL emission, which, as expected, was produced at the anode of the ECL device (Figures 3.2b and 3.2c).

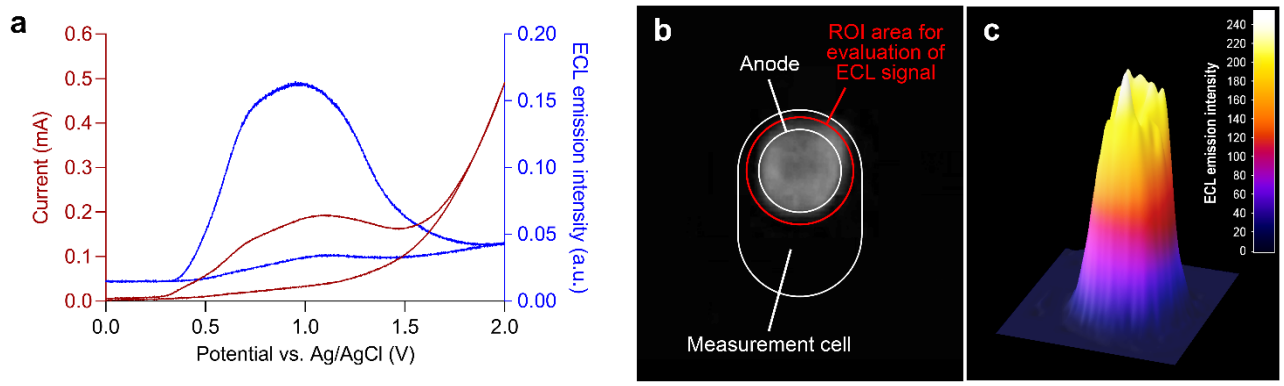


***Figure 3.2.*** *(a) Profiles of current (red trace) and ECL emission intensity (blue trace) recorded in a CV/ECL experiment performed in the ECL device. (b) Image and (c) profile of the spatial distribution of the ECL emission (the real dimensions of the measurement cell and of the anode of the ECL device, as well the integration area used for the evaluation of the signal, are also shown). The measurements were carried out in carbonate buffer at pH 10.8 containing 5.0 mmol $L^{-1}$ luminol and 0.1 mmol $L^{-1}$ $H_2O_2$.*

The ECL signal of the luminol/$H_2O_2$ system is strongly influenced by the luminol concentration and the pH of the working medium.

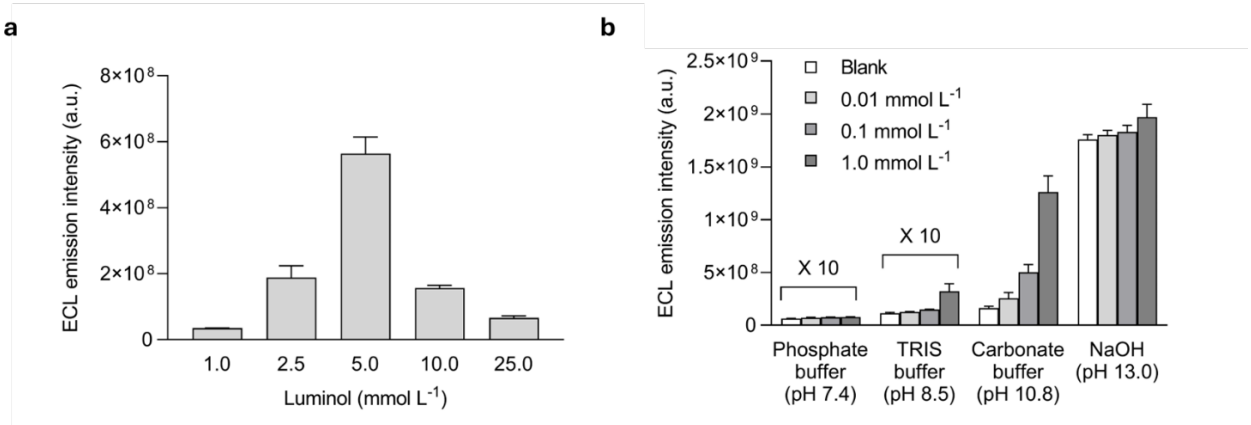


***Figure 3.3.*** *(a) ECL maximum emission intensities obtained for a 0.1 mmol $L^{-1}$ $H_2O_2$ solution in the presence of different luminol concentrations. The measurements were carried out in carbonate buffer at pH 10.8. (b) ECL maximum emission intensities obtained at different pH values in the presence of 5.0 mmol $L^{-1}$ luminol and various concentrations of $H_2O_2$ (the ECL signals obtained in phosphate and TRIS buffers were plotted at ten times their real intensities). Each data is the mean ± SD of three independent measurements.*

Figure 3.3a reports the ECL emissions obtained in 0.1 mmol $L^{-1}$ $H_2O_2$ solutions containing different concentrations of luminol. An increase of the ECL emission intensity with the concentration of luminol has been observed up to 5.0 mmol $L^{-1}$, while more concentrated luminol solutions gave weaker ECL signals, which can be ascribed to a self-quenching effect [61]. Based on these results, a 5.0 mmol $L^{-1}$ luminol concentration was selected to be used in the ECL device.

Once established the optimal luminol concentration, the effect of pH on the ECL emission was investigated.

It is indeed known that the luminol/$H_2O_2$ ECL system is more efficient at alkaline pH because the oxidized, unprotonated form of luminol (diazaquinone) reacts with the $HO_2^-$ anion [52]. To this end, ECL measurements were performed in 0.1 mol $L^{-1}$ buffer solutions with pH values ranging from 7.4 to 10.8 and in NaOH solution at pH 13.0, either without or with different concentrations of $H_2O_2$ to also evaluate the dynamic range of the $H_2O_2$ ECL assay. As shown in Figure 3.3b, at lower pH values (pH 7.4 and 8.5) weak ECL signals were obtained and the signal due to oxidation of hydrogen peroxide could not be discriminated from the blank, except at the highest concentration. The measurements performed at pH 10.8 provided much intense ECL signals as well as an evident increasing trend with the concentration of hydrogen peroxide. The ECL signals were even higher at pH 13.0, however the dynamic range was reduced because of the intense blank signal. Therefore, the carbonate buffer was selected as that providing the widest dynamic range of the hydrogen peroxide assay. This finding is in line with the literature since pH values around 10 were found to provide the highest signal-to-background ratios for the luminol/$H_2O_2$ CL [11] and ECL systems [60].

### 3.3.1.2 Quantification of hydrogen peroxide

As a preliminary step for the development of the glucose ECL biosensor, the performance of the ECL device in the quantification of $H_2O_2$ was evaluated. Figures 3.4a and 3.4b show, respectively, the kinetic profiles of the ECL emissions obtained by analysing $H_2O_2$ standard solutions and the corresponding $H_2O_2$ calibration curve (the evaluation of the ECL signal as the integral of the ECL emission over a 60 s-time interval starting from the application of the voltage to the ECL device was preferred to the measurement of the peak ECL intensity since it reduced data variability). A good correlation between the ECL analytical signal and the logarithm of the $H_2O_2$ concentration was found in the 0.05 – 5.0 mmol $L^{-1}$ concentration interval, and the detection limit (LOD) of the assay (estimated as the concentration of $H_2O_2$ giving a signal corresponding to that of the blank plus three times its standard deviation) was about 40 µmol $L^{-1}$.

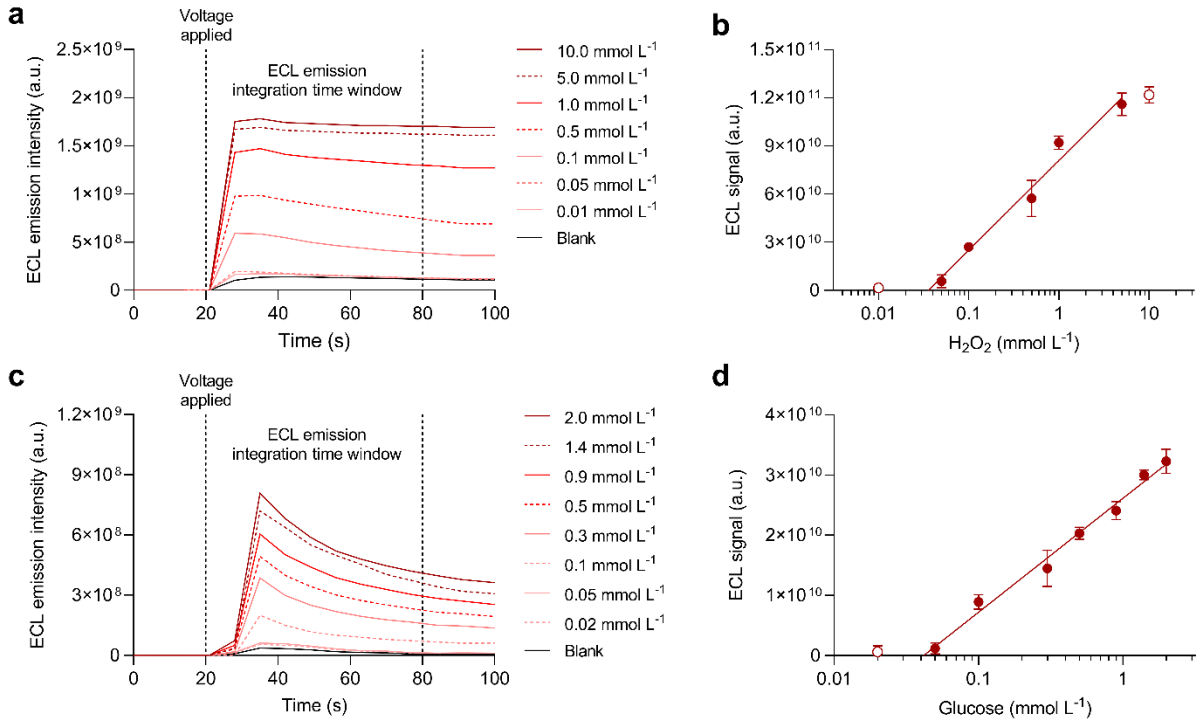


***Figure 3.4.*** *(a) Kinetic profiles of the ECL emission obtained for the analysing samples with different concentrations of $H_2O_2$ with the solution ECL device and (b) corresponding calibration curve for $H_2O_2$. The equation of the calibration curve in the 0.05 - 5.0 mmol $L^{-1}$ concentration interval (filled circles) is Y = (5.60 ± 0.51) × $10^{10}$ X + (8.09 ± 0.41) × $10^{10}$ ($R^2$ = 0.97), where Y and X are the ECL signal (after blank subtraction) and the logarithm of the concentration of $H_2O_2$ (mmol $L^{-1}$), respectively.(c) Kinetic profiles of the ECL emission obtained for the analysis of samples with different glucose concentrations with the solution ECL device and (d) corresponding calibration curve for glucose. The equation of the calibration curve in the 0.05 - 2.0 mmol $L^{-1}$ concentration interval (filled circles) is Y = (1.89 ± 0.09) × $10^{10}$ X + (2.61 ± 0.06) × $10^{10}$ ($R^2$ = 0.99), where Y and X are the ECL signal (after blank subtraction) and the logarithm of the concentration of glucose (mmol $L^{-1}$), respectively. Each data is the mean ± SD of three independent measurements.*

### 3.3.1.3 Quantification of glucose

The ECL biosensor for glucose was designed to exploit an endpoint assay, i.e., the glucose was completely oxidized to gluconic acid and hydrogen peroxide in the GO-catalysed enzyme reaction before performing the ECL measurement of $H_2O_2$. This increased assay sensitivity (the amount of $H_2O_2$ to be detected is the highest possible) but required a preliminary incubation step (15 min in our case) for glucose oxidation. In addition, the optimal pH for the GO-catalysed enzyme reaction is slightly acidic, even a quite broad pH range of activity (pH 4 – 7) has been reported [62]. Therefore, the incubation step was carried out at pH 7.0, then the pH value was adjusted to 10.8 by adding a concentrated carbonate buffer solution prior to ECL measurement [63].

Figure 3.4c shows the kinetic profiles of the ECL emissions obtained by analysing glucose standard solutions. The behaviour of the kinetic profiles was like that found for the $H_2O_2$ assay, even though the decrease of the ECL emission with time was slightly faster. The corresponding glucose calibration curve (Figure 3.4d) covered the 0.05 – 2.0 mmol $L^{-1}$ concentration interval, with a CV% below 10%. The LOD of the assay (about 50 µmol $L^{-1}$ of glucose) was of the same order of magnitude of that found for $H_2O_2$. The performance of the ECL glucose biosensor was also tested in real samples. Glucose saline solutions with glucose contents ranging from 5% to 70% (m/v) were diluted 1:2000 (v/v) with water before the analysis to obtain final glucose concentrations within the assay calibration range (this also reduced the concentrations of other matrix components, thus minimizing a possible matrix effect). In addition, as an example of a possible application of this device in the clinical field, we analysed glucose-spiked artificial serum samples (to comply with the calibration range of the ECL device, samples were preliminarily diluted 1:10 (v/v) with water). Table 3.1 shows the comparison between the glucose concentrations measured with the ECL device and the glucose contents, which have been also confirmed by using a reference enzymatic colorimetric assay. The recovery values varied between 86% and 112% and the assay reproducibility was satisfactory (CV% not higher than 10%), thus indicating the applicability of the ECL biosensor for the quantification of glucose in real matrices.

***Table 3.1.*** *Results obtained by analysing real samples.* [a]

| **Glucose saline solutions** [b] | | | | | | |
|---|---|---|---|---|---|---|
| | | **Solution-based ECL device** | | **Hydrogel-based ECL device** | | **Reference assay** |
| **Sample no.** | **Nominal glucose concentration (%(m/v))** | **Measured glucose concentration (% (m/v))** | **Recovery (%)** | **Measured glucose concentration (% (m/v))** | **Recovery (%)** | **Measured glucose concentration (% (m/v))** |
| #1 | 5.0 | 4.3 ± 0.1 | 86% | 4.5 ± 0.4 | 90% | 4.8 ± 0.1 |
| #2 | 10.0 | 10.5 ± 0.7 | 105% | 10.3 ± 0.7 | 103% | 10.2 ± 0.4 |
| #3 | 20.0 | 21.2 ± 0.6 | 106% | 22.0 ± 1.1 | 110% | 20.5 ± 0.6 |
| #4 | 33.0 | 30.0 ± 1.3 | 91% | 30.9 ± 2.6 | 94% | 32.2 ± 0.5 |
| #5 | 50.0 | 48.9 ± 1.9 | 98% | 47.9 ± 2.9 | 96% | 49.3 ± 0.9 |
| #6 | 70.0 | 78.1 ± 4.4 | 112% | 76.3 ± 5.8 | 109% | 72.8 ± 1.7 |

| Glucose-spiked artificial serum samples [c] | | | | | | |
|---|---|---|---|---|---|---|
| | | Solution-based ECL device | | Hydrogel-based ECL device | | Reference assay |
| Sample no. | Spiked glucose concentration (mmol $L^{-1}$) | Measured glucose concentration (mmol $L^{-1}$) | Recovery (%) | Measured glucose concentration (mmol $L^{-1}$) | Recovery (%) | Measured glucose concentration (mmol $L^{-1}$) |
| #1 | 1.0 | 1.1 ± 0.1 | 110% | 1.1 ± 0.1 | 110% | 0.9 ± 0.1 |
| #2 | 5.0 | 5.4 ± 0.2 | 108% | 5.2 ± 0.3 | 104% | 5.1 ± 0.1 |
| #3 | 10.0 | 10.2 ± 0.5 | 102% | 10.3 ± 0.7 | 103% | 10.1 ± 0.3 |

[a] Results are the mean ± SD of three independent measurements. [b] Glucose saline solutions were diluted 1:2000 (v/v) with water before analysis. [c] Spiked artificial serum samples were diluted 1:10 (v/v) with water before analysis.

### 3.3.2 Hydrogel-based ECL device

To obtain an ECL glucose biosensor suitable for onsite application, we further simplified the analytical system by employing a 1.5 V AA alkaline battery to provide the voltage and using a smartphone for measuring the ECL emission. A 3D-printed dark box was designed to employ a Samsung S20 smartphone for the measurement (however, the dark box could be adapted with minimal modifications to other smartphones).

We also investigated the possibility to preload the reagents in the device within a hydrogel matrix, which will allow to prepare in advance the ECL devices and reduce the analytical procedure to the sample addition, incubation, and measurement steps. The prerequisites for the hydrogel matrix were inertness towards analytes, reagents, and electrode materials, as well as suitability as a reaction medium for the enzyme reaction and the ECL detection of hydrogen peroxide. Low-cost and environmental friendliness were also desirable characteristics. Based on these requirements, agarose was selected as the best candidate. Agarose gels are cheap, non-toxic, easy to prepare, exhibit thermo-reversible gelation, and are highly transparent in the visible range, thus allowing transmission and imaging of the optical signal [14], [64], [65], [66]. Moreover, the agarose hydrogel acts as a protective carrier for the enzyme and enable easy diffusion of low molecular weight molecules such as glucose, $H_2O_2$, and luminol, thus ensuring a rapid response of the ECL biosensor.

### 3.3.2.1 Quantification of hydrogen peroxide

The hydrogel-based ECL device was preliminarily characterized to assess the effect of the hydrogel matrix on its performance. The CV/ECL experiments performed in the presence of $H_2O_2$ indicated that the maximum ECL emission intensity is obtained at a potential of about 0.75 V vs. Ag/AgCl, thus close to the value found for the solution ECL device (Figure 3.5a). Notice that the maximum of ECL intensity for the hydrogel device is two times higher compared with conventional ECL device (see Figure 3.2a) with almost the same current involved as evidence of higher performance of hydrogel-based sensor. Furthermore, the ECL emission kinetics was unaffected by the hydrogel matrix (Figure 3.5b); since the peak ECL signal was reached a few seconds after voltage application, a 60-s ECL signal acquisition time was used also for smartphone-based experiments.

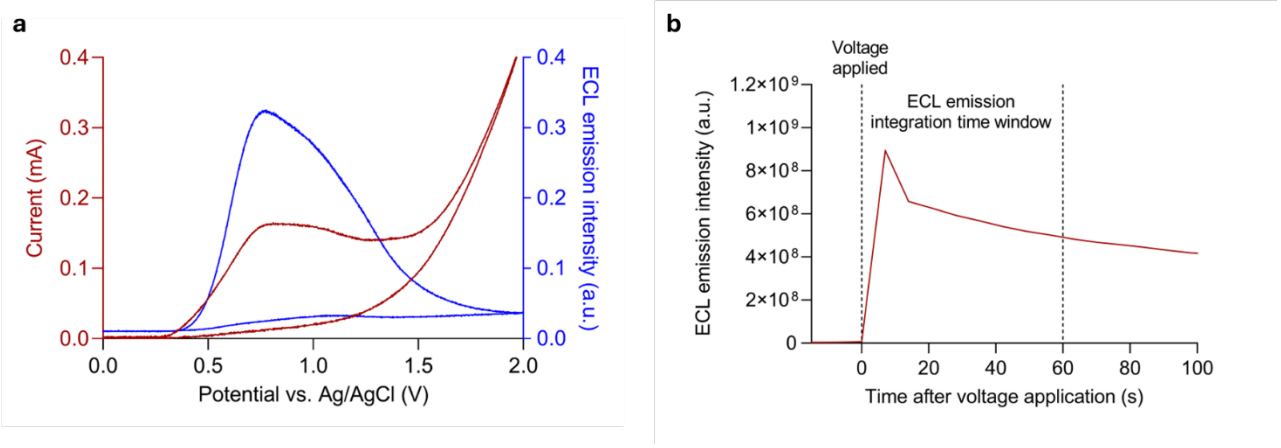


***Figure 3.5.*** *(a) Profiles of current (red trace) and ECL emission intensity (blue trace) recorded in a CV/ECL experiment performed in the hydrogel ECL device and (b) kinetic profiles of the ECL emission. The measurements were carried out by employing a 0.1 mmol $L^{-1}$ $H_2O_2$ standard solution.*

Then, the ECL device with luminol-loaded hydrogel was employed for analysing $H_2O_2$ standard solutions employing the 3D printed dark box and smartphone based ECL detection. Figure 3.6a shows the $H_2O_2$ calibration curve, which indicated an excellent linearity of response in the range 0.2 – 2.0 mmol $L^{-1}$ of $H_2O_2$, as well as a LOD of 30 µmol $L^{-1}$ of $H_2O_2$.

### 3.3.2.2 Quantification of glucose

Then, the ECL device with luminol/GO-loaded hydrogel was employed for glucose quantification. Figures 3.6b and 3.6c show, respectively, the ECL images acquired by analysing glucose standard solutions with concentrations ranging from 0.05 to 5.0 mmol $L^{-1}$ and the corresponding glucose calibration curve.

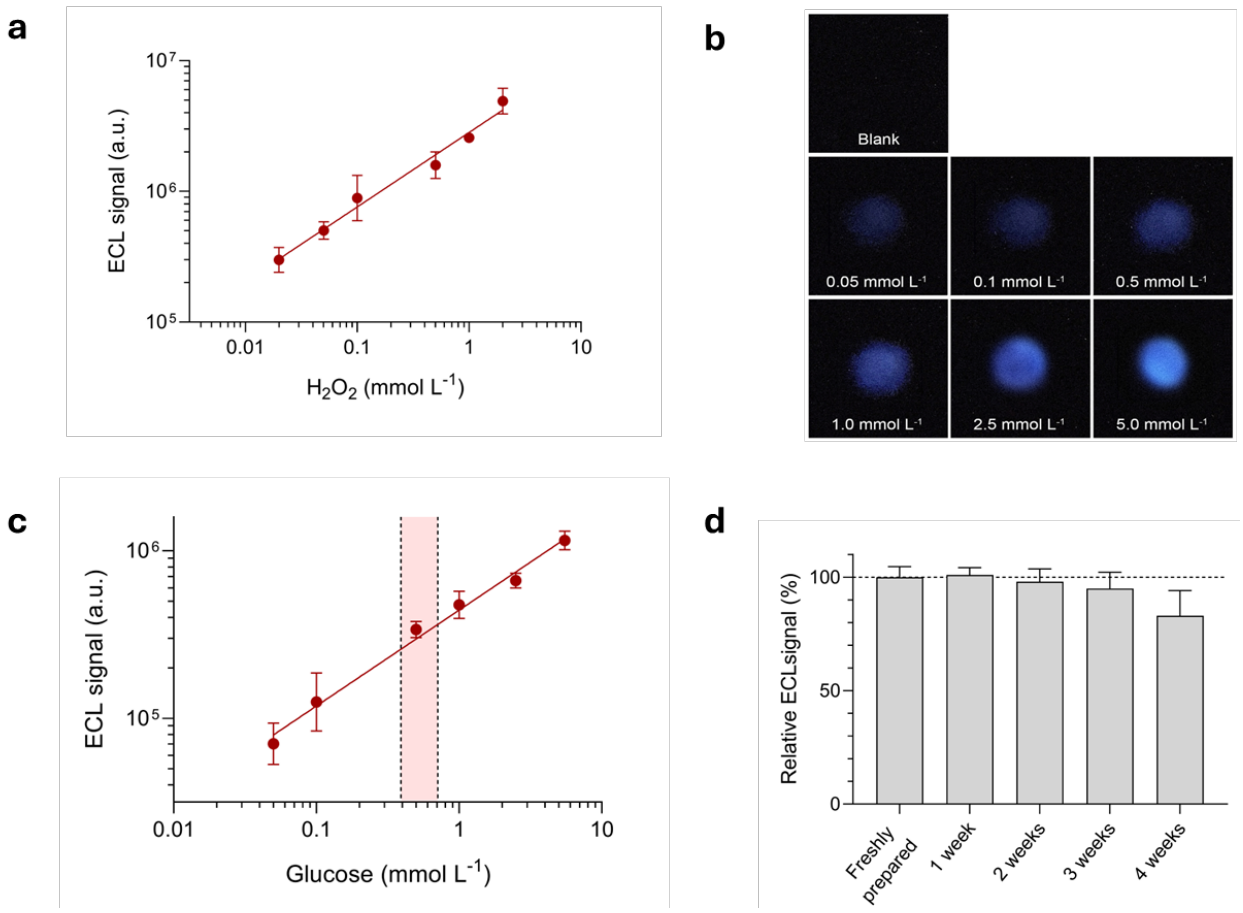


***Figure 3.6.*** *(a) Calibration curve for the analysis of $H_2O_2$ obtained using the hydrogel-based ECL device. The equation of the calibration curve in the 0.01 – 2.0 mmol $L^{-1}$ concentration interval is $Y = (0.57 \pm 0.04) X + (6.45 \pm 0.04)$ ($R^2 = 0.98$), where Y and X are the logarithms of the ECL signal (after blank subtraction) and the concentration of $H_2O_2$ (mmol $L^{-1}$), respectively. (b) ECL images acquired with the smartphone during the analysis of glucose standard solutions. (c) Calibration curve for the analysis of glucose obtained using the hydrogel-based ECL device. The equation of the calibration curve in the 0.05 - 5.0 mmol $L^{-1}$ concentration interval is $Y = (1.89 \pm 0.09) \times 10^{10} X + (2.61 \pm 0.06) \times 10^{10}$ ($R^2 = 0.99$), where Y and X are the logarithms of the ECL signal (after blank subtraction) and the concentration of glucose (mmol $L^{-1}$), respectively. The shaded area indicates the expected range of blood glucose concentrations of healthy subjects upon 1:10 (v/v) dilution (as described in the text). (d) ECL signals obtained by analysing a 5 mmol $L^{-1}$ glucose solution employing hydrogel-based ECL devices stored in sealed plastic bags and in the dark at +4°C for different times. Each data is the mean ± SD of three independent measurements.*

By combining the end-point enzymatic method for glucose in the hydrogel matrix with the smartphone-based ECL detection of $H_2O_2$ a response proportional to the glucose concentration was obtained. The LOD of the assay (60 µmol $L^{-1}$ of glucose) was almost the same found for the solution-based ECL device. It is worthwhile to note that in the hydrogel ECL device the GO-catalysed enzymatic reaction could be carried out at the alkaline pH required for the ECL measurement. Indeed, the coupling of the detection of $H_2O_2$ by luminol's ECL with enzyme-catalysed reactions is often

complicated by the requirement of a physiological pH for optimal enzyme activity [67]. In such cases the enzyme reaction is often performed at a first stage and then the products are applied at the electrochemical cell [66]. The observation of GO enzyme activity at pH 10.8 is in line with previously reported findings showing that enzymes trapped in hydrogels displayed higher activity and increased tolerance to temperature and pH variation if compared to the free enzyme [68].

To evaluate applicability of the biosensor, the real samples reported in paragraph 3.3.1.3, i.e., glucose saline solutions and glucose-spiked artificial serum samples were analysed. As shown in Table 3.1, there was a quite good correspondence between the measured glucose concentrations and the expected values (recoveries ranged from 90% to 110%), and the assay reproducibility was satisfactory (CV% not higher than 10%).

The obtained results suggested the applicability of the hydrogel-based ECL device for assessing glucose blood levels. Furthermore, by considering that the expected blood glucose levels in healthy subjects are in the 3.9 – 7.1 mmol $L^{-1}$ range [69], both hypoglycaemic and hyperglycaemic samples could be discriminated, in agreement with standard commercial glucometers (1,1 – 33.3 mmol $L^{-1}$).

The specificity of the ECL biosensor was evaluated by measuring the ECL signal corresponding to 0.2 mmol $L^{-1}$ glucose in the presence of various interferents at the same concentration. Substances with reducing activity were tested, namely glycine, alanine, phenylalanine, dopamine, ascorbic acid, and uric acid. No interference was observed, as the biosensor response varied not more than 5% with respect to the glucose solution without interferents.

The stability of the hydrogel-based ECL device was evaluated by measuring the changes in the ECL signal obtained using devices stored in sealed plastic bags and in the dark at +4°C for different times, up to four weeks. The response of biosensor was maintained for at least 3 weeks, showing the ability of the agarose gelled medium to preserve enzyme activity and reagents stability, as reported in Figure 3.6d.

## 3.4 Conclusions

In this work an ECL-based enzymatic biosensor for glucose quantification was developed through a low-cost 3D printing technology and using a PLA sustainable polymer. The protocol for the detection of hydrogen peroxide based on the luminol/$H_2O_2$ ECL system was optimised and then applied for the quantification of $H_2O_2$ produced in the enzymatic oxidation of glucose catalysed by GO.

The biosensor performance was initially evaluated using a CCD for ECL signal detection and a feasibility study was carried out for the quantification of glucose in pharmaceutical formulations. Since the use of a CCD camera reduced the portability of the biosensor and required expert personnel for the acquisition, processing and interpretation of the results, a further step towards the development of a real point-of-need analytical system was the implementation of a smartphone based ECL signal measurement. In addition, the development of an ECL device containing a hydrogel matrix with preloaded reagents for a single-use disposable assay made it possible to considerably simplify the analytical protocol, which required only the addition of the sample (possibly preceded by its appropriate dilution). As an example of a possible point-of-care application of this analytical system, glucose-spiked artificial serum samples were analysed obtaining satisfactory results. With respect to previously reported ECL-based biosensors for glucose, the developed device enables easy and reproducible rapid prototyping of electrode components by 3D printing and reagents preloading in a hydrogel matrix for convenient POC application. The developed device could therefore represent an advancement in the field of portable and low-cost ECL-based analytical systems and, although it has been used for glucose quantification, its application can in principle be extended to all those substrates that are converted into hydrogen peroxide by oxidases or for which there is a specific enzymatic reaction that can be coupled to a secondary reaction catalysed by an oxidase. In addition, the future combination of this platform with paper-based substrates would enhance its sustainable feature.

## 3.5 Acknowledgements

This research was funded by the Italian Ministry of University and Research: PRIN2017 project “Cutting edge analytical chemistry methodologies and bio-tools to boost precision medicine in hormone-related diseases”, Prot. 2017Y2PAB8; and PRIN2017 project “Functional 3D architectures for electrochemiluminescence applications”, Prot. 2017FJCPEX.

## 3.6 References


[1] M. A. Ali *et al.*, "Recent Advances in 3D Printing of Biomedical Sensing Devices," *Adv Funct Mater*, vol. 32, no. 9, p. 2107671, Feb. 2022, doi: 10.1002/ADFM.202107671.

[2] C. L. Manzanares Palenzuela and M. Pumera, "(Bio)Analytical chemistry enabled by 3D printing: Sensors and biosensors," *TrAC Trends in Analytical Chemistry*, vol. 103, pp. 110–118, Jun. 2018, doi: 10.1016/J.TRAC.2018.03.016.

[3] S. Arshavsky-Graham, A. Enders, S. Ackerman, J. Bahnemann, and E. Segal, "3D-printed microfluidics integrated with optical nanostructured porous aptasensors for protein detection," *Microchimica Acta*, vol. 188, no. 3, pp. 1–12, Mar. 2021, doi: 10.1007/S00604-021-04725-0/FIGURES/5.

[4] D. Calabria *et al.*, "Paper-based smartphone chemosensor for reflectometric on-site total polyphenols quantification in olive oil," *Sens Actuators B Chem*, vol. 305, p. 127522, Feb. 2020, doi: 10.1016/J.SNB.2019.127522.

[5] A. Chiadò *et al.*, "A modular 3D printed lab-on-a-chip for early cancer detection," *Lab Chip*, vol. 20, no. 3, pp. 665–674, Feb. 2020, doi: 10.1039/C9LC01108K.

[6] K. Kadimisetty, S. Malla, and J. F. Rusling, "Automated 3-D Printed Arrays to Evaluate Genotoxic Chemistry: E-Cigarettes and Water Samples," *ACS Sens*, vol. 2, no. 5, pp. 670–678, May 2017, doi: 10.1021/ACSSENSORS.7B00118.

[7] H. Van Nguyen, V. D. Nguyen, E. Y. Lee, and T. S. Seo, "Point-of-care genetic analysis for multiplex pathogenic bacteria on a fully integrated centrifugal microdevice with a large-volume sample," *Biosens Bioelectron*, vol. 136, pp. 132–139, Jul. 2019, doi: 10.1016/J.BIOS.2019.04.035.

[8] M. Zangheri *et al.*, "Chemiluminescence-based biosensor for monitoring astronauts' health status during space missions: Results from the International Space Station," *Biosens Bioelectron*, vol. 129, pp. 260–268, Mar. 2019, doi: 10.1016/J.BIOS.2018.09.059.

[9] C. Lertvachirapaiboon, A. Baba, K. Shinbo, and K. Kato, "Dual-mode surface plasmon resonance sensor chip using a grating 3D-printed prism," *Anal Chim Acta*, vol. 1147, pp. 23–29, Feb. 2021, doi: 10.1016/J.ACA.2020.12.027.

[10] A. Roda *et al.*, "A simple smartphone-based thermochemiluminescent immunosensor for valproic acid detection using 1,2-dioxetane analogue-doped nanoparticles as a label," *Sens Actuators B Chem*, vol. 279, pp. 327–333, Jan. 2019, doi: 10.1016/J.SNB.2018.10.012.

[11] D. Calabria *et al.*, "Smartphone-Based Chemiluminescent Origami μPAD for the Rapid Assessment of Glucose Blood Levels," *Biosensors 2021, Vol. 11, Page 381*, vol. 11, no. 10, p. 381, Oct. 2021, doi: 10.3390/BIOS11100381.

[12] W. Q. Lai, Y. F. Chang, F. N. Chou, and D. M. Yang, "Portable FRET-Based Biosensor Device for On-Site Lead Detection," *Biosensors (Basel)*, vol. 12, no. 3, p. 157, Mar. 2022, doi: 10.3390/BIOS12030157/S1.

[13] X. Li, F. Yang, J. X. H. Wong, and H. Z. Yu, "Integrated Smartphone-App-Chip System for On-Site Parts-Per-Billion-Level Colorimetric Quantitation of Aflatoxins," *Anal Chem*, vol. 89, no. 17, pp. 8908–8916, Sep. 2017, doi: 10.1021/ACS.ANALCHEM.7B01379.

[14] D. Calabria *et al.*, "A smartphone-based chemosensor to evaluate antioxidants in agri-food matrices by in situ AuNP formation," *Sensors*, vol. 21, no. 16, p. 5432, Aug. 2021, doi: 10.3390/S21165432/S1.

[15] D. Yi, Z. Liu, T. Liu, S. Zhang, H. Ding, and W. Wang, "Development of a handheld dual-channel optical fiber fluorescence sensor based on a smartphone," *Applied Optics, Vol. 59, Issue 3, pp. 601-606*, vol. 59, no. 3, pp. 601–606, Jan. 2020, doi: 10.1364/AO.378622.

[16] F. Mustafa, M. Carhart, and S. Andreescu, "A 3D-Printed Breath Analyzer Incorporating CeO2 Nanoparticles for Colorimetric Enzyme-Based Ethanol Sensing," *ACS Appl Nano Mater*, vol. 4, no. 9, pp. 9361–9369, Sep. 2021, doi: 10.1021/ACSANM.1C01826.

[17] A. Kalkal *et al.*, "Recent advances in 3D printing technologies for wearable (bio)sensors," *Addit Manuf*, vol. 46, p. 102088, Oct. 2021, doi: 10.1016/J.ADDMA.2021.102088.

[18] R. M. Cardoso *et al.*, "Additive-manufactured (3D-printed) electrochemical sensors: A critical review," *Anal Chim Acta*, vol. 1118, pp. 73–91, Jun. 2020, doi: 10.1016/J.ACA.2020.03.028.

[19] A. M. López Marzo, C. C. Mayorga-Martinez, and M. Pumera, "3D-printed graphene direct electron transfer enzyme biosensors," *Biosens Bioelectron*, vol. 151, p. 111980, Mar. 2020, doi: 10.1016/J.BIOS.2019.111980.

[20] M. H. Omar, K. A. Razak, M. N. Ab Wahab, and H. H. Hamzah, "Recent progress of conductive 3D-printed electrodes based upon polymers/carbon nanomaterials using a fused deposition modelling (FDM) method as emerging electrochemical sensing devices," *RSC Adv*, vol. 11, no. 27, pp. 16557–16571, Apr. 2021, doi: 10.1039/D1RA01987B.

[21] L. R. G. Silva *et al.*, "Electrochemical Biosensor for SARS-CoV-2 cDNA Detection Using AuPs-Modified 3D-Printed Graphene Electrodes," *Biosensors (Basel)*, vol. 12, no. 8, p. 622, Aug. 2022, doi: 10.3390/BIOS12080622/S1.

[22] M. M. Richter, "Electrochemiluminescence (ECL)," *Chem Rev*, vol. 104, no. 6, pp. 3003–3036, Jun. 2004, doi: 10.1021/CR020373D.

[23] W. Miao, "Electrogenerated Chemiluminescence and Its Biorelated Applications," *Chem Rev*, vol. 108, no. 7, pp. 2506–2553, Jul. 2008, doi: 10.1021/CR068083A.

[24] A. Fiorani *et al.*, "Advanced carbon nanomaterials for electrochemiluminescent biosensor applications," *Curr Opin Electrochem*, vol. 16, pp. 66–74, Aug. 2019, doi: 10.1016/J.COELEC.2019.04.018.

[25] H. Qi and C. Zhang, "Electrogenerated Chemiluminescence Biosensing," *Anal Chem*, vol. 92, no. 1, pp. 524–534, Jan. 2019, doi: 10.1021/ACS.ANALCHEM.9B03425.

[26] S. M. Yoo, Y. M. Jeon, and S. Y. Heo, "Electrochemiluminescence Systems for the Detection of Biomarkers: Strategical and Technological Advances," *Biosensors 2022, Vol. 12, Page 738*, vol. 12, no. 9, p. 738, Sep. 2022, doi: 10.3390/BIOS12090738.

[27] F. Du, Y. Chen, C. Meng, B. Lou, W. Zhang, and G. Xu, "Recent advances in electrochemiluminescence immunoassay based on multiple-signal strategy," *Curr Opin Electrochem*, vol. 28, p. 100725, Aug. 2021, doi: 10.1016/J.COELEC.2021.100725.

[28] M. Hesari and Z. Ding, "Review—Electrogenerated Chemiluminescence: Light Years Ahead," *J Electrochem Soc*, vol. 163, no. 4, p. H3116, Dec. 2015, doi: 10.1149/2.0161604JES.

[29] W. Lv, H. Ye, Z. Yuan, X. Liu, X. Chen, and W. Yang, "Recent advances in electrochemiluminescence-based simultaneous detection of multiple targets," *TrAC Trends in Analytical Chemistry*, vol. 123, p. 115767, Feb. 2020, doi: 10.1016/J.TRAC.2019.115767.

[30] H. Nasrollahpour, B. Khalilzadeh, A. Naseri, M. Sillanpää, and C. H. Chia, "Homogeneous Electrochemiluminescence in the Sensors Game: What Have We Learned from Past

Experiments?," *Anal Chem*, vol. 94, no. 1, pp. 349–365, Jan. 2021, doi: 10.1021/ACS.ANALCHEM.1C03909.

[31] Z. Liu, W. Qi, and G. Xu, "Recent advances in electrochemiluminescence," *Chem Soc Rev*, vol. 44, no. 10, pp. 3117–3142, May 2015, doi: 10.1039/C5CS00086F.

[32] Neso. Sojic, "Analytical Electrogenerated Chemiluminescence: From Fundamentals to Bioassays," p. 501, 2020, Accessed: Sep. 16, 2025. [Online]. Available: https://books.google.com/books/about/Analytical_Electrogenerated_Chemilumines.html?hl=it&id=wDbBDwAAQBAJ

[33] X. Ma *et al.*, "Rational Design of Electrochemiluminescent Devices," *Acc Chem Res*, vol. 54, no. 14, pp. 2936–2945, Jul. 2021, doi: 10.1021/ACS.ACCOUNTS.1C00230.

[34] E. H. Doeven *et al.*, "Mobile phone-based electrochemiluminescence sensing exploiting the 'USB On-The-Go' protocol," *Sens Actuators B Chem*, vol. 216, pp. 608–613, Sep. 2015, doi: 10.1016/J.SNB.2015.04.087.

[35] W. Gao, K. Muzyka, X. Ma, B. Lou, and G. Xu, "A single-electrode electrochemical system for multiplex electrochemiluminescence analysis based on a resistance induced potential difference," *Chem Sci*, vol. 9, no. 16, pp. 3911–3916, Apr. 2018, doi: 10.1039/C8SC00410B.

[36] P. Nikolaou *et al.*, "Ultrasensitive PCR-Free detection of whole virus genome by electrochemiluminescence," *Biosens Bioelectron*, vol. 209, p. 114165, Aug. 2022, doi: 10.1016/J.BIOS.2022.114165.

[37] P. Pittet *et al.*, "A novel low-cost approach of implementing electrochemiluminescence detection for microfluidic analytical systems," *Materials Science and Engineering: C*, vol. 28, no. 5–6, pp. 891–895, Jul. 2008, doi: 10.1016/J.MSEC.2007.10.030.

[38] X. Huang *et al.*, "Smartphone-based analytical biosensors," *Analyst*, vol. 143, no. 22, pp. 5339–5351, Nov. 2018, doi: 10.1039/C8AN01269E.

[39] D. Quesada-González and A. Merkoçi, "Mobile phone-based biosensing: An emerging 'diagnostic and communication' technology," *Biosens Bioelectron*, vol. 92, pp. 549–562, Jun. 2017, doi: 10.1016/J.BIOS.2016.10.062.

[40] J. L. Delaney, C. F. Hogan, J. Tian, and W. Shen, “Electrogenerated Chemiluminescence Detection in Paper-Based Microfluidic Sensors,” *Anal Chem*, vol. 83, no. 4, pp. 1300–1306, Feb. 2011, doi: 10.1021/AC102392T.

[41] S. Li *et al.*, “Electrogenerated chemiluminescence on smartphone with graphene quantum dots nanocomposites for Escherichia Coli detection,” *Sens Actuators B Chem*, vol. 297, p. 126811, Oct. 2019, doi: 10.1016/J.SNB.2019.126811.

[42] Y. Yao, H. Li, D. Wang, C. Liu, and C. Zhang, “An electrochemiluminescence cloth-based biosensor with smartphone-based imaging for detection of lactate in saliva,” *Analyst*, vol. 142, no. 19, pp. 3715–3724, Sep. 2017, doi: 10.1039/C7AN01008G.

[43] Y. Zhang *et al.*, “Deep learning-assisted smartphone-based molecularly imprinted electrochemiluminescence detection sensing platform: Protable device and visual monitoring furosemide,” *Biosens Bioelectron*, vol. 209, p. 114262, Aug. 2022, doi: 10.1016/J.BIOS.2022.114262.

[44] G. W. Bishop, J. E. Satterwhite-Warden, I. Bist, E. Chen, and J. F. Rusling, “Electrochemiluminescence at Bare and DNA-Coated Graphite Electrodes in 3D-Printed Fluidic Devices,” *ACS Sens*, vol. 1, no. 2, pp. 197–202, Feb. 2015, doi: 10.1021/ACSSENSORS.5B00156.

[45] E. Climent and K. Rurack, “Combining Electrochemiluminescence Detection with Aptamer-Gated Indicator Releasing Mesoporous Nanoparticles Enables ppt Sensitivity for Strip-Based Rapid Tests,” *Angewandte Chemie International Edition*, vol. 60, no. 50, pp. 26287–26297, Dec. 2021, doi: 10.1002/ANIE.202110744.

[46] H. Motaghi, S. Ziyaee, M. A. Mehrgardi, A. A. Kajani, and A. K. Bordbar, “Electrochemiluminescence detection of human breast cancer cells using aptamer modified bipolar electrode mounted into 3D printed microchannel,” *Biosens Bioelectron*, vol. 118, pp. 217–223, Oct. 2018, doi: 10.1016/J.BIOS.2018.07.066.

[47] T. Zhan, Y. Su, W. Lai, Z. Chen, and C. Zhang, “A dry chemistry-based ultrasensitive electrochemiluminescence immunosensor for sample-to-answer detection of Cardiac Troponin I,” *Biosens Bioelectron*, vol. 214, p. 114494, Oct. 2022, doi: 10.1016/J.BIOS.2022.114494.

[48] M. Bhaiyya, M. B. Kulkarni, P. K. Pattnaik, and S. Goel, “Internet of things-enabled photomultiplier tube- and smartphone-based electrochemiluminescence platform to detect

choline and dopamine using 3D-printed closed bipolar electrodes," *Luminescence*, vol. 37, no. 2, pp. 357–365, Feb. 2022, doi: 10.1002/BIO.4179.

[49] M. Bhaiyya, P. K. Pattnaik, and S. Goel, "Multiplexed and simultaneous biosensing in a 3D-printed portable six-well smartphone operated electrochemiluminescence standalone point-of-care platform," *Microchimica Acta*, vol. 189, no. 2, pp. 1–9, Feb. 2022, doi: 10.1007/S00604-022-05200-0/FIGURES/5.

[50] S. F. Douman *et al.*, "Electrochemiluminescence at 3D Printed Titanium Electrodes," *Front Chem*, vol. 9, p. 662810, May 2021, doi: 10.3389/FCHEM.2021.662810/BIBTEX.

[51] C. Aymard *et al.*, "High-Throughput Electrochemical Screening Assay for Free and Immobilized Oxidases: Electrochemiluminescence and Intermittent Pulse Amperometry," *ChemElectroChem*, vol. 4, no. 4, pp. 957–966, Apr. 2017, doi: 10.1002/CELC.201600647.

[52] B. Leca-Bouvier, B. Doumèche, and L. J. Blum, "Enzymatic Assays," *RSC Detection Science*, vol. 2020-January, no. 15, pp. 331–385, Nov. 2019, doi: 10.1039/9781788015776-00331.

[53] I. Rahmawati, Y. Einaga, T. A. Ivandini, and A. Fiorani, "Enzymatic Biosensors with Electrochemiluminescence Transduction," *ChemElectroChem*, vol. 9, no. 12, p. e202200175, Jun. 2022, doi: 10.1002/CELC.202200175.

[54] M. Basiaga, Z. Paszenda, W. Walke, P. Karasiński, and J. Marciniak, "Electrochemical Impedance Spectroscopy and Corrosion Resistance of SiO2 Coated CpTi and Ti-6Al-7Nb Alloy," *Advances in Intelligent Systems and Computing*, vol. 284, pp. 411–420, 2014, doi: 10.1007/978-3-319-06596-0_39.

[55] A. Roda *et al.*, "Portable Device Based on Chemiluminescence Lensless Imaging for Personalized Diagnostics through Multiplex Bioanalysis," *Anal Chem*, vol. 83, no. 8, pp. 3178–3185, Apr. 2011, doi: 10.1021/AC200360K.

[56] C. Gao *et al.*, "Paper-Based Constant Potential Electrochemiluminescence Sensing Platform with Black Phosphorus as a Luminophore Enabled by a Perovskite Solar Cell," *Anal Chem*, vol. 92, no. 10, pp. 6822–6826, May 2020, doi: 10.1021/ACS.ANALCHEM.0C01033.

[57] J. Pan *et al.*, "A two-electrode system-based electrochemiluminescence detection for microfluidic capillary electrophoresis and its application in pharmaceutical analysis," *Luminescence*, vol. 29, no. 5, pp. 427–432, Aug. 2014, doi: 10.1002/BIO.2565.

[58] S. Wang *et al.*, “Rechargeable battery-triggered electrochemiluminescence detection on microfluidic origami immunodevice based on two electrodes,” *Chemical Communications*, vol. 48, no. 80, pp. 9971–9973, Sep. 2012, doi: 10.1039/C2CC34649D.

[59] P. Pittet, G. N. Lu, J. M. Galvan, R. Ferrigno, L. J. Blum, and B. Leca-Bouvier, “PCB-based integration of electrochemiluminescence detection for microfluidic systems,” *Analyst*, vol. 132, no. 5, pp. 409–411, Apr. 2007, doi: 10.1039/B701296A.

[60] P. Zhou, S. Hu, W. Guo, and B. Su, “Deciphering electrochemiluminescence generation from luminol and hydrogen peroxide by imaging light emitting layer,” *Fundamental Research*, vol. 2, no. 5, pp. 682–687, Sep. 2022, doi: 10.1016/J.FMRE.2021.11.018.

[61] H. R. Zhang, Y. Z. Wang, W. Zhao, J. J. Xu, and H. Y. Chen, “Visual Color-Switch Electrochemiluminescence Biosensing of Cancer Cell Based on Multichannel Bipolar Electrode Chip,” *Anal Chem*, vol. 88, no. 5, pp. 2884–2890, Mar. 2016, doi: 10.1021/ACS.ANALCHEM.5B04716.

[62] H. Tsuge, O. Natsuaki, and K. Ohashi, “Purification, Properties, and Molecular Features of Glucose Oxidase from Aspergillus niger,” *The Journal of Biochemistry*, vol. 78, no. 4, pp. 835–843, Oct. 1975, doi: 10.1093/OXFORDJOURNALS.JBCHEM.A130974.

[63] S. A. Kitte *et al.*, “Stainless Steel Electrode for Sensitive Luminol Electrochemiluminescent Detection of H2O2, Glucose, and Glucose Oxidase Activity,” *Anal Chem*, vol. 89, no. 18, pp. 9864–9869, Sep. 2017, doi: 10.1021/ACS.ANALCHEM.7B01939.

[64] P. T. Nguyen, H. T. Ahn, and M. Il Kim, “Reagent-Free Colorimetric Assay for Galactose Using Agarose Gel Entrapping Nanoceria and Galactose Oxidase,” *Nanomaterials 2020, Vol. 10, Page 895*, vol. 10, no. 5, p. 895, May 2020, doi: 10.3390/NANO10050895.

[65] P. Zarrintaj *et al.*, “Agarose-based biomaterials for tissue engineering,” *Carbohydr Polym*, vol. 187, pp. 66–84, May 2018, doi: 10.1016/J.CARBPOL.2018.01.060.

[66] A. De Poulpiquet *et al.*, “Dual Enzymatic Detection by Bulk Electrogenerated Chemiluminescence,” *Anal Chem*, vol. 88, no. 12, pp. 6585–6592, Jun. 2016, doi: 10.1021/ACS.ANALCHEM.6B01434.

[67] C. Fang, H. Li, J. Yan, H. Guo, and T. Yifeng, “Progress of the Electrochemiluminescence Biosensing Strategy for Clinical Diagnosis with Luminol as the Sensing Probe,” *ChemElectroChem*, vol. 4, no. 7, pp. 1587–1593, Jul. 2017, doi: 10.1002/CELC.201700465.

[68] J. Meyer, L. E. Meyer, and S. Kara, “Enzyme immobilization in hydrogels: A perfect liaison for efficient and sustainable biocatalysis,” *Eng Life Sci*, vol. 22, no. 3–4, pp. 165–177, Mar. 2022, doi: 10.1002/ELSC.202100087.

[69] G. Danaei *et al.*, “National, regional, and global trends in fasting plasma glucose and diabetes prevalence since 1980: Systematic analysis of health examination surveys and epidemiological studies with 370 country-years and 2·7 million participants,” *The Lancet*, vol. 378, no. 9785, pp. 31–40, Jul. 2011, doi: 10.1016/S0140-6736(11)60679-X.

# *Chapter 4*

*An Origami Lab-on-Paper Biosensor for ATP Detection by Chemiluminescence DNA nanoswich assay*

---

## 4.1 Introduction

Aptamers are nucleic acid sequences capable of specifically recognizing and binding to target molecules, following a three-dimensional configuration change achieved after contact with the analyte. These sequences have been proposed as innovative probes for the development of new generation biosensors [1] due to the various advantages they possess over the more common antibodies. In fact, they are characterized by greater stability and are cheaper [2], [3]. Moreover, they are chemically synthesized, ensuring excellent reproducibility of production, and they are far simpler to engineer and chemically modify than protein affinity reagents. Recently, considering the aforementioned advantages, aptamer-based biosensors have found wide development in the scientific community.

Various approaches have been explored to date to incorporate the structure switching functionality into aptamer molecules. Based on the molecular mechanism that regulates target recognition and the optimal thermodynamic equilibrium between the associated and non-associated states, sensor aptamers are divided into three main categories: aptamer beacons, split aptamer sensors and strand-displacement sensors [4]. Originally, molecular beacons were developed for the detection of specific DNA sequences by fluorescence measurements [5]. These molecular structures are labelled at the 5' and 3' ends with a fluorophore and a quencher respectively and contain within them a specific nucleotide sequence capable of recognizing and hybridising, reaching a configuration that takes the name of hairpin in which the fluorophore and quencher are neighbours, resulting in the absence of a luminescent signal. In the presence of a target, a conformational change occurs which leads to the separation of the two labelled ends, resulting in an increasing of fluorescence. As an example, Ellington and coworkers designed the first aptamer beacon based on an existing thrombin-binding aptamer, based on this kind of recognition mechanism [6], [7]. Molecular beacons have been employed for a variety of applications ranging from biosensing platforms for DNA/RNA detection and the monitoring of enzymatic processes, to the real time analysis of living cells pathways [8]. A molecular system that offers higher specificity and lower background is represented by split aptamers. In this case, the aptamers are split into two nucleic acid strands labelled with a fluorophore and a quencher, respectively, able to combine only in presence of a target. Thus, in the absence of analyte, the nucleotide strands are free in solution, and a luminescent signal occurs. The presence of the target promotes the assembly of the two strands, resulting in a decrease of the fluorescent signal. Well known examples based on split aptamers systems are those developed for the detection of ATP [9], [10] and for the Tat protein [11].

A limitation related to the previously described aptamer engineering strategies consists in the modification of the target binding region within the aptamer. An alternative approach that modifies the aptamer only minimally is the displacement strand structure-switching aptamer (dsSSA) assay, which employs a short quencher-labelled strand hybridized to a fluorescent aptamer. In the absence of target, fluorescence is quenched; upon target binding, the short strand is displaced, restoring signal. Proper tuning of strand stability ensures preferential aptamer-target binding and dose-dependent fluorescence recovery. This concept was first demonstrated with ATP and thrombin aptamers [4], [12].

Nearly three decades after their discovery, Deoxyribozymes (DNAzymes) have been extensively applied in biosensing. As functional oligonucleotides, they can operate as reporters, allowing the transduction of detectable signals [13]. The activity of certain DNAzymes depends on the presence of specific molecules, including metal ions and proteins [14] and because of this property can be used to engineer biosensors capable of detecting such molecules.

A widely investigated class of DNAzymes is represented by G-quadruplex (G4) oligonucleotides complexed with hemin (iron (III)-protoporphyrin IX), which exhibits peroxidase-like activity. In these systems, hemin stacks onto the G-tetrads of the G4 scaffold, stabilizing either parallel or antiparallel conformations, and catalyses the oxidation of various substrates (e.g., ABTS, TMB, luminol) in the presence of hydrogen peroxide [15].

G-quadruplex/hemin (G4/hemin) biosensors offer several advantages: they are simple to design and produce due to the ease of oligonucleotide synthesis and modification; stable, as G4 structures are more resistant to denaturation than proteins; and cost-effective, since both DNA and hemin are inexpensive and readily available. Moreover, their structural tunability allows precise control over catalytic activity and specificity, making them versatile tools for analytical applications [16], [17].

G-quadruplex/hemin DNAzymes, which mimic peroxidase activity, enable signal quantification through either chemiluminescent or colorimetric methods. Chemiluminescent biosensors offer significant advantages over colorimetric systems. The photon-based readout provides a virtually background-free signal, enabling the detection of analytes at much lower concentrations. Chemiluminescent DNAzymes also exhibit a broader dynamic range and reduced interference from sample turbidity or colour, which can limit colorimetric assays [15].

Over millions of years, nature has fine-tuned a complex network of molecular mechanisms to regulate a variety of cellular activities. Cells and organisms can rapidly and precisely respond to changes in their extracellular and intracellular environments. Many of these processes rely on molecular

switches, receptors that transmit information from the cell's exterior to its interior. Structure-switching biomolecules change their conformation or oligomerization state upon target binding, triggering specific outputs such as ion channel opening or enzyme activation [18].

Inspired by these mechanisms, which efficiently convert a specific chemical and/or biological input into a desired output, strong efforts to re-create *in vitro* artificial switches using synthetic molecules or re-engineered biomolecules have been done. These tools can find broad applications ranging from the measurement of biomolecule concentration to the tuning of biomolecular activity (i.e. enzymatic activity). DNA-based switches represent an emerging class of structure-switching receptors whose structure and function are regulated (i.e. activated or inhibited) by the presence of specific molecular and chemical inputs.

The utilization of aptamers and DNAzymes to engineer analyte recognition switches is a compelling strategy in biosensor development. By integrating these components, researchers have developed biosensors that can switch their recognition capabilities in response to environmental stimuli, offering enhanced sensitivity and versatility in detecting a wide range of analytes [19]. This approach holds promise for advancing diagnostic tools and environmental monitoring systems.

As can be seen from the large number of examples of aptamer-biosensors for ATP quantification, ATP represents one of the most used targets for the design of different recognition mechanisms of aptamer-biosensors. Adenosine triphosphate (ATP), being a high-energy compound, is found in all living cells and performs important functions in cell life activities and signal transmission [20], [21]. ATP reflects cellular energy status and is involved in key physiological and pathological processes, including Parkinson's and cardiovascular diseases [22]. Its measurement is crucial in research and diagnosis [23]. Common detection methods include bioluminescence [24], HPLC [25], and capillary electrophoresis [26], though these often require costly equipment and complex pretreatment [27].

During the past two decades, ATP has been used as a target by many groups to test new aptamer selection methods [28]. A very popular method is to immobilize nucleic acid libraries and use free target molecules for selections [29]. For example, Nutiu and Li used the library immobilization method, but obtained the exact same classical DNA aptamer [30]. The other reported ATP aptamers have been much less studied or used probably due to their lower affinities, longer sequences, less defined structures, or modified nucleotide content [31], [32].

Still recently aptamer-biosensors for the detection of ATP are being developed, employing recognition mechanisms of greater complexity, and based on detection techniques alternative to

fluorescence, such as electrochemistry, colorimetry or chemiluminescence, to increase the specificity of recognition towards the target and the sensitivity of the methods analysed.

Del Grosso et al. developed a modular DNA nanoswitch combining a clamp probe and an aptamer, enabling target-dependent activation and tunable affinity using an external ligand [33]. Biochemical amplification techniques (e.g., PCR, rolling circle amplification) and CRISPR-based systems have further enhanced assay sensitivity. Pan et al. used a hollow covalent organic framework (COF) to protect a CRISPR/Cas12a-aptamer nanosensor for in vivo ATP imaging, allowing robust detection in live animals [34]. Liu et al. designed a 2D DNA structure with multiple ATP aptamers acting as toehold switches; ATP binding collapses the structure, releasing methylene blue and generating a rapid, sensitive electrochemical signal, achieving a detection limit of 0.3 pmol $L^{-1}$ in 30 minutes [35].

We previously developed a structure-switching aptasensor exploiting ATP-induced hemin-DNAzyme catalytic activity for generating a chemiluminescent signal implemented on a lab-on-chip, hosting the a-Si:H photodiodes and the microfluidic network [36]. In this system, the G-quadruplex DNA-nanoswitches can recognize different ATP concentrations and turn into catalytically active DNAzymes that generate chemiluminescence in the presence of $H_2O_2$/luminol. Specifically, aptamer-nanoswitch can be used as a potential biosensor to detect the life marker ATP through DNAzyme-like catalytic activity, in view of its future possible application in extraterrestrial exploration missions.

In last decades, the interest in paper-based biosensors has grown, thanks to the possibility of integrating the benefits related to the using instead of antibodies with the much more promising aptamers, and the well-known and widely established advantages of paper-based microfluidic devices. Once appeared, the paper-based microfluidic chip attracted considerable interest from most scientific researchers. It has attractive advantages such as robustness, portable transportation, low consumption of reagents and no need for an external pump, etc. It has been applied in various fields such as colorimetry, fluorescence, surface Raman scattering, and electrochemical sensing [37].

Aptamer sensors combined with paper-based microfluidic devices are becoming increasingly popular as a new trend in the field of in situ sensing. Portable paper-based sensors enable rapid, on-site detection of chemicals and metals using simple readouts [38], [39].

Therefore, research oriented towards the development of cheap and green portable devices based on the robustness and increasing specificity of the aptamer target recognition mechanism continue to represent a captivating challenge in the field of biosensing. Aptamer sensors combined with paper-based devices have become a new research route, well suited to the purpose of *in situ* sensing.

However, the majority of studies reported in the literature implement the complete assay in solution [40], [41]. In certain instances, paper substrates are employed exclusively for the terminal signal acquisition step, while the bulk of the assay remains solution-based [42], [43]. Although this strategy confers enhanced analytical sensitivity, it constrains the development of biosensors designed for in situ or point-of-need applications.

In this research work, a ready-to-use lab-on-paper aptamer-based biosensor, inspired by the same biorecognition mechanism previously investigated, is presented for on-site ATP detection in water for microbial monitoring. This biosensor is based on allosterically regulated DNA-based switches strategy, exploiting the advantages of chemiluminescence as detection methods and smartphone imaging. The chip was prepared with hydrophilic and hydrophobic regions through wax printing. The single-strand DNA composed by an ATP specific recognition sequence and a turn-on G-quadruplex sequence upon the ATP-bonding was fixed on the reaction area of the paper chip. After adding the ATP sample, aptamer changes its 3D-conformation *turning-on* the G-quadruplex sequence folding. This latter combining with hemin exploits a DNAzyme activity that catalyses the chemiluminescence reaction between luminol and $H_2O_2$ [36]. Due to the capillary force-driven liquid action in the hydrophilic channel of the filter paper, the luminol and perborate flowed into the detection area, where the chemiluminescence signal was raised. The changes of the chemiluminescence signal were captured by a CCD and BI-CMOS mobile camera. Therefore, the proposed device indicated the advantages of portable, low cost, and less consumption.

To overcome the limitations of direct aptamer immobilization on paper substrates, a bio-polymeric matrix as an intermediate support was employed. The matrix provides a uniform and versatile environment, reducing non-specific adsorption and preserving the aptamer's structural flexibility, essential for high-affinity binding. This strategy improves the stability, reproducibility, and overall performance of the paper-based biosensor by combining the advantages of cellulose with a tailored microenvironment for the aptamers [43], [44], [45].

## 4.2 Materials and methods

### 4.2.1 Reagents and materials

Adenosine 5′-triphosphate (ATP) disodium salt hydrate (99%), adenosine 5′-monophosphate monopotassium salt dihydrate (95%), hemin from bovine (≥ 90%), trizma hydrochloride, sodium bicarbonate (99%), sodium carbonate (anhydrous) (≥ 99%), hydrogen peroxide (30%), sodium perborate tetrahydrate, pullulan, agarose, ethylenediaminetetraacetic acid (98.5% powder), and

luminol sodium salt were purchased from Sigma-Aldrich (St Louis, MO, USA). dNTP Mix (10 mmol $L^{-1}$ each) was obtained from Thermo-Fisher Scientific (Fair Lawn, NJ, USA).

DNA sequence purified via high-performance liquid chromatography (HPLC) was purchased from Integrated DNA Technologies (IDT, Skokie, IL). All reagent-grade chemicals were used without further purification. All the other chemicals were of the highest purity available. The Whatman CHR 1 chromatographic paper (200 × 200 mm sheets) was bought from Sigma-Aldrich.

The following buffers were used in the assay procedure: TRIS (TRIS 100 mmol $L^{-1}$ pH 7.4, containing $MgCl_2$ 10 mmol $L^{-1}$), carbonate-bicarbonate buffer 0.1 mol $L^{-1}$ (sodium bicarbonate 230 mmol $L^{-1}$, sodium carbonate (anhydrous) 760 mmol $L^{-1}$, pH 10.4), and TE buffer (TRIS 10 mmol $L^{-1}$, EDTA 1.0 mmol $L^{-1}$, pH 8.0).

As real samples, different commercial drinking waters spiked with known ATP amounts were used.

### 4.2.2 Reference optical instrumentation

Chemiluminescence measurements were carried out using an ultrasensitive CCD camera (ATIK Camera 383L Plus) equipped with Kodak's KAF-8300 Image Sensor coupled with an objective and inserted into a light-tight dark box to avoid interference from ambient light. As proof of principle, CL emission was also detected with a Samsung S20 smartphone's CMOS camera (Samsung, Seoul, South Korea) using the proprietary camera app.

### 4.2.3 DNA nanoswitch

A structure-switching aptasensor exploiting ATP-induced hemin-DNAzyme catalytic activity (Adornetto et al., 2015) for generating a chemiluminescent signal was developed for its implementation on the *lab-on-paper origami* chip. The assay principle, shown in Figure 4.1, is based on a stem-loop DNA nanoswitch that can adopt two exclusive conformations: "non-binding conformation" containing a stem domain and a "binding-competent" conformation containing a duplex stem (red stem) recognized by the specific target analyte ATP. The binding of ATP pushes the conformational equilibrium towards the latter "bound" state to allow the hemin/G-quadruplex structuring. The incorporation of hemin into the resulting G-quadruplex ATP-nanoswitch aptamer complex yields an active HRP-mimicking DNAzyme, which generates a chemiluminescence signal in the presence of $H_2O_2$/luminol proportional to ATP concentration.

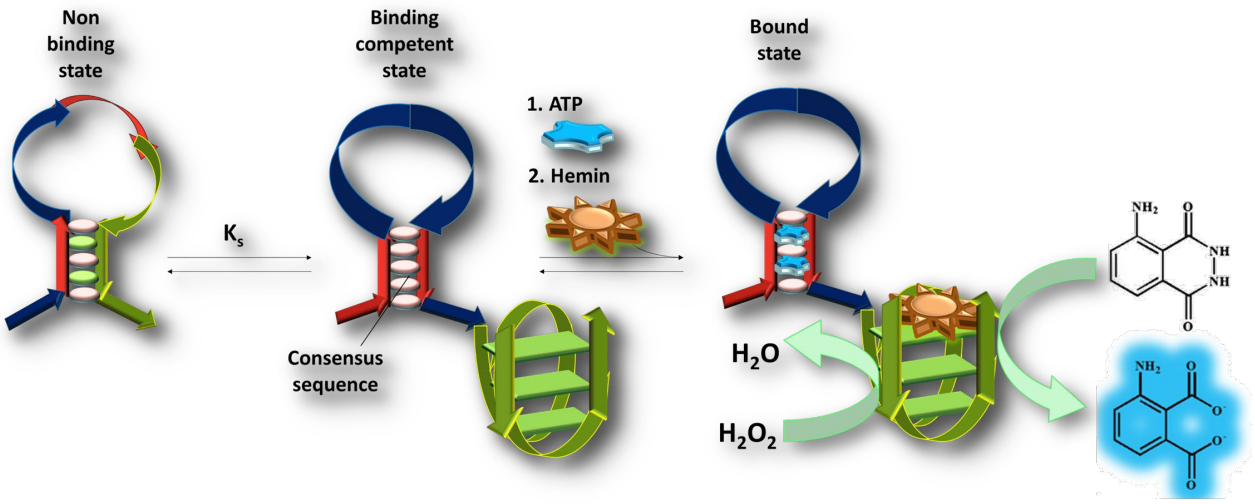


***Figure 4.1.*** *The molecular structure of the assay includes ATP-regulated DNA nanoswitches, which can exist in two opposing stem-loop forms: "Non-Binding" and "Binding-competent". ATP binds to the nanoswitches pushing the conformational equilibrium towards the "Bound" state, which induces the formation of a hemin/G-quadruplex structure.*

The oligonucleotides were used as provided and diluted in pH 8.0, TE buffer solution to give stock solutions of 100 µmol $L^{-1}$. The sequence (DNA-nanoswitch) regulated by ATP is as follows:

5′-*ACCTGGGGGAGTAT*CAACCC*TGCGGAGGAAGGT*TTTGGGTGGGTTGGGTGGGT-3’

In the sequence above the underlined bases represent the stem portion of the “non-binding” state, while the italic bases represent the ATP recognition element and the stem of the “bound” state.

For performing the assay, DNA-nanoswitch was entrapped in a 10% w/v pullulan matrix and then adsorbed on a chromatographic paper chip.

### 4.2.4 Fabrication of the *lab-on-paper Origami* µPAD Device

The *origami* µPAD was produced by drawing the layout of the hydrophobic areas on PowerPoint and printing the areas on a 200 × 200 mm Whatman CHR 1 chromatography paper sheet using a commercial solid ink Phaser 8560DN printer (Xerox Co., Norwalk, CN, USA). The folding lines were created by a manual rotary perforating blade and the µPAD was cut from the paper sheet and heated at 150 °C for 2 min in an oven to melt the wax-based solid ink, which diffused into the paper, generating the hydrophobic barriers. As illustrated in Figure 4.2, the *origami* is composed of three paper layers/sheets having the same dimensions (25 mm x 20 mm). However, layers A and B are

characterized by six hydrophilic areas (5 mm diameter), whereas layer C shows only a hydrophilic area surrounded by a hydrophobic frame and back. In the case of layer C, printing is carried out on both sides (front and back) in order to create the white hydrophilic region surrounded exclusively by the hydrophobic frame on one side, while the opposite side is fully coated with hydrophobic wax. Afterwards, the reagents were loaded into the origami µPAD by dispensing the solutions onto the hydrophilic areas. First, 5.0 µL of DNA nanoswitch solution 1.0 µmol $L^{-1}$ in pullulan 10% w/v prepared in TRIS buffer (TRIS 100 mmol $L^{-1}$, pH 7.4, containing $MgCl_2$ 10 mmol $L^{-1}$) were added in each area of layer A and left to dry. For layer B, in each area 10 µL of 60 mmol $L^{-1}$ sodium perborate solution in carbonate-bicarbonate buffer 0.1 mol $L^{-1}$ pH 10.8 were dispensed. Finally, on layer C 100 µL of 5.0 mmol $L^{-1}$ the luminol were adsorbed on the whole hydrophilic area. After air-drying at room temperature in the dark for 1 h, the biosensor was stored at 4°C in the dark until use.

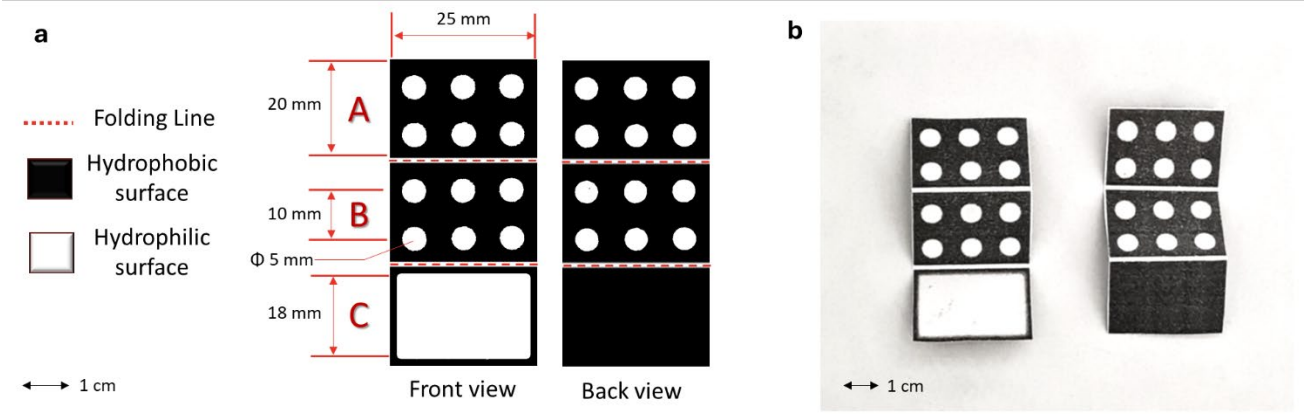


***Figure 4.2.*** *Aptasensing µPAD. (a) Layout of the µPAD with hydrophobic areas printed in black. (b) Photo of the µPAD, after heating by front (left) and back (right) view, preloading of reagents and folding.*

### 4.2.5 Assay Procedure in solution

For the quantification of ATP, a solution test was first developed, in which only the detection step is performed on paper. For each ATP concentration tested (10 – 50 – 100 – 200 – 500 – 1000 µmol $L^{-1}$), a reaction mix with a final volume of 25 µL in TRIS buffer (100 TRIS mmol $L^{-1}$, pH 7.4, containing $MgCl_2$ 10 mmol $L^{-1}$) was prepared, containing DNA nanoswitch 1.0 µmol $L^{-1}$, hemin 5.0 µmol $L^{-1}$ and the different ATP concentrations. Firstly, DNA nanoswitch (4.0 µmol $L^{-1}$ diluted in TRIS buffer) was heated for 5 minutes at 95°C to limit any unwanted secondary conformations. Then, 6.0 µL of the DNA nanoswitch solution and 12 µL of different ATP concentrations solutions were added to 5.0 µL of TRIS buffer. Upon 30 min of incubation at room temperature (RT), 2.0 µL of hemin 100 µmol

$L^{-1}$ were added to each mix and left reacting for 20 min. Later, to perform the analysis, 5.0 µL of each reaction tube were dispensed on the *lab-on-paper* device. To detect the signal, 5.0 µL of a chemiluminescence (CL) detection mix (luminol 1.0 mmol $L^{-1}$ and $H_2O_2$ 60 mmol $L^{-1}$ in carbonate-bicarbonate buffer 0.1 mol $L^{-1}$ pH 10.4) were spotted on the device's hydrophilic regions and the CL signal was acquired by a CCD camera.

### 4.2.6 Assay Procedure for the *Origami* format biosensor

To exploit the advantages of *origami* paper biosensors, all the reagents necessary for the analysis where previously loaded on the device's sheets. In order to immobilize DNA aptamers and DNAzymes on paper supports, their trapping within bio-polymer matrices is necessary. This allows the target recognition and the correct folding, even when adsorbed on paper. In this work, the DNA nanoswitch was trapped within a 10% w/v pullulan matrix in layer A, prepared in TRIS buffer (TRIS 100 mmol $L^{-1}$, pH 7.4, containing $MgCl_2$ 10 mmol $L^{-1}$). In addition, the reagents required for the chemiluminescent reaction were also immobilised: luminol was loaded on layer C five times more concentrated (5.0 mmol $L^{-1}$) than the concentration of the CL revelation mix employed for the solution test (1.0 mmol $L^{-1}$); due to the poor stability of hydrogen peroxide, sodium perborate was immobilised on the chromatography paper layer B as oxidising agent.

Hence, 5.0 µL of a solution of DNA nanoswitch (previously heated at 95°C for 5 min) 1.0 µmol $L^{-1}$ prepared in pullulan 10% w/v solubilized in TRIS Buffer (TRIS 100 mmol $L^{-1}$, pH 7.4, containing $MgCl_2$ 10 mmol $L^{-1}$) was loaded on the six hydrophilic regions of layer A and left drying at room temperature for at least 1 h. Then, 5.0 µL of different ATP concentrations solutions (1.0 – 10 – 50 – 100 – 500 µmol $L^{-1}$) were spotted on the adsorbed DNA nanoswitch and left reacting for 30 min. Afterwards, 2.5 µL of hemin 5.0 µmol $L^{-1}$ solution were added. Upon 20 min of incubation at RT, layer C was rinsed with 100 µL of carbonate-bicarbonate buffer 0.1 mol $L^{-1}$ pH 10.4 and the origami was correctly fold following the scheme in Figure 4.3. Immediately after the folding, the CL signals were acquired by the CCD camera.

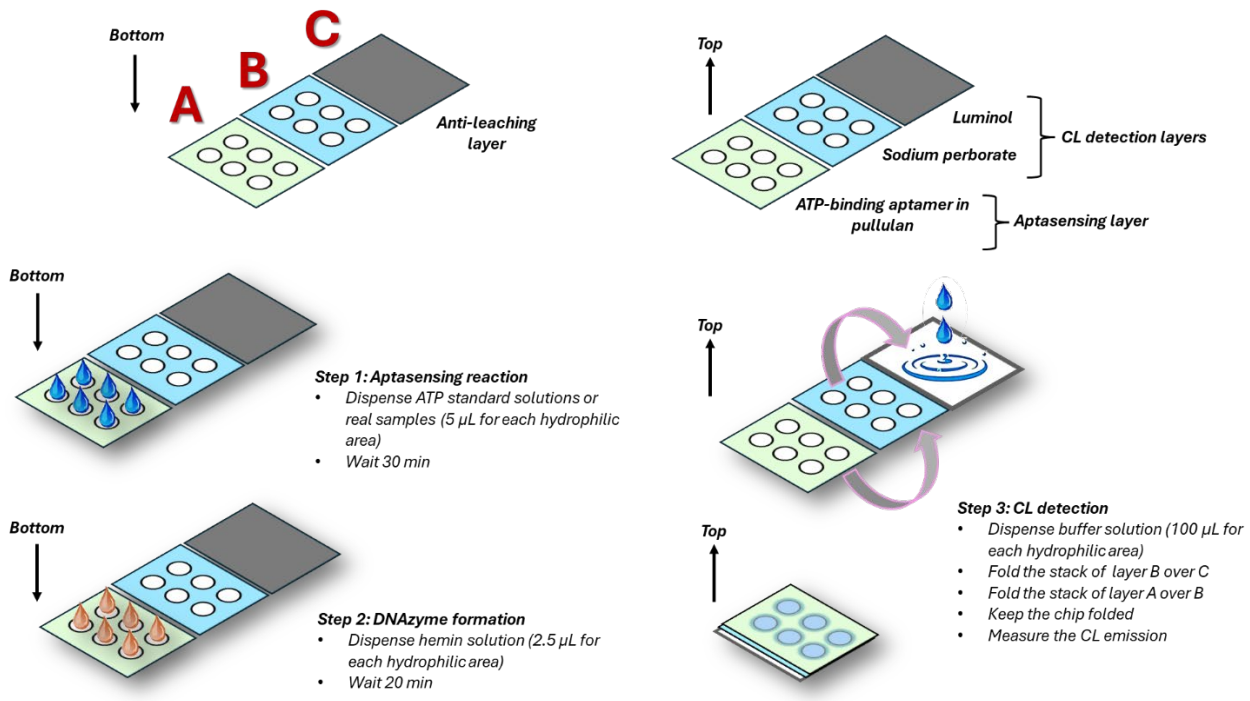


***Figure 4.3.*** *Scheme of the analytical procedure for the determination of ATP using the origami µPAD.*

### 4.2.7 CL imaging

The chemiluminescent signals were monitored employing a portable, cooled charge coupled device (CCD) camera (ATIK Camera 383L Plus, ATIK Cameras, New Road, Norwich) adapted to perform imaging detection, as previously described. A sequence of 4 consecutive images with exposure time of 30 s and Binning 4x4 was acquired, starting immediately after the addition of the buffer. For each sequence, only the last image acquired was analysed in order to allow the homogeneous mixing of the absorbed reagents on the different chromatographic paper layers, due to the vertical flow of the buffer. The CL images were analysed using the freeware ImageJ v.1.53h software (National Institutes of Health, Bethesda, MD). Regions of interest (ROIs) corresponding to the three deposition areas of layer A were defined and for each image, the CL emission intensities were evaluated by integrating the CL emissions on the ROI areas.

### 4.2.8 Data Elaboration and Statistics

All measurements were performed at least in three replicates. All data analysis and statistical data elaboration were performed using GraphPad Prism, version 8.0 (GraphPad Software, Inc., La Jolla, CA, USA). The program was also used to obtain calibration curves by fitting experimental data with both a three-parameter logistic equation (sigmoidal curve) and a ln-log function (linear curve).

### 4.2.9 Real Sample analysis

The method applicability for the analysis of real samples was assessed by using commercial drinking waters from different market brands bought in local stores. No sample treatment was necessary. The direct analysis of real samples was evaluated analysing no diluted samples spiked with different amounts of ATP (1.0 – 10 – 100 μmol $L^{-1}$). Hence, 5.0 μL of three different ATP concentrations solutions spiked in commercial drinking water were spotted on the previously adsorbed DNA nanoswitch and left reacting for 30 min. Then, 2.5 μL of 5.0 μmol $L^{-1}$ hemin solution were added. Upon 20 min of incubation at RT, layer C was rinsed with 100 μL of carbonate-bicarbonate buffer 0.1 mol $L^{-1}$ pH 10.4 and the origami was correctly fold. Immediately after the folding, the CL signals were acquired by the CCD camera.

### 4.2.10 Computational modelling of aptamer-based selectivity

The modelling of complex aptamer-nucleotide was carried out by molecular docking technique. For simplicity, we decided to study only the aptamer sequence involved in the binding with the ATP molecule, due to the existence of the crystallographic structure of interest (1AW4.pdb) deposited in the Protein Data Bank (https://doi.org/10.2210/pdb1AW4/pdb). The structure was refined, and ligands were removed by Autodock Vina software [46]. Target structures (AMP, ATP, GTP, CTP, TTP) were downloaded by PubChem (https://pubchem.ncbi.nlm.nih.gov/), that is an open chemistry database at the National Institutes of Health (NIH). The molecular docking simulations were performed by HNADOCK Server, a nucleic acid (NA) docking server for RNA/DNA – RNA/DNA complex structure modelling [47]. The intermolecular energy expressed in kcal/mol for the best posed models of each aptamer-ligand complex, obtained upon docking, were computed using Abalone software.

## 4.3 Results and discussion

### 4.3.1 Optimization of experimental conditions and construction of calibration curve for the assay in solution

To achieve the best assay performances in terms of sensitivity, the correct hemin concentration was determined, in relation to the constant DNA nanoswitch concentration 1.0 μmol $L^{-1}$. The experiment was performed in solution as described in section 4.2.5 and three different samples for each hemin concentrations were tested: hemin (0.25 – 0.5 – 1.0 – 2.5 – 5.0 μmol $L^{-1}$), DNA nanoswitch with hemin and DNA nanoswitch whit hemin and ATP 500 μmol $L^{-1}$. As expected, the CL signal increases as the concentration of hemin increases. Based on this results, 5.0 μmol $L^{-1}$ was selected as final concentration for the preparation of the bioassay because it shows the best signal/background ratio both compared to hemin and the DNA nanoswitch with hemin (1:5 ratio) (Figure 4.4a).

Moreover, the incubation time of the DNA nanoswitch with ATP was characterised. The experiment was conducted in solution as described in section 4.2.5 and three different samples for each incubation time were tested: DNA nanoswitch (1.0 μmol $L^{-1}$) with hemin, DNA nanoswitch (1.0 μmol $L^{-1}$) with hemin and ATP 200 μmol $L^{-1}$ and DNA nanoswitch (1.0 μmol $L^{-1}$) with hemin and ATP 500 μmol $L^{-1}$. As it can be seen in Figure 4.4b, 30 minutes was proved to be the best reaction time to perform the test.

Finally, the incubation time of the DNA nanoswitch with hemin in the presence of a minimal concentration of ATP (100 nmol $L^{-1}$, to ensure the proper development of the analytical test) was optimised. The experiment was performed in solution as described in section 4.2.5 and two different samples for each incubation time were tested: hemin (5.0 μmol $L^{-1}$) and DNA nanoswitch (1.0 μmol $L^{-1}$) with hemin. As shown in Figure 4.4c, the best signal-to-noise ratio is observed with a reaction time of 20 minutes, although it is still quite high even after 2 hours of incubation.

Once optimized all the experimental parameters of the complex formation, a general analytical method was developed exploiting the answer of the supramolecular system as the concentration of ATP varies, using a lab-on-paper approach. Figure 4.4d shows the calibration curve generated in the optimised experimental conditions in solution, obtained by plotting the CL signals measured for different ATP standard solutions against the logarithm of ATP concentration. Since the number of samples that can be analysed in the lab-on-paper device is limited, the calibration curve has been obtained by combining the results of several biosensors. A three-parameter logistic equation was used to fit the experimental data and obtain the calibration curve parameters. According to the equation of the calibration curve, the limit of detection (LOD) of the assay (calculated as the concentration of

ATP corresponding to the CL signal of the ATP-free sample, plus three times its standard deviation) was 30 µmol $L^{-1}$, while the assay working range was from 10 to 1000 µmol $L^{-1}$ of ATP.

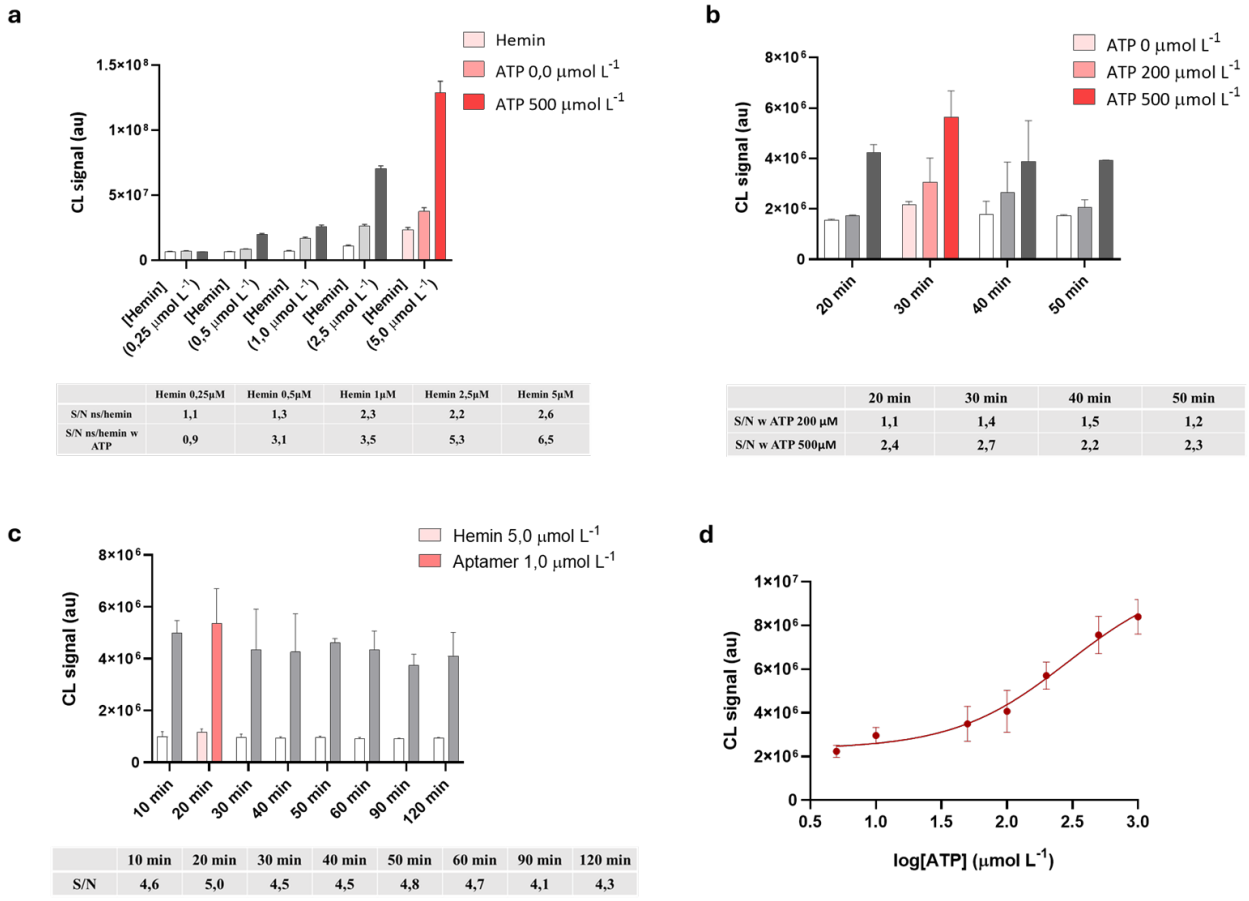


| | Hemin 0,25µM | Hemin 0,5µM | Hemin 1µM | Hemin 2,5µM | Hemin 5µM |
|---|---|---|---|---|---|
| S/N ns/hemin | 1,1 | 1,3 | 2,3 | 2,2 | 2,6 |
| S/N ns/hemin w ATP | 0,9 | 3,1 | 3,5 | 5,3 | 6,5 |

| | 20 min | 30 min | 40 min | 50 min |
|---|---|---|---|---|
| S/N w ATP 200 µM | 1,1 | 1,4 | 1,5 | 1,2 |
| S/N w ATP 500µM | 2,4 | 2,7 | 2,2 | 2,3 |

| | 10 min | 20 min | 30 min | 40 min | 50 min | 60 min | 90 min | 120 min |
|---|---|---|---|---|---|---|---|---|
| S/N | 4,6 | 5,0 | 4,5 | 4,5 | 4,8 | 4,7 | 4,1 | 4,3 |

***Figure 4.4.*** *Determination of optimal experimental conditions. (a) Determination of the optimal concentration of hemin at a constant DNA concentration (1 µmol $L^{-1}$) with the corresponding signal-to-noise (S/N) ratios shown below. (b) Optimization of incubation time of the DNA nanoswitch with ATP, keeping constant the concentration of hemin, with the corresponding signal-to-noise ratios shown below. (c) Optimization of the incubation time of the DNA nanoswitch with hemin in the presence of a minimal concentration of ATP (100 nmol $L^{-1}$) monitoring the best CL signal-to-noise ratio, with the corresponding signal-to-noise ratios shown below. (d) Calibration curve generated by combining the results obtained by analysing ATP standard solutions. A three-parameter logistic equation was used to fit the experimental data and the equation of the resulting calibration curve was $Y = (2.3\times10^6) + (8.0\times10^6)/(1+10^{(2.467-X)})$ ($R^2 = 0.9899$), where Y and X were the CL signal ratio and the logarithm of concentration of ATP standard solutions. Each of the data are the mean ± SD of three measurements.*

### 4.3.2 Optimization of the Origami µPAD

Once the method had been validated in solution, we proceeded to the origami format on paper. All the reagents necessary to the assay has been adsorbed as DNA nanoswitch, luminol and sodium

perborate for the CL detection reaction. To preserve the three-dimensional structure of DNA nanoswitch, while maintaining target recognition and catalytic activity, it is necessary to entrap the sequence within bio-polymeric matrices. The sugary nature of such compounds [48], [49], ensures an optimal hydration and environmental preservation on the paper substrate. As shown in Figure 4.5, pullulan 10% w/v and agarose 0.1% w/v were tested as possible candidate matrices for this purpose. The best results were obtained with pullulan 10% w/v because it shows the best signal-to-noise ratio.

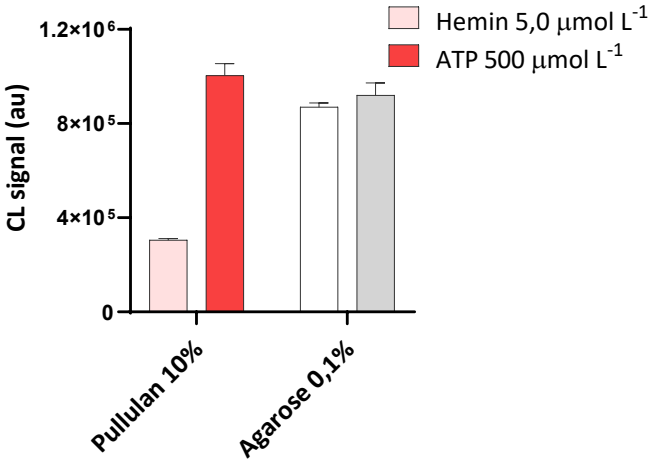


***Figure 4.5.*** *Evaluation of the best entrapment conditions for aptasensor between pullulan 10% and agarose 0.1% w/v that provide highest CL signal-to-noise ratio.*

### 4.3.3 Assay Performance

Once optimised the paper-based experimental conditions, the analytical method for the µPAD aptassay was developed. Figure 4.6a represents the calibration curve generated in the optimised experimental conditions, obtained by plotting the CL signals measured for different ATP standards against the logarithm of ATP concentration. Also in this case, the calibration curve has been obtained by the combination of several biosensors. A three-parameter logistic equation was used to fit the experimental data and obtain the calibration curve parameters. According to the equation of the calibration curve, the LOD of the assay (calculated as the concentration of ATP corresponding to the CL signal of the ATP-free sample, plus three times its standard deviation) was 3 µmol $L^{-1}$, while the assay working range was from 1 to 500 µmol $L^{-1}$ of ATP. This limit of detection is consistent with the dissociation constant (6 ± 3 µmol $L^{-1}$) reported for the ATP binding 27-mer aptamer employed in this work [9]. In addition, it is worth noting that all reported DNA aptamers have Kd values greater than 6 µmol $L^{-1}$ for adenosine and ATP [50].

Since the number of samples that can be analysed in a single *lab-on-paper* µPAD is limited, an analytical procedure that relies on a multiple-point calibration curve could be only performed using several devices, which would complicate assay execution. For this reason, we assessed the reliability of a calibration curve obtained using only three ATP standard solutions (1 – 10 – 100 µmol $L^{-1}$). As shown in Figure 4.6b, the comparison between the two calibration curves shows a good agreement in term of the slopes, allowing us to use a single chip for a reliable analysis.

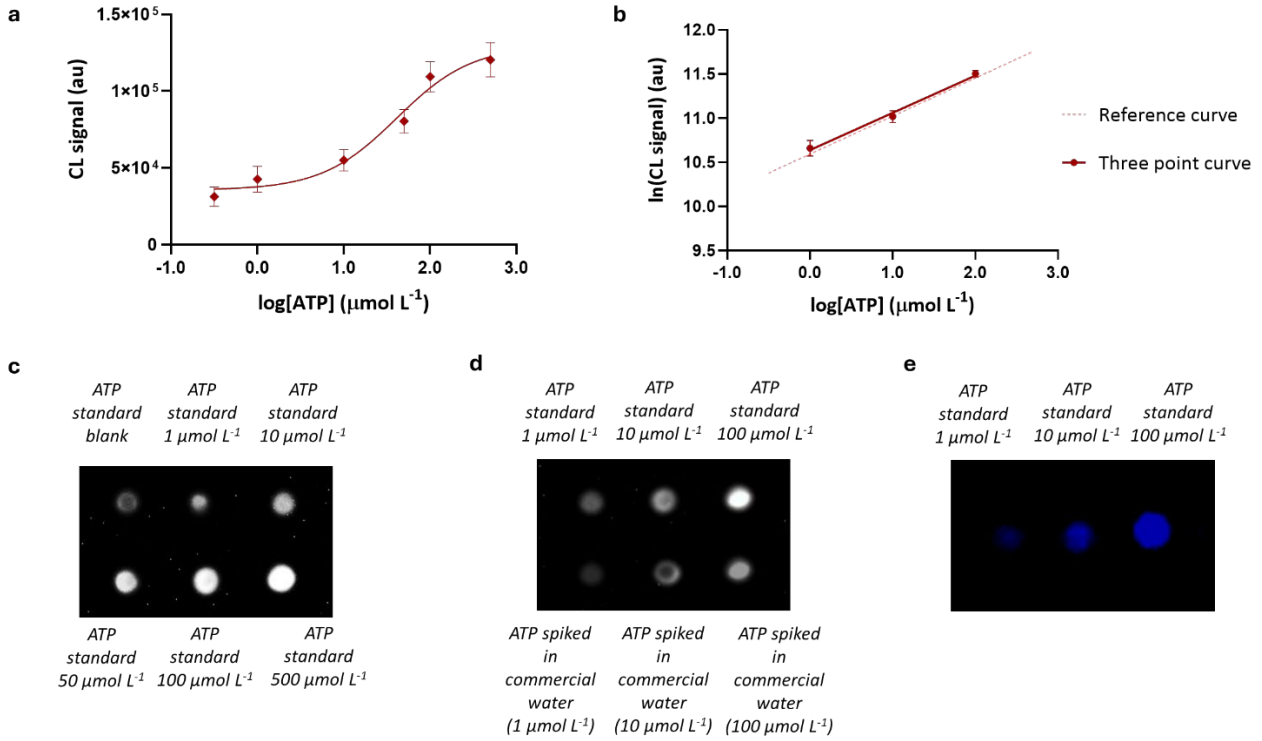


***Figure 4.6.*** *Analytical method: (a) calibration curve generated by combining the results obtained by analysing ATP standard solutions with different µPAD biosensors. A three-parameter logistic equation was used to fit the experimental data and the equation of the resulting calibration curve was* $Y = (3.6\times10^{4}) + (9.4\times10^{4})/(1+10^{(1.616-X)})$ *(*$R^2 = 0.9770$*), where Y and X were the CL signal ratio and the logarithm of concentration of ATP standard solutions. Each of the data are the mean ± SD of three measurements. (b) Comparison of slope between reference and three-point calibration curve plotted as Ln (CL signal) (au) vs Log [ATP] (µmol* $L^{-1}$*) for origami format. (c) Imaging of CL signal corresponding to reference calibration curve acquired by CCD camera. (d) Imaging of CL signal corresponding to three-point calibration curve (upper line) and to three different concentrations of ATP spiked in a sample of commercial drinking water acquired by CCD camera. (e) Imaging of CL signal corresponding to three-point calibration curve acquired by mobile BI-CMOS camera of smartphone Samsung S20 (Samsung, Seoul, South Korea).*

### 4.3.4 Accuracy and Quantification of ATP in Real Samples

The accuracy of the origami μPAD biosensor for ATP was evaluated by comparison of measurements obtained for real samples. To assess its applicability for microbial monitoring in water, commercial drinking water from different market brands bought in local stores was analysed. We investigated the potential interference of a real sample matrix by performing a recovery study. A commercial water sample with ATP content below the LOD of the assay was spiked with known amounts of ATP and analysed using the origami μPAD. Table 4.1 shows a good value of percentage recovery, thus implying a negligible decrease in sensitivity and the applicability of the biosensor in real complex matrices.

***Table 4.1.*** *Results of the recovery study of the origami μPAD biosensor performed on a commercial drinking water sample spiked with known amounts of ATP.*

| | **Concentration of ATP Spiked (μmol $L^{-1}$)** | **Concentration of ATP Measured (μmol $L^{-1}$)** | **Recovery (%)** |
|---|---|---|---|
| Sample 1 | 1 | 0.99 ± 0.04 | 99 ± 4 |
| Sample 2 | 10 | 10.1 ± 0.7 | 101 ± 7 |
| Sample 3 | 100 | 112 ± 14 | 112±14 |

Moreover, to increase the further portability of paper-based device, the possibility to detect the CL signal of the developed aptasensor by smartphone BI-CMOS camera was demonstrated. Since the sensitivity of mobile camera is slightly lower than that of a CCD camera [51], it was necessary to slightly adapt the quantities of adsorbed CL mix (luminol 10 mmol $L^{-1}$, sodium perborate 150 mmol $L^{-1}$). In this way it was possible to increase the intensity of the emitted signal, without modifying the analytic protocol of aptasensing for ATP. As shown in Figure 4.6e, using a Samsung S20 smartphone's CMOS camera (Samsung, Seoul, South Korea) with the proprietary camera app, we can discriminate three different ATP levels in good agreement with previously data.

### 4.3.5 Assay specificity

To evaluate assay specificity, standard solutions of AMP (adenosine 5′-monophosphate) and a mix solution of ATP, GTP, CTP and TTP were analysed with origami µPADs. Figure 4.7 shows the comparison between the CL signals measured for 50 µmol $L^{-1}$ standard solutions of the potentially interfering molecules and an equimolar ATP standard solution. The results showed that, even at such relatively high concentrations, AMP, GTP, CTP, and TTP did not significantly interfere with the binding of ATP to DNA nanoswitch.

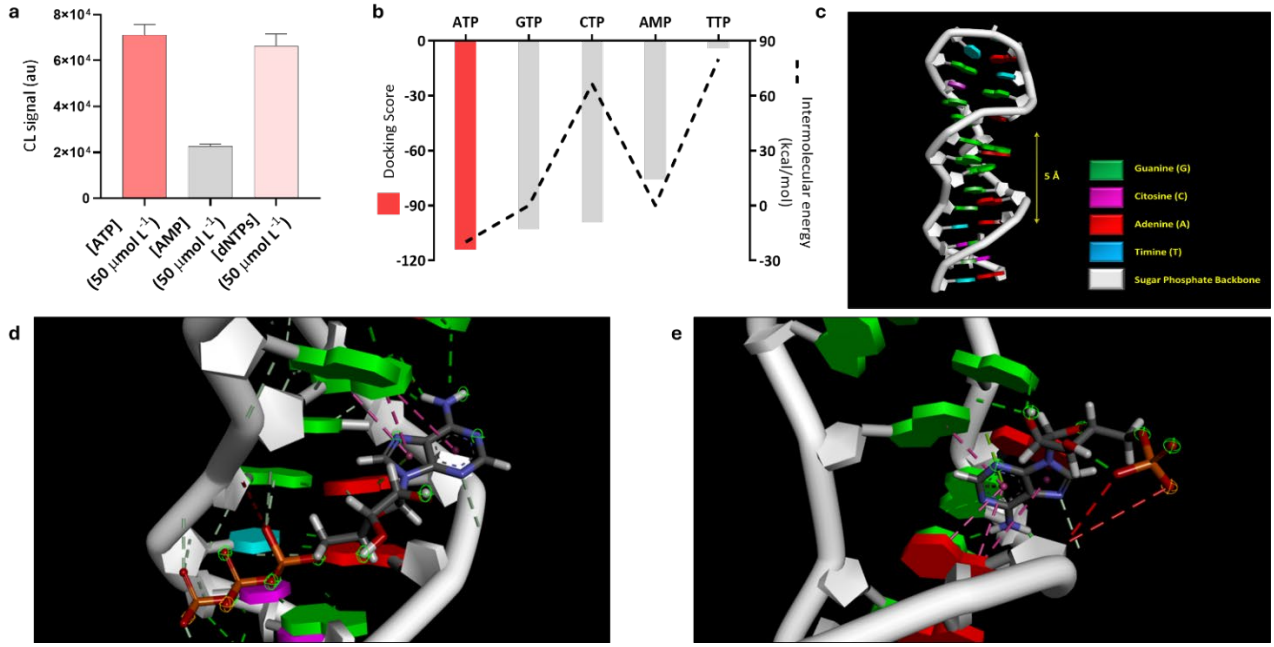


***Figure 4.7.*** *Assay specificity. (a) CL signals measured in the origami µPAD for 50 µmol $L^{-1}$ standard solutions of the potentially interfering nucleotides AMP, dNTPs (containing ATP, GTP, CTP, TTP). For comparison, the CL signal measured for a 50 µmol $L^{-1}$ ATP standard solution is reported. Each of the data are the mean ± SD of three measurements. (b) results of molecular docking study: comparison between docking score values and intermolecular energy (kcal/mol) for each nucleotide docked within aptamer. (c) crystallographic structure of aptamer specific for ATP. (d) Most probable 3D structures obtained by molecular docking simulations for the complexes of ATP with aptamer. (e) Most probable 3D structures obtained by molecular docking simulations for the complexes of AMP with aptamer.*

For a better comprehension of assay specificity, an *in-silico* model was used to compare the experimental results with computational data. In detail, the model was used to calculate the thermodynamic stability parameters of the aptamer-target complexes formed between the aptamer and either ATP or the tested interfering nucleotides.

Computational modelling methods for the *in-silico* construction of the 3D structure of aptamers and their complexes with biomolecules as proteins or polynucleotides have been already developed and applied in drug discovery [47], while their exploitation to support aptasensor development is not yet widespread. Even if the obtained docking scores here do not reflect the true binding affinities, but a relative ranking of the complex models, as algorithm score used in the server was not calibrated with experimental binding data [52], they provide us an estimate of strengths of complex receptor-ligand association interactions. These data were compared to the energies of the intermolecular interactions between aptamer and target calculated using abalone software, a tool dedicated to biomodelling of macromolecules.

The theoretical data obtained through the molecular modelling study are in good agreement with the experimental data. They confirm that the designed aptamer can preferentially recognize ATP. Furthermore, the structural analysis of the complex allows us to understand the greater affinity of the aptamer towards ATP compared to AMP. As can be seen from Figures 4.7d and 4.7e, the presence of the two phosphate groups in the beta and gamma atoms of phosphorous of ATP allow to better stabilize the target in the active site of the DNA, which is a sequence rich in guanine, in good agreement with the literature [53].

### 4.3.6 Stability

The stability of the reagents (aptamer entrapped in pullulan, luminol and sodium perborate) over time, loaded in the origami μPAD has been investigated. A series of origami μPADs was sealed stored at 4 °C. After a given storage time (up to 10 days), the CL signals obtained for the analysis of an ATP standard (100 μmol $L^{-1}$) were measured. The comparison of the CL signals with that obtained in a freshly prepared μPAD allowed us to assess the degradation over time of the investigated reagent. As shown in Figure 4.8, displayed good stability, with a CL signal decrease of less than 10% after 10 days of storage. This data provided us the good stability evaluation of adsorbed DNA aptamer entrapped in pullulan, a polysaccharide that ensures high biomolecules stability upon drying [54], as we yet demonstrated in previously papers [55], the long-time stability of luminol and sodium perborate adsorbed on paper-based μPADs (at least up to 6 weeks).

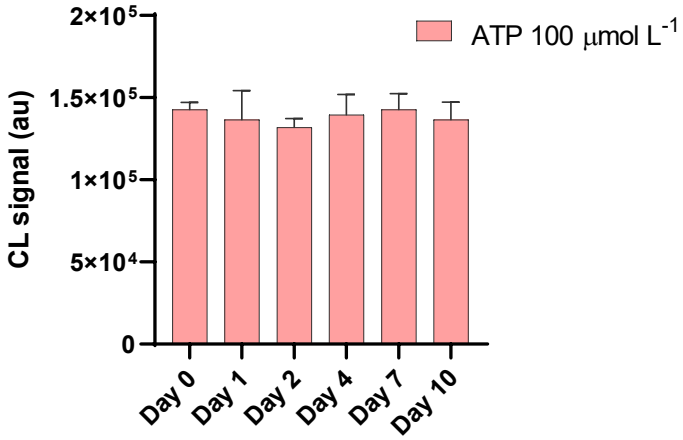


***Figure 4.8*** *Monitoring of stability over time of paper-based device stored at +4°C in the dark by CL signal detection, testing a solution of ATP standard at concentration of 100 μmol $L^{-1}$.*

## 4.4 Conclusions

This article describes an origami μPAD for the quantitative determination of ATP in water samples that displayed improved performance and were suitable for on-site application. The assay relied on a direct recognition of ATP by DNA nanoswitch aptasensing, followed by CL detection by a luminol/hydrogen peroxide system. The use of pullulan allowed easy and efficient immobilization of aptamer in the μPAD. Due to the origami approach, it was possible to fully implement on paper a multi-step analytical procedure and to avoid chemical handling by the operator, as all the reagents were preloaded in the μPAD, with the only exception of hemin. The assay proved to be suitable for the detection of ATP amount in real samples in a relatively short period of time (i.e., approximately 1 h). The same approach could be used for other biomolecules as toxins and clinical markers. Future work is foreseen to evaluate the implementation of a smartphone's camera methods and a detector in the substitution of the portable CCD and dedicated application for data elaboration, to further improve assay portability and widespread applicability.

## 4.5 References


[1] Y. Seok Kim, N. H. Ahmad Raston, and M. Bock Gu, "Aptamer-based nanobiosensors," *Biosens Bioelectron*, vol. 76, pp. 2–19, Feb. 2016, doi: 10.1016/J.BIOS.2015.06.040.

[2] K. Tsukakoshi *et al.*, "Structural regulation by a G-quadruplex ligand increases binding abilities of G-quadruplex-forming aptamers," *Chemical Communications*, vol. 52, no. 85, pp. 12646–12649, Oct. 2016, doi: 10.1039/C6CC07552E.

[3] K. Chen *et al.*, "Aptamers as Versatile Molecular Tools for Antibody Production Monitoring and Quality Control," *J Am Chem Soc*, vol. 142, no. 28, pp. 12079–12086, Jul. 2020, doi: 10.1021/JACS.9B13370.

[4] R. Nutiu and Y. Li, "Structure-switching signaling aptamers," *J Am Chem Soc*, vol. 125, no. 16, pp. 4771–4778, Apr. 2003, doi: 10.1021/JA028962O/SUPPL_FILE/JA028962OSI20021224_123748.PD.

[5] S. Tyagi and F. R. Kramer, "Molecular beacons: probes that fluoresce upon hybridization," *Nat Biotechnol*, vol. 14, no. 3, pp. 303–308, 1996, doi: 10.1038/NBT0396-303.

[6] N. Hamaguchi, A. Ellington, and M. Stanton, "Aptamer beacons for the direct detection of proteins," *Anal Biochem*, vol. 294, no. 2, pp. 126–131, Jul. 2001, doi: 10.1006/abio.2001.5169.

[7] L. C. Bock, L. C. Griffin, J. A. Latham, E. H. Vermaas, and J. J. Toole, "Selection of single-stranded DNA molecules that bind and inhibit human thrombin," *Nature*, vol. 355, no. 6360, pp. 564–566, 1992, doi: 10.1038/355564A0.

[8] M. Rossetti and A. Porchetta, "Allosterically regulated DNA-based switches: From design to bioanalytical applications," *Anal Chim Acta*, vol. 1012, pp. 30–41, Jul. 2018, doi: 10.1016/J.ACA.2017.12.046.

[9] D. E. Huizenga and J. W. Szostak, "A DNA aptamer that binds adenosine and ATP," *Biochemistry*, vol. 34, no. 2, pp. 656–665, Jan. 1995, doi: 10.1021/BI00002A033.

[10] M. N. Stojanovic, P. De Prada, and D. W. Landry, "Fluorescent Sensors Based on Aptamer Self-Assembly," *J Am Chem Soc*, vol. 122, no. 46, pp. 11547–11548, Nov. 2000, doi: 10.1021/JA0022223.

[11] R. Yamamoto and P. K. R. Kumar, "Molecular beacon aptamer fluoresces in the presence of Tat protein of HIV-1," *Genes Cells*, vol. 5, no. 5, pp. 389–396, 2000, doi: 10.1046/J.1365-2443.2000.00331.X.

[12] P. S. Lau, B. K. Coombes, and Y. Li, “A general approach to the construction of structure-switching reporters from RNA aptamers,” *Angew Chem Int Ed Engl*, vol. 49, no. 43, pp. 7938–7942, Oct. 2010, doi: 10.1002/ANIE.201002621.

[13] S. Khan, B. Burciu, C. D. M. Filipe, Y. Li, K. Dellinger, and T. F. Didar, “DNAzyme-Based Biosensors: Immobilization Strategies, Applications, and Future Prospective,” *ACS Nano*, vol. 15, no. 9, pp. 13943–13969, Sep. 2021, doi: 10.1021/ACSNANO.1C04327.

[14] S. K. Silverman, “In vitro selection, characterization, and application of deoxyribozymes that cleave RNA,” *Nucleic Acids Res*, vol. 33, no. 19, pp. 6151–6163, Oct. 2005, doi: 10.1093/NAR/GKI930.

[15] Y. Cao *et al.*, “Investigation and improvement of catalytic activity of G-quadruplex/hemin DNAzymes using designed terminal G-tetrads with deoxyadenosine caps,” *Chem Sci*, vol. 11, no. 26, pp. 6896–6906, Jul. 2020, doi: 10.1039/D0SC01905D.

[16] I. Willner, B. Shlyahovsky, M. Zayats, and B. Willner, “DNAzymes for sensing, nanobiotechnology and logic gate applications,” *Chem Soc Rev*, vol. 37, no. 6, pp. 1153–1165, May 2008, doi: 10.1039/B718428J.

[17] X. Mao *et al.*, “Activity modulation and allosteric control of a scaffolded DNAzyme using a dynamic DNA nanostructure,” *Chem Sci*, vol. 7, no. 2, pp. 1200–1204, Jan. 2016, doi: 10.1039/C5SC03705K.

[18] A. Vallée-Bélisle and K. W. Plaxco, “Structure-switching biosensors: inspired by Nature,” *Curr Opin Struct Biol*, vol. 20, no. 4, p. 518, Aug. 2010, doi: 10.1016/J.SBI.2010.05.001.

[19] S. Stangherlin, N. Lui, J. H. Lee, and J. Liu, “Aptamer-based biosensors: from SELEX to biomedical diagnostics,” *TrAC Trends in Analytical Chemistry*, vol. 191, p. 118349, Oct. 2025, doi: 10.1016/J.TRAC.2025.118349.

[20] L. Peng *et al.*, “CRISPR-Cas12a based aptasensor for sensitive and selective ATP detection,” *Sens Actuators B Chem*, vol. 320, Oct. 2020, doi: 10.1016/J.SNB.2020.128164.

[21] K. Ratajczak, A. Lukasiak, H. Grel, B. Dworakowska, S. Jakiela, and M. Stobiecka, “Monitoring of dynamic ATP level changes by oligomycin-modulated ATP synthase inhibition in SW480 cancer cells using fluorescent ‘On-Off’ switching DNA aptamer,” *Anal Bioanal Chem*, vol. 411, no. 26, pp. 6899–6911, Oct. 2019, doi: 10.1007/S00216-019-02061-0/FIGURES/7.

[22] T. Doenst, T. D. Nguyen, and E. D. Abel, “Cardiac metabolism in heart failure: implications beyond ATP production,” *Circ Res*, vol. 113, no. 6, pp. 709–724, 2013, doi: 10.1161/CIRCRESAHA.113.300376.

[23] C. Ma, C. Lin, Y. Wang, and X. Chen, “DNA-based ATP sensing,” *TrAC Trends in Analytical Chemistry*, vol. 77, pp. 226–241, Mar. 2016, doi: 10.1016/J.TRAC.2016.01.013.

[24] B. R. Branchini *et al.*, “An enhanced chimeric firefly luciferase-inspired enzyme for ATP detection and bioluminescence reporter and imaging applications,” *Anal Biochem*, vol. 484, pp. 148–153, Jun. 2015, doi: 10.1016/j.ab.2015.05.020.

[25] X. F. Xue, F. Wang, J. H. Zhou, F. Chen, Y. Li, and J. Zhao, “Online cleanup of accelerated solvent extractions for determination of adenosine 5’-triphosphate (ATP), adenosine 5’-diphosphate (ADP), and adenosine 5’-monophosphate (AMP) in royal jelly using high-performance liquid chromatography,” *J Agric Food Chem*, vol. 57, no. 11, pp. 4500–4505, Jun. 2009, doi: 10.1021/JF900853Q.

[26] A. Zinellu *et al.*, “Ultra-fast adenosine 5’-triphosphate, adenosine 5’-diphosphate and adenosine 5’-monophosphate detection by pressure-assisted capillary electrophoresis UV detection,” *Electrophoresis*, vol. 31, no. 16, pp. 2854–2857, 2010, doi: 10.1002/ELPS.201000138.

[27] S. V. Khlyntseva, Y. R. Bazel’, A. B. Vishnikin, and V. Andruch, “Methods for the determination of adenosine triphosphate and other adenine nucleotides,” *Journal of Analytical Chemistry*, vol. 64, no. 7, pp. 657–673, Jun. 2009, doi: 10.1134/S1061934809070028/METRICS.

[28] Y. Li and J. Liu, “Aptamer-based strategies for recognizing adenine, adenosine, ATP and related compounds,” *Analyst*, vol. 145, no. 21, pp. 6753–6768, Oct. 2020, doi: 10.1039/D0AN00886A.

[29] C. Lyu, I. M. Khan, and Z. Wang, “Capture-SELEX for aptamer selection: A short review,” *Talanta*, vol. 229, Jul. 2021, doi: 10.1016/j.talanta.2021.122274.

[30] R. Nutiu and Y. Li, “In vitro selection of structure-switching signaling aptamers,” *Angew Chem Int Ed Engl*, vol. 44, no. 7, pp. 1061–1065, Feb. 2005, doi: 10.1002/ANIE.200461848.

[31] H. Qu, L. Wang, J. Liu, and L. Zheng, “Direct Screening for Cytometric Bead Assays for Adenosine Triphosphate,” *ACS Sens*, vol. 3, no. 10, pp. 2071–2078, Oct. 2018, doi: 10.1021/ACSSENSORS.8B00224.

[32] L. Zhang and J. C. Chaput, “In Vitro Selection of an ATP-Binding TNA Aptamer,” *Molecules 2020, Vol. 25, Page 4194*, vol. 25, no. 18, p. 4194, Sep. 2020, doi: 10.3390/MOLECULES25184194.

[33] E. Del Grosso, A. Idili, A. Porchetta, and F. Ricci, “A modular clamp-like mechanism to regulate the activity of nucleic-acid target-responsive nanoswitches with external activators,” *Nanoscale*, vol. 8, no. 42, pp. 18057–18061, Oct. 2016, doi: 10.1039/C6NR06026A.

[34] Y. Pan *et al.*, “Hollow covalent organic framework-sheltering CRISPR/Cas12a as an in-vivo nanosensor for ATP imaging,” *Biosens Bioelectron*, vol. 209, p. 114239, Aug. 2022, doi: 10.1016/J.BIOS.2022.114239.

[35] Y. Liu, L. Kong, H. Li, R. Yuan, and Y. Chai, “Electrochemical Aptamer Biosensor Based on ATP-Induced 2D DNA Structure Switching for Rapid and Ultrasensitive Detection of ATP,” *Anal Chem*, vol. 94, no. 18, pp. 6819–6826, 2022, doi: 10.1021/ACS.ANALCHEM.2C00613.

[36] A. Nascetti *et al.*, “Integrated chemiluminescence-based lab-on-chip for detection of life markers in extraterrestrial environments,” *Biosens Bioelectron*, vol. 123, pp. 195–203, Jan. 2019, doi: 10.1016/J.BIOS.2018.08.056.

[37] Q. Li *et al.*, “A self-powered rotating paper-based analytical device for sensing of thrombin,” *Sens Actuators B Chem*, vol. 351, p. 130917, Jan. 2022, doi: 10.1016/J.SNB.2021.130917.

[38] Monisha *et al.*, “Inkjet-printed paper-based colorimetric sensor coupled with smartphone for determination of mercury (Hg2+),” *J Hazard Mater*, vol. 414, p. 125440, Jul. 2021, doi: 10.1016/J.JHAZMAT.2021.125440.

[39] M. Yuan *et al.*, “Low-cost, portable, on-site fluorescent detection of As(III) by a paper-based microfluidic device based on aptamer and smartphone imaging,” *Mikrochim Acta*, vol. 190, no. 3, Mar. 2023, doi: 10.1007/S00604-023-05693-3.

[40] K. Shahsavar, M. Hosseini, E. Shokri, M. R. Ganjali, and H. Ju, “A sensitive colorimetric aptasensor with a triple-helix molecular switch based on peroxidase-like activity of a DNAzyme for ATP detection,” *Analytical Methods*, vol. 9, no. 32, pp. 4726–4731, Aug. 2017, doi: 10.1039/C7AY01381G.

[41] X. Chen, Y. Feng, H. Chen, Y. Zhang, X. Wang, and N. Zhou, “Fluorescent Aptasensor for Highly Specific Detection of ATP Using a Newly Screened Aptamer,” *Sensors*, vol. 22, no. 7, p. 2425, Apr. 2022, doi: 10.3390/S22072425/S1.

[42] G. Kibar, O. B. Şahinoğlu, B. Kılınçlı, E. Y. Erdem, B. Çetin, and V. C. Özalp, "Biosensor for ATP detection via aptamer-modified PDA@POSS nanoparticles synthesized in a microfluidic reactor," *Microchimica Acta*, vol. 191, no. 3, pp. 1–10, Mar. 2024, doi: 10.1007/S00604-024-06186-7/TABLES/2.

[43] E. Climent and K. Rurack, "Combining Electrochemiluminescence Detection with Aptamer-Gated Indicator Releasing Mesoporous Nanoparticles Enables ppt Sensitivity for Strip-Based Rapid Tests," *Angew Chem Int Ed Engl*, vol. 60, no. 50, pp. 26287–26297, Dec. 2021, doi: 10.1002/ANIE.202110744.

[44] A. Economou, C. Kokkinos, L. Bousiakou, and T. Hianik, "Paper-Based Aptasensors: Working Principles, Detection Modes, and Applications," *Sensors 2023, Vol. 23, Page 7786*, vol. 23, no. 18, p. 7786, Sep. 2023, doi: 10.3390/S23187786.

[45] Y. Sun and J. Lu, "Chemiluminescence-based aptasensors for various target analytes," *Luminescence*, vol. 33, no. 8, pp. 1298–1305, Dec. 2018, doi: 10.1002/BIO.3557.

[46] O. Trott and A. J. Olson, "AutoDock Vina: improving the speed and accuracy of docking with a new scoring function, efficient optimization, and multithreading," *J Comput Chem*, vol. 31, no. 2, pp. 455–461, Jan. 2010, doi: 10.1002/JCC.21334.

[47] J. He, J. Wang, H. Tao, Y. Xiao, and S. Y. Huang, "HNADOCK: a nucleic acid docking server for modeling RNA/DNA-RNA/DNA 3D complex structures," *Nucleic Acids Res*, vol. 47, no. W1, pp. W35–W42, Jul. 2019, doi: 10.1093/NAR/GKZ412.

[48] J. S. Kuo, "The effect of protective agents on the stability of plasmid DNA by the process of spray-drying," *J Pharm Pharmacol*, vol. 55, no. 3, pp. 301–306, Mar. 2003, doi: 10.1211/002235702702.

[49] P. Y. Hsieh *et al.*, "RNA Protection is Effectively Achieved by Pullulan Film Formation," *Chembiochem*, vol. 18, no. 6, pp. 502–505, Mar. 2017, doi: 10.1002/CBIC.201600643.

[50] Y. Ding and J. Liu, "Pushing Adenosine and ATP SELEX for DNA Aptamers with Nanomolar Affinity," *J Am Chem Soc*, vol. 145, no. 13, pp. 7540–7547, Apr. 2023, doi: 10.1021/JACS.3C00848.

[51] A. Roda, E. Michelini, L. Cevenini, D. Calabria, M. M. Calabretta, and P. Simoni, "Integrating biochemiluminescence detection on smartphones: mobile chemistry platform for point-of-need analysis," *Anal Chem*, vol. 86, no. 15, pp. 7299–7304, Aug. 2014, doi: 10.1021/AC502137S.

[52] Y. Yan, Z. Wen, D. Zhang, and S. Y. Huang, “Determination of an effective scoring function for RNA-RNA interactions with a physics-based double-iterative method,” *Nucleic Acids Res*, vol. 46, no. 9, May 2018, doi: 10.1093/NAR/GKY113.

[53] C. H. Lin and D. J. Patel, “Structural basis of DNA folding and recognition in an AMP-DNA aptamer complex: Distinct architectures but common recognition motifs for DNA and RNA aptamers complexed to AMP,” *Chem Biol*, vol. 4, no. 11, pp. 817–832, 1997, doi: 10.1016/S1074-5521(97)90115-0.

[54] S. Jahanshahi-Anbuhi *et al.*, “Simple and ultrastable all-inclusive pullulan tablets for challenging bioassays,” *Chem Sci*, vol. 7, no. 3, pp. 2342–2346, Feb. 2016, doi: 10.1039/C5SC04184H.

[55] D. Calabria *et al.*, “AstroBio-CubeSat: A lab-in-space for chemiluminescence-based astrobiology experiments,” *Biosens Bioelectron*, vol. 226, p. 115110, Apr. 2023, doi: 10.1016/J.BIOS.2023.115110.

# *Chapter 5*

*Chemiluminescence-enhanced type III CRISPR-Cas-based system for nucleic acid detection in lab-on-chip devices*

---

## 5.1 Introduction

CRISPR-Cas (Clustered Regularly Interspaced Short Palindromic Repeats/CRISPR-associated) systems function as an adaptive immune mechanism in numerous bacteria and archaea, providing protection against viruses and other mobile genetic elements (MGEs) [1]. A CRISPR array is composed of alternating repeat and spacer sequences. The repeat sequences are identical, while the spacers contain distinct sequence fragments derived from invading MGEs. This array is typically situated in proximity to *cas* genes, which encode the Cas proteins. The CRISPR-Cas system functions through three sequential stages: adaptation, crRNA biogenesis, and interference [2]. During the adaptation phase, short fragments of foreign DNA, known as protospacers, are incorporated into the CRISPR locus as new spacers, establishing a heritable molecular record of prior infections. Subsequently, the CRISPR array is transcribed and processed into mature CRISPR RNAs (crRNAs), which assemble with Cas proteins to form effector complexes. In the interference stage, these complexes identify and bind complementary sequences within invading nucleic acids, guided by the presence of a protospacer adjacent motif (PAM), and mediate the cleavage of the foreign genetic material. This process effectively neutralizes the mobile genetic element and provides sequence-specific adaptive immunity to the host cell.

***Table 5.1**. Classification of the CRISPR-CAS system.*

| Class | Type | Representative Cas Protein(s) | Target | Key Features / Biosensing Use |
|---|---|---|---|---|
| **Class 1** | I | Cas3 (Cascade complex) | dsDNA | Multi-protein effector; limited biosensing use. |
| | III | Cas10–Csm/Cmr complex | RNA (primary), DNA (secondary) | Dual RNA/DNA activity; cOA signalling enables self-amplified detection; emerging in RNA-based biosensors. |
| | IV | Csf complex | DNA (unclear) | Poorly characterized; limited data. |
| **Class 2** | II | Cas9 | dsDNA | Precise cleavage; PAM (NGG) required; standard in DNA biosensors. |
| | V | Cas12a (Cpf1), Cas14 | dsDNA / ssDNA | Collateral ssDNA cleavage; T-rich PAM; used in DETECTR-type sensors. |
| | VI | Cas13a/b | ssRNA | RNA-specific; collateral RNA cleavage; basis of SHERLOCK assays. |

The CRISPR-Cas systems are broadly classified into two main classes and further subdivided into six distinct types based on their signature effector proteins (Table 5.1). Class 1 systems include types I, III, and IV, which employ multi-protein effector complexes, whereas Class 2 systems comprise types II, V, and VI, characterized by single, multidomain effector proteins such as Cas9, Cas12, and Cas13 [3].

By harnessing the specific cis/trans-cleavage activities of the CRISPR/Cas system, researchers have developed nucleic acid detection technologies that exhibit single-molecule sensitivity, single-nucleotide specificity, portability, and cost-effectiveness. As a result, nucleic acid-based methodologies are emerging as the foundation of next-generation in vitro diagnostics, particularly due to their versatility and suitability for deployment in resource-limited settings.

CRISPR-based biosensors employ various detection strategies that exploit the nuclease activity of Cas proteins to identify nucleic acid targets. The most common approaches include fluorescence, which uses labelled probes to generate a signal upon target cleavage; colorimetric assays, where chemical reactions produce visible colour changes for easy readout; potentiometric methods, which detect changes in electrical potential associated with Cas activity; and lateral flow assays (LFA), which allow rapid, instrument-free detection similar to point-of-care tests. These detection strategies are often coupled with isothermal amplification techniques, such as recombinase polymerase amplification (RPA), to enhance sensitivity and reduce assay time, making CRISPR-based biosensors highly versatile and suitable for rapid diagnostics [3].

Cas9, Cas12 and Cas13 have emerged as the most widely adopted effectors due to their programmability and collateral cleavage activities. Cas9 has been employed in biosensors for the detection of viral DNA and genetic mutations, often integrated with electrochemical or fluorescence-based platforms for high specificity and sensitivity [4], [5]. For example, Cas9-based sensors have been used to detect mutations in cancer-related genes and antibiotic resistance markers. Cas12 and Cas13, on the other hand, have gained prominence for their trans-cleavage activity, which enables signal amplification upon target recognition. This property has been harnessed in lateral flow assays and fluorescent biosensors for detecting pathogens such as *Salmonella typhimurium* and SARS-CoV-2 variants [6]. Cas12-based biosensors have also demonstrated high sensitivity in single nucleotide variant (SNV) detection, making them suitable for clinical diagnostics. Cas13, which targets single-stranded RNA, has shown great promise in RNA virus detection. A notable example is its use in a colorimetric biosensor for influenza A (H1N1), where Cas13a's trans-cleavage activity triggered a

hybridization chain reaction that amplified the signal, enabling visual detection with high sensitivity [7].

In contrast, type III CRISPR systems remain largely unexplored in biosensing applications. Although they possess unique features such as cyclic oligoadenylate (cOA) signalling and RNA-targeting capabilities, their complex multi-protein architecture and limited understanding of effector dynamics have hindered their integration into biosensor platforms [5]. Current literature reveals few works regarding practical implementations of type III systems in biosensing, underscoring the need for further research to unlock their potential. Type III CRISPR-based biosensors offer a highly promising platform for next-generation diagnostics. Indeed, this unique combination of built-in signal amplification, dual targeting mechanisms, and compatibility with label-free, amplification-free formats makes them particularly well-suited for point-of-care use, especially in settings where traditional laboratory infrastructure is limited.

In type III CRISPR-Cas systems, the CRISPR array is transcribed into a precursor CRISPR RNA (pre-crRNA), which undergoes endonucleolytic cleavage by the Cas6 ribonuclease to generate intermediate crRNA species [8]. These intermediates are further processed via 3′-end trimming to yield mature crRNAs of defined length [9], [10]. The mature crRNA assembles with multiple Cas proteins to form a ribonucleoprotein effector complex, typically comprising Cas10 and several copies of Cas7, among other subunits. During the interference phase, type III systems exhibit dual nucleic acid targeting capabilities, enabling degradation of both RNA and DNA substrates. This contrasts with other CRISPR-Cas types, which generally exhibit substrate specificity for either DNA (types I, II, and V) or RNA (type VI) [11], [12], [13], [14], [15], [16]. Target recognition is initiated by base pairing between the crRNA and a complementary RNA transcript, which triggers a cascade of enzymatic activities. The Cas7 subunits, arranged in a helical filament, cleave the bound target RNA at 6-nucleotide intervals via their intrinsic RNase activity [17], [18].

Concurrently, target RNA binding allosterically activates the Cas10 subunit, a multidomain protein harbouring both HD and Palm domains [15], [19], [20]. The HD domain mediates sequence-independent cleavage of single-stranded DNA, while the Palm domain catalyses the synthesis of cyclic oligoadenylate (cOA) second messengers from ATP. These cOAs bind to and activate CRISPR-associated Rossmann fold (CARF) domain-containing accessory proteins, such as Csm6 or Csx1, which function as non-specific RNases. The resulting widespread RNA degradation can induce cellular dormancy or programmed cell death, thereby limiting the propagation of mobile genetic elements [21], [22], [23].

Briefly, sequence-specific recognition of RNA by type III CRISPR-cas systems initiates a signalling cascade. RNA binding by the type III Complex triggers a conformational change that activates the Palm domain of the Cas10 subunit, which amplifies the RNA binding signal by converting ATP into ~1000 cyclic oligoadenylates (e.g., $cOA_4$) [24]. This intrinsic signal amplification unique of the type III CRISPR systems can boost the sensitivity of direct RNA detection while maintaining specificity, therefore making it ideal for biosensing applications [19]. In analytical contexts, nucleic acids are often preferred for detection due to their superior thermal stability compared to proteins or lipids, making them particularly suitable for analyses in extreme environmental conditions. RNA, in particular, offers unique advantages over DNA as a biomarker. Its expression reflects real-time cellular activity, enabling dynamic monitoring of disease progression, treatment responses, and environmental influences. These features make RNA an ideal biomarker, offering early disease detection, enhanced specificity, non-invasive sampling, and high sensitivity for detecting low-abundance targets [26].

Recently, a type of system has already been developed and made commercially available for highly accurate diagnostics to the point of need. In this method, the signal amplification potentiality of type III CRISPR-Cas system was exploited, by coupling the production of second messengers to an easy read-out. To this end, a cOA-dependent nonspecific RNase (Csx1) was selected to establish a synthetic signalling pathway in which the TtCmr/crRNA complex (type III CRISPR-Cas effector complex of *Thermus thermophilus*) recognise the target RNA and produces cOAs. As a result, activated Csx1 cleaves a reporter RNA, generating a detectable fluorescent signal [27]. Although this system is very promising, the technique relies on a fluorescence detection that requires photoexcitation, thus hampering the assay miniaturization for the development of a portable analytical devices for Point-of-Care applications [28].

To overcome this limitation, we explored the possibility to utilize the same TtCmr-mediated activation of Csx1 RNAse to detect nucleic acid sequences, employing a chemiluminescent (CL) readout for enhanced sensitivity, ease of use and amenability of miniaturization. The key advantage of this detection technique lies in its operation without the need for external light sources, enabling highly sensitive photon detection with minimal background interference, a limitation often encountered in photoluminescence-based assays. In addition, as filters are not required, nor specific geometries for signal readout, thus providing amenability for miniaturization. As a result, chemiluminescence-based analytical methods offer inherently high sensitivity and represent both a robust alternative and a valuable complement to traditional optical biosensing strategies [29].

Indeed, the ultimate goal is to develop CRISPR-based technologies that are sensitive enough to detect the target RNA directly, without prior amplification.

To test this hypothesis, we employed a guanine-rich RNA probe (G4), capable of forming a catalytically active G-quadruplex and catalyse the CL reaction, serving as a target for Csx1.

Hence, G-quadruplexes are non-canonical nucleic acid structures with stacked G-tetrads assembled by Hoogsteen hydrogen-bonding [30]. Owing to their unique structural topology and crucial biological roles, G-quadruplexes have garnered considerable scientific interest. A particularly noteworthy property of G4s is their capacity to complex with hemin (iron(III)-protoporphyrin IX), yielding G4-based DNAzymes and RNAzymes that mimic peroxidase activity [31].

Compared to natural protein-based peroxidases, G4 RNAzymes offer several advantages, including compact molecular size, straightforward chemical synthesis, ease of handling, and compatibility with rationally designed allosteric regulation. These features make them a highly versatile catalytic platform for applications in biosensing, biomaterials, and biomolecular engineering [32], [33], [34]. G4 RNAzymes have been widely utilized as signal-generating elements in the development of different biosensors and molecular devices and have emerged as promising biocatalysts effective in both aqueous and non-aqueous environments [34], [31]. Given these properties, RNAzymes represent highly suitable candidates for the development of CRISPR-based sensing strategies.

In this work, we present an analytical approach for the detection of nucleic acid sequences, employing 4.5 target RNA as the recognition template. In particular, a novel chemiluminescence-based analytical approach was developed for detecting nucleic acid sequences and integrated into a platform composed of a microfluidic chip coupled either to a portable photosensor array or to a smartphone readout. The 4.5 target RNA sequence was selected as the target model, as it is known to activate the TtCmr/Csx1 complex employed in this study.

In this assay, the 4.5 target RNA sequence binds to and activates the TtCmr/crRNA complex, consequently activating the Csx1 RNAse that digests the G4 RNAzyme sequence preventing it from adopting a secondary structure capable of binding hemin and catalysing the oxidation of luminol by hydrogen peroxide. So, in the presence of the Target sequence a weak CL signal is generated, whereas in the absence of the target sequence an intense CL signal is obtained. As a results, the chemiluminescent intensity is inversely proportional to the concentration of the target sequence (Figure 5.1).

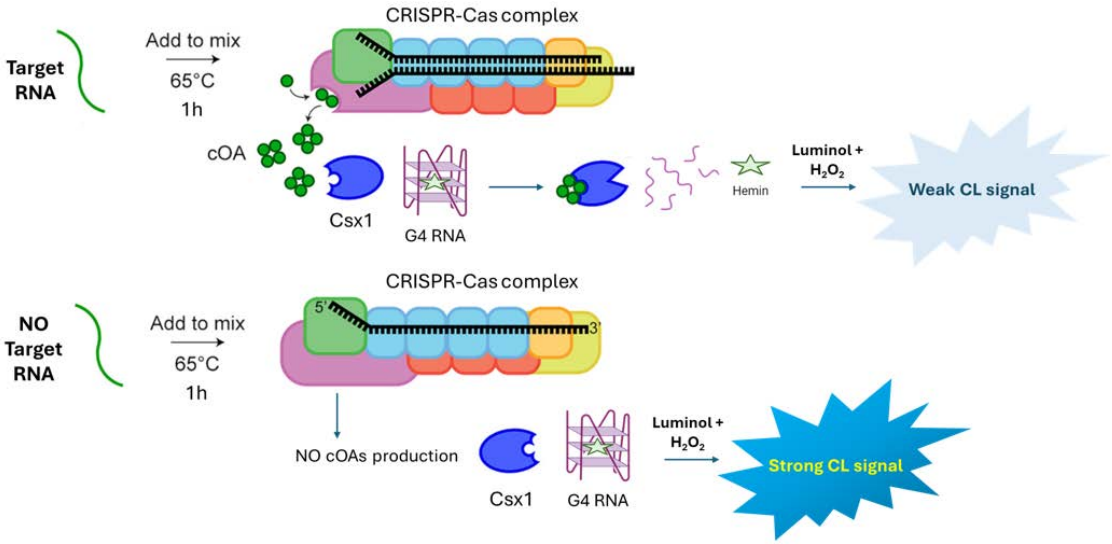


***Figure 5.1.*** *Schematic representation of the detection mechanism: in the presence of the target sequence a weak chemiluminescent signal is generated, while in its absence, an intense CL signal is observed.*

## 5.2 Materials and Methods

### 5.2.1 Reagents and materials

TtCmr/crRNA complex, ATP, Csx1, $MgCl_2$ and 4.5 target RNA were the components of the "Type III CRISPR-Cas Test" for target RNA detection were generously provided by SCOPE Biosciences B.V. (The Netherlands). Hemin, luminol sodium salt, hydrogen peroxide, Trizma HCl, NaCl, KCl, $NH_4OH$ were purchased from Sigma-Aldrich (St. Louis, MO). Cyclic tetraadenosine monophosphate ($cOA_4$) sodium salt was purchased from Biolog Life Science Institute GmbH & Co. KG (Germany).

The following buffers, prepared in Milli-Q Plus ultra-pure water, were used in the preparation of the stock solutions and in the enzymatic assays: phosphate buffered saline (PBS, 0.01 mol $L^{-1}$ phosphate buffer containing 137 mmol $L^{-1}$ NaCl and 2.7 mmol $L^{-1}$ KCl, pH 7.4), TE buffer (10 mmol $L^{-1}$ Tris, 0.1 mmol $L^{-1}$ EDTA, pH 8.0), CRISPR-Cas reaction buffer (10 mmol $L^{-1}$ Tris-HCl pH 8.2, 7 mmol $L^{-1}$ $NH_4OH$, and 2 mmol $L^{-1}$ $MgCl_2$).

The single-stranded G-quadruplex (ssRNA, G4) RNAzyme was purchased from Integrated DNA Technologies (IDT, Coralville, IA, USA).

The CL measurements in microplates were performed in black 96-well microtiter plates using a Varioskan LUX microtiter plate luminometer (Thermo Scientific, Waltham, MA, USA).

### 5.2.2 DNA sequences

The G-quadruplex RNAzyme oligonucleotide probe was used as provided and diluted in pH 8.0, TE buffer solution to give stock solution of 100 μmol $L^{-1}$. The sequence of the RNA is as follows:

G4 RNAzyme: 5'-GGGUAGGGCGGGUUGGGA-3'

The short RNA sequence contains four guanine-rich regions, known as G-tetrads (GGG), which can form a unique type of RNAzyme with peroxidase-like activity in the presence of hemin. These G-tetrads are separated by loop sequences (UAG, UUG).

The TtCmr/crRNA complex has been loaded with a crRNA that is specific for the Target RNA 4.5 used as a model for this method. The sequences of the crRNA and the Target RNA 4.5 are as follows:

crRNA 4.5, 46 nts:

5'-AUUGCGACCCGUAGAUAAGGCGCCCGGGGACGACCACGUCAAGGCG-3'

4.5 target RNA, 50 nts:

5'-GUUGUGCGCCUUGACGUGGUCGUCCCCGGGCGCCUUAUCUACGGCAGCGU-3'

The selectivity of the method was assessed by testing a non-target RNA sequence and a non-target DNA sequence:

NT RNA, 21 nts: 5'- UAGCUUAUCAGACUGAUGUUG-3'

NT DNA, 36 nts: 5'-AAAAAACTAAGTAACTCTGCACTCTTTAGCCCTGAT-3'

Before each use, all the sequences were heated to 75 °C for 5 minutes to disrupt any secondary structures ensuring that the strands are fully linearized and accessible for subsequent processes.

### 5.2.3 Type III CRISPR Cas - based RNA detection

The 4.5 target RNA detection assays were conducted in CRISPR-Cas reaction buffer to which TtCmr/crRNA complex (62.5 nmol $L^{-1}$ final concentration), ATP (1 mmol $L^{-1}$ final concentration), Csx1 RNAse (1,2 μmol $L^{-1}$ final concentration), G4 RNAzyme probe (250 nmol $L^{-1}$ final concentration) as well as the RNA substrates (0.1 nmol $L^{-1}$, 0.5 nmol $L^{-1}$ , 1 nmol $L^{-1}$ , 5 nmol $L^{-1}$ , 10 nmol $L^{-1}$ , 100 nmol $L^{-1}$) were added (solution 1). The 20 μL reaction of solution 1 was incubated at 65 °C for 1 h and then 20 μL of hemin (0.25 μmol $L^{-1}$ final concentration; solution 2) were added to bind to the uncleaved G4 RNAzyme probe for 30 min at room temperature.

Finally, 40 µL of CL mixture (luminol 0.3 mmol $L^{-1}$, hydrogen peroxide 12 mmol $L^{-1}$ final concentrations, in reaction buffer pH 8.2; solution 3) were added so that a light signal indirectly proportional to the different concentrations of 4.5 target RNAs tested was generated. The CL signal was acquired via the Varioskan LUX microtiter plate luminometer for 2 min, setting an integration time of 50 ms.

### 5.2.4 Type III CRISPR Cas - based RNA detection – Portable formats

Demonstrated the validity of the test for the detection of 4.5 target RNA, the method was coupled with two portable detectors.

#### 5.2.4.1 Lab-on-Chip device

The PMMA (Polymethyl methacrylate) microfluidic chip employed in this work was designed with tapered reaction chambers. This design leverages the tendency of water to creep into confined spaces on hydrophilic substrates, with the driving force influenced by channel dimensions and taper angle. The device comprises four independent chambers, enabling the simultaneous analysis of four different samples.

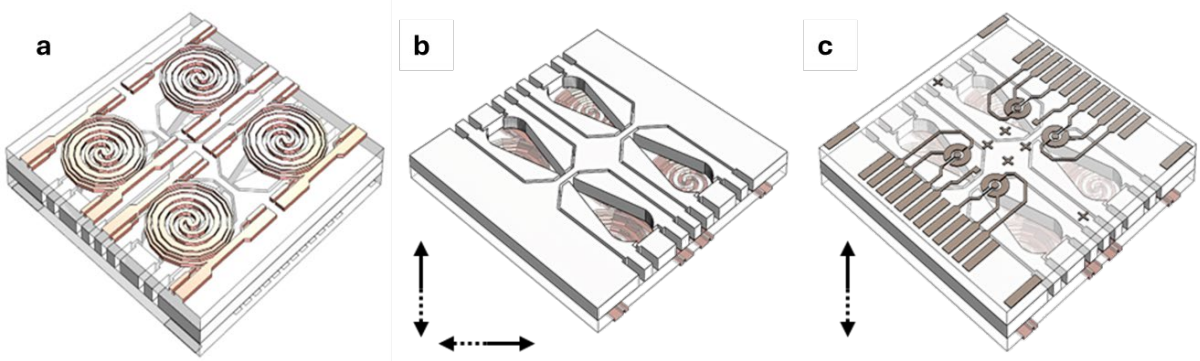


***Figure 5.2.*** *Chip design containing four chambers. (a) top view of the heating elements. (b) view of the tapered chambers and microfluidic network. (c) photosensitive diode and thermal sensor (the chip is rotated and flipped upside-down).*

The microfluidic chip was coupled with a system on glass where thermalization, temperature control and CL detection are all integrated on a single glass substrate (Figure 5.2) [35]. Hydrogenated amorphous silicon (a-Si:H) diodes have been chosen as basic structure for the thin film sensor [36] because of its optoelectronic characteristics (Figure 5.3b) [37], [38].

In particular, a-Si:H photosensors have been shown to be well-suited for detecting chemiluminescence (CL) signals. Moreover, their analytical performance in CL-based biomolecule detection is comparable to that of state-of-the-art laboratory imaging systems based on cooled crystalline silicon charge-coupled devices (CCDs) [39], [40]. The set-up is housed in a dark metal box that contains all the electronic components required for operating the photosensors and the heater (Figure 5.3a). A lid prevents interference from ambient light during measurements. The lab-on-chip connects to the user through a graphical user interface (GUI), which enables real-time adjustment of experimental parameters. The complete device was developed within the framework of the ALCYONE project (Sapienza University of Rome, Horizon Europe, Grant agreement ID: 101082679).

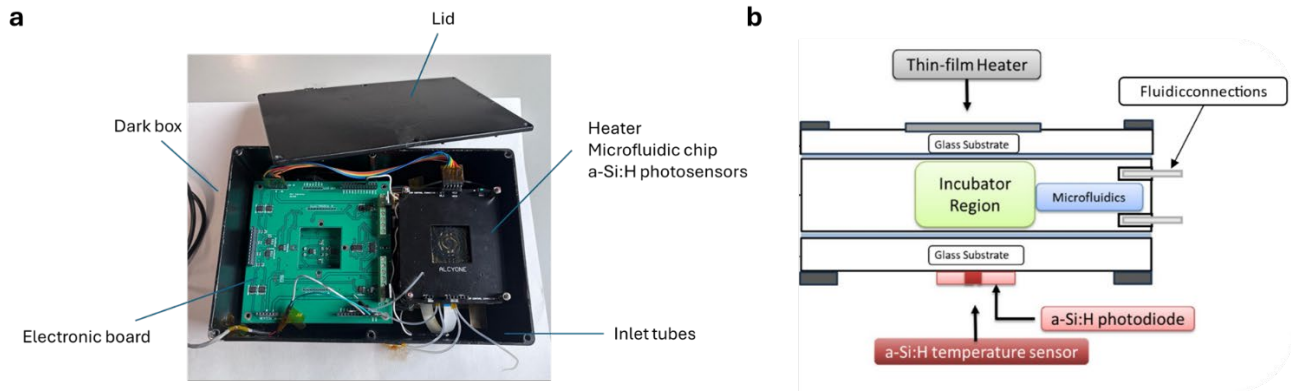


***Figure 5.3**. (a) Dark box containing the complete set-up to operate the lab-on-chip and (b) cutaway view of the lab-on-chip portable device.*

To ensure proper mixing of the reagents and effective coupling with the photosensors, the CL reaction was fully conducted within each chamber of the microfluidic chip. 4.5 target RNA is added to solution 1 and immediately injected into the pre-heated chamber. The solution is incubated for 1 h at 65 °C and then a solution with hemin (solution 2) is added using the input channel of the microfluidic chip. After 30 min, the CL cocktail (solution 3) is injected into the chamber and real time signals are acquired for 200 seconds.

Injected volumes were selected considering the diameter of the inlet channels in order to have the same liquid amount inside the chamber as used for the microtiter plate test (0.08 mL total). The flow rate was set at 10 mL $h^{-1}$ which was optimal to have a rapid entry and good mixing of the reagents within the reaction chamber.

### 5.2.4.2 Smartphone's CMOS Camera

An iPhone 15 (Apple, 2024) CMOS camera was used as a detector to acquire images of the CL emission produced inside the microfluidic chip. The chip was the same as that used for coupling with the photosensors, following the same procedure. Each image was acquired for 30 seconds after the inflow of solution 3 into the reaction chamber. To prevent external light interference, a 3D-printed dark box with a smartphone holder on the top was employed during the signals acquisition (Figure 5.4).

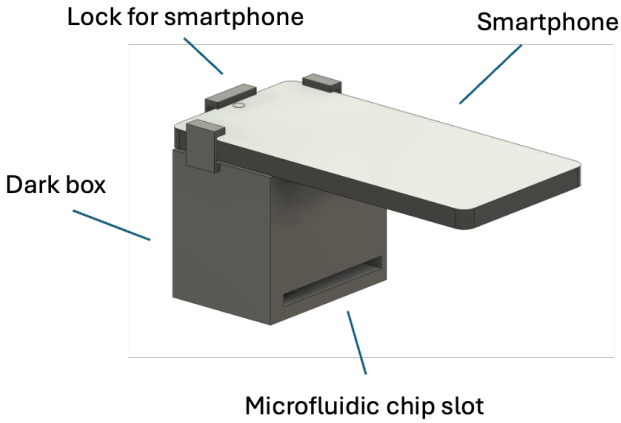


***Figure 5.4*** *Scheme of the 3D-printed dark box used in this assay employing smartphone-based CL detection. Key components include the dark box, smartphone holder, and microfluidic chip slot.*

### 5.2.5 Data elaboration and processing

Quantitative measurements were performed at least in three replicates. Data analysis was performed using MATLAB (The MathWorks, Inc., Natick, MA, USA, version 2024a) or ImageJ v.1.53h software (National Institutes of Health, Bethesda, MD). GraphPad Prism software (GraphPad Software, San Diego, CA, USA, version 9) was employed for data graphing and regression analysis.

## 5.3 Results and discussion

### 5.3.1 Optimization of experimental conditions

The experimental conditions were optimized to maximize the chemiluminescent yield. In particular, parameters such as signal intensity, stability, and signal-to-noise ratio were rigorously evaluated.

Since the CL reaction needs an alkaline pH and it is widely known that G4 structures require monovalent ions to fold, alkaline buffers with different salt components were tested. PBS + $MgCl_2$ and TRIS-HCl + $MgCl_2$ supplemented with different ions were examined to find the best signal-to-noise ratio between hemin and G4 + hemin (Table 5.2). $MgCl_2$ 2 mmol $L^{-1}$ is essential for the activity of RNase, so it must be present in all relevant conditions. Hemin alone can catalyse the chemiluminescent reaction, producing a constant background signal. Upon addition of G4, a complex with hemin is formed, leading to a pronounced increase in the CL signal.

***Table 5.2**. List of buffers tested to determine the optimal reaction conditions.*

| **Buffers Figure 5.5a** | **Buffers Figure 5.5b** |
|---|---|
| TRIS-HCl[a] + $MgCl_2$ [c] + NaCl[d] pH 7.5 | TRIS-HCl[a] + $MgCl_2$ [c] + $NH_4OH$[f] pH 8.2 |
| TRIS-HCl[a] + $MgCl_2$ [c] + KCl[e] pH 7.5 | TRIS-HCl[a] + $MgCl_2$ [c] + $NH_4OH$[f] + NaCl[d] pH 8.2 |
| TRIS-HCl[a] + $MgCl_2$ [c] + $NH_4OH$[f] pH 8.2 | TRIS-HCl[a] + $MgCl_2$ [c] + $NH_4OH$[f] + KCl[e] pH 8.2 |
| PBS[b] + $MgCl_2$ [c] pH 7.4 | TRIS-HCl[a] + $MgCl_2$ [c] + $NH_4OH$[f] + NaCl[d] + KCl[e] pH 8.2 |

*[a] TRIS-HCl 10 mmol $L^{-1}$, [b] PBS 10 mmol $L^{-1}$, [c] $MgCl_2$ 2 mmol $L^{-1}$, [d] NaCl 200 mmol $L^{-1}$, [e] KCl 100 mmol $L^{-1}$, [f] $NH_4OH$ 7 mmol $L^{-1}$*

Thus, a 1:1 ratio (i.e. 250 nmol $L^{-1}$ each) of hemin to G4 was used [31] for buffer and, as shown in Figure 5.5a, best results were obtained for the TRIS-HCl with $NH_4OH$ buffer. Subsequently, to further improve the signal-to-noise ratio, different ion combinations were tested with the previously chosen buffer. The graph in Figure 5.5b shows that all the tested combinations worsen the performance of G4. Consequently, all subsequent experiments were carried out using the TRIS-HCl 10 mmol $L^{-1}$ with $MgCl_2$ 2 mmol $L^{-1}$ and $NH_4OH$ 7 mmol $L^{-1}$, pH 8.2. This finding is in line with the literature since buffer enriched with $NH_4OH$ was found to provide the highest signal-to-background ratios for the luminol/$H_2O_2$ CL [41].

These experiments were carried out by incubating G4 + hemin and hemin alone for 30 minutes at room temperature. To assess the optimal signal-to-noise ratio, the CL signal from each G4 + hemin sample was compared to the signal obtained with hemin alone. Signals were detected using a CL cocktail (0.3 mmol $L^{-1}$ luminol and 12 mmol $L^{-1}$ hydrogen peroxide), dispensing the solutions into a 96 well microtiter plate and using a plate reader (Varioskan LUX) as a detector.

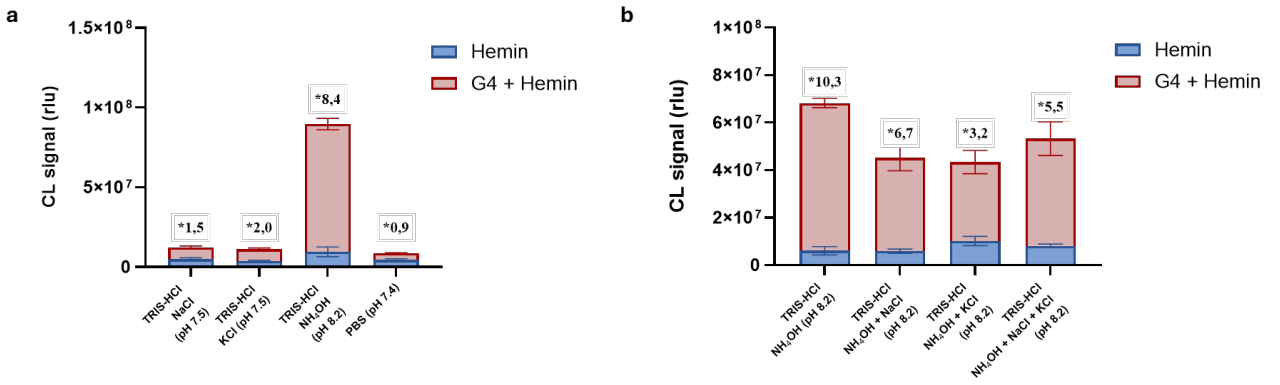


***Figure 5.5.*** *(a) CL maximum emission intensities obtained with different buffers in the presence of a 1:1 ratio of hemin to G4, 250 nmol $L^{-1}$ each. (b) CL maximum emission intensities obtained by combining different salts to the chosen buffer, in the presence of a 1:1 ratio of hemin to G4, 250 nmol $L^{-1}$ each. Each data is the mean ± SD of three independent measurements. * Signal-to-noise ratio between G4 + hemin and hemin alone.*

### 5.3.2 Type III CRISPR-based RNA CL detection – Microtiter plate format

The test for detection and quantification of the target RNA was initially optimized in a microtiter plate using the TtCmr/crRNA complex with the addition of RNase Csx1 and the G4 RNA reporter, following the procedure described in paragraph 5.2.3. As shown by the curves in Figure 5.6a, an inverse proportionality was observed between the intensity of the chemiluminescent reaction and the tested 4.5 target RNA concentrations. Using this setup, a minimal detectable concentration of 0.1 nmol $L^{-1}$ target RNA concentration was achieved with a CL signal detectable within seconds after starting the acquisition. The corresponding calibration curve was generated by plotting the peak signal from each kinetic curve as a function of the corresponding 4.5 target RNA concentration (Figure 5.6b). The calibration curve displays a downward trend, reflecting the decrease in signal intensity when increasing 4.5 target RNA concentration, consistent with the behaviour observed in the reaction kinetics. The detection limit (LOD) is 1 nmol $L^{-1}$ and was calculated as the blank signal peak plus three times its standard deviation.

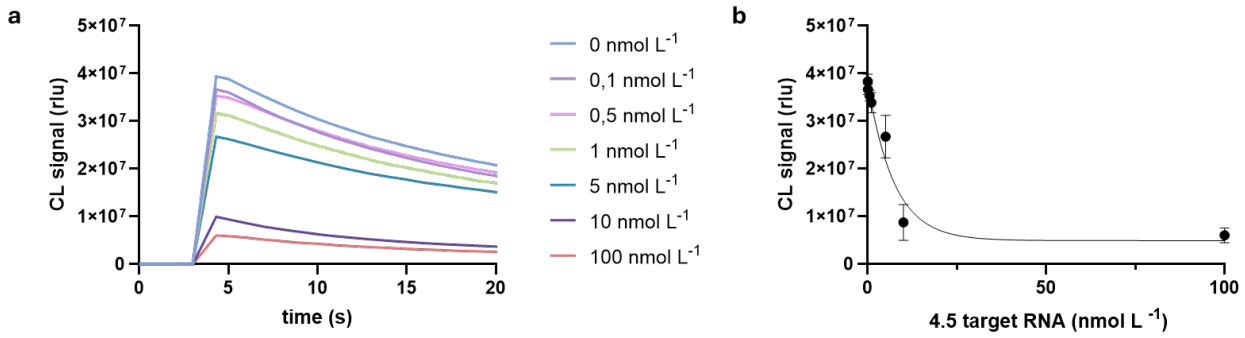


***Figure 5.6.*** *(a) Kinetic profiles of the CL emission obtained for the analysis of samples with different concentrations of 4.5 target RNA in a microtiter plate format and (b) the corresponding calibration curve. The equation of the calibration curve (one phase decay) in the 0.1 – 100 nmol $L^{-1}$ concentration interval is $Y = 33168868 \times e^{(-0.1356X)} + 4957156$ ($R^2 = 0.955$), where Y and X are the CL signal and the concentration of 4.5 target RNA, respectively.*

### 5.3.3 Type III CRISPR-based RNA CL detection – Photosensors

To obtain an RNA biosensor suitable for onsite applications we worked on the portability of the analytical system by exploiting a CL-based integrated analytical platform employing a microfluidic network and an array of photosensors to perform CL bioassay for highly sensitive detection.

The solution-based assay was adapted to a microfluidic chip and consists of three successive additions of solutions into the reaction chamber. Indeed, 4.5 target RNA was mixed with the CRISPR-Cas reagent solution to initiate the reaction, injected into the pre-heated chamber, and incubated at 65 °C for 1 h. After addition of the hemin-containing solution and a 30 min incubation, the CL cocktail was introduced, and luminescence signals were recorded for 200 s.

This setup ensures slower and more homogeneous mixing of reagents compared to the microtiter plate format. At the same time, it allows the entire analytical protocol to be carried out within a single chamber, thanks to the integrated heater.

Figure 5.7a displays the kinetic profiles recorded with the photosensors integrated into the portable device. The corresponding calibration curve (Figure 5.7b) was constructed by plotting the peak signal of each kinetic trace as a function of the respective 4.5 target RNA concentration. A LOD of 0.545 nmol $L^{-1}$, approximately half the value previously obtained, demonstrated the improvement of the analytical performance of the method.

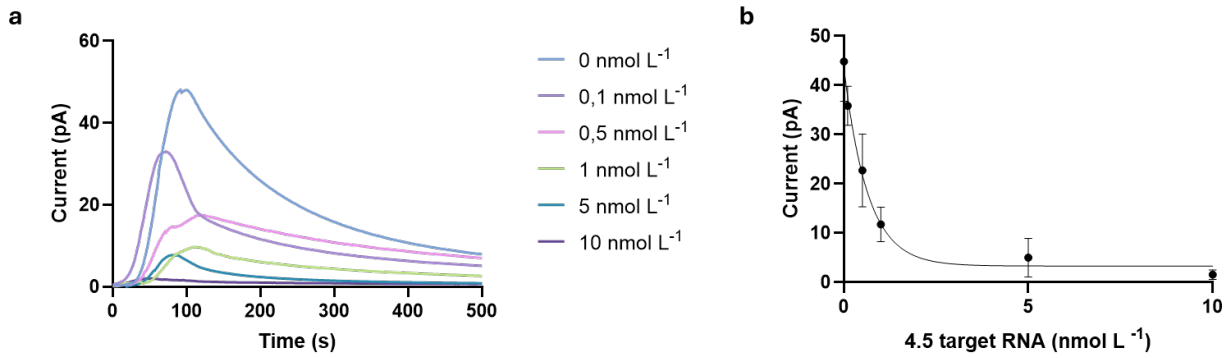


***Figure 5.7.*** *(a) Kinetic profiles of the CL emission obtained for the analysis of samples with different concentrations of 4.5 target RNA employing the photosensor format and (b) the corresponding calibration curve. The equation of the calibration curve (one phase decay) in the 0.1 – 10 nmol L$^{-1}$ concentration interval is* $Y = 40.226 \times e^{(-1.546X)} + 3{,}324$ *($R^2 = 0.991$), where Y and X are the CL signal and the concentration of 4.5 target RNA, respectively.*

### 5.3.4 Assay specificity

To evaluate assay specificity, two different oligonucleotides sequences were analysed as potential targets. Specifically, we tested a DNA oligonucleotide (NT DNA, 100 nmol L$^{-1}$) and an RNA oligonucleotide (NT RNA, 100 nmol L$^{-1}$), both with sequences and lengths different from the correct target RNA and we compared the results with the maximum (4.5 target RNA, 0 nmol L$^{-1}$) and minimum (4.5 target RNA, 100 nmol L$^{-1}$) signals obtainable with this analytical method. The results (Figure 5.8) show that, even at such relatively high concentrations, NT DNA and NT RNA are not significantly recognized by the CRISPR-Cas complex and therefore the RNase responsible for signal reduction is not activated.

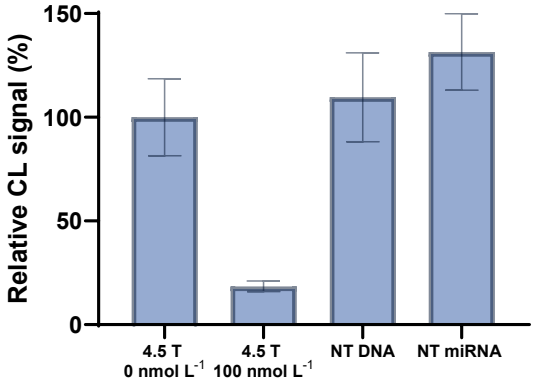


***Figure 5.8.*** *Relative CL (%) signals measured for the potentially interfering non-target sequences prepared at 100 nmol L$^{-1}$ in the presence of 0.3 mmol L$^{-1}$ luminol and 12 mmol L$^{-1}$ hydrogen peroxide.*

### 5.3.5 CMOS camera detection

To further increase the portability of this method, the possibility to detect the CL signal of the developed biosensor by smartphone CMOS camera was investigated. 4.5 target RNA was mixed with the CRISPR-Cas reagents, injected into the pre-heated chamber, and incubated at 65 °C for 1 h. Hemin solution was then added for 30 min, followed by the CL cocktail. The microfluidic chip was placed inside a dark box to enable accurate acquisition of the CL signal, which was recorded for 30 s at ISO 6400, using an IPhone15 smartphone (Apple, 2024) with the proprietary camera app (Figure 5.9a). The CL images were analysed using the freeware ImageJ v.1.53h software (National Institutes of Health, Bethesda, MD). Regions of interest (ROIs) corresponding to the reaction chambers were defined and the CL emission intensities were evaluated by integrating the CL emissions on the ROI areas (Figure 5.9b). As shown in Figure 5.9c, we can discriminate three different 4.5 target RNA concentrations in good agreement with previously data.

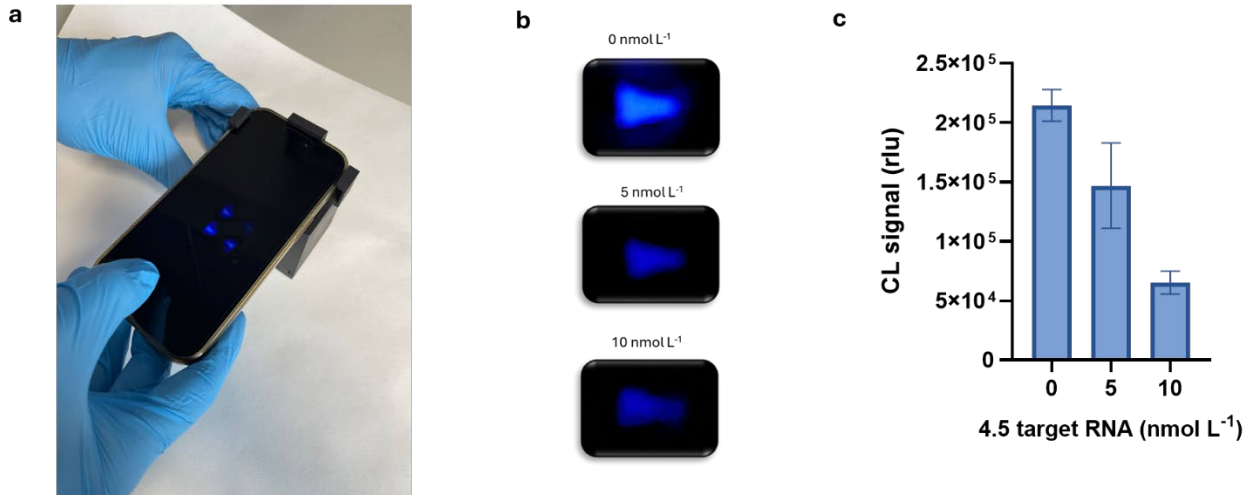


***Figure 5.9.*** *(a) Images taken during the measurement of the CL emission in the microfluidic chip. (b) CL emission obtained for the analysis of three samples with different concentrations (low, medium, high) of 4.5 target RNA employing a smartphone detection, in the presence of 0.3 mmol $L^{-1}$ luminol and 12 mmol $L^{-1}$ hydrogen peroxide. (c) Elaboration of CL image with ImageJ v.1.53h software to quantify the CL signal of each sample.*

## 5.4 Conclusions

This study presents a proof-of-concept for a sensitive, specific, and rapid diagnostic test based on the type III CRISPR-Cas system. The protocol for detecting the 4.5 target RNA was optimized and then configured for compatibility with portable devices. Initial evaluation of biosensor performance was carried out using a luminometer for CL signal detection, followed by a feasibility study assessing the

quantification of different concentrations of 4.5 target RNA. However, reliance on a luminometer limits system portability and requires trained personnel for data acquisition, processing, and interpretation. To address this limitation and advance toward a true point-of-need analytical system, the assay was implemented in a lab-on-chip format integrating a microfluidic chip with a photosensor array (a-Si:H). Furthermore, the feasibility of coupling the test with smartphone-based detection was demonstrated. Compared to previously reported type III CRISPR-Cas nucleic acid detection methods, the developed test represents an advancement in portable CRISPR-Cas analytical platforms. Although demonstrated here for 4.5 target RNA quantification, the assay can, in principle, be extended to other RNA sequences simply by replacing the crRNA. Future integration with paper-based supports could further enhance the sustainability of the platform. Furthermore, a comprehensive evaluation of matrix effects (e.g., serum, saliva, and wastewater) has yet to be performed. Addressing these interferences constitutes a crucial objective for the next stage of this research.

## 5.5 Acknowledgements

This research was supported by the NanoImmunoEra project that has received funding from the European Union's MSCA Staff exchange Horizon Europe programme Grant Agreement Number 101086341.

## 5.6 References

[1] S. H. Sternberg, H. Richter, E. Charpentier, and U. Qimron, "Adaptation in CRISPR-Cas Systems," *Mol Cell*, vol. 61, no. 6, pp. 797–808, Mar. 2016, doi: 10.1016/J.MOLCEL.2016.01.030.

[2] G. Faure, K. S. Makarova, and E. V. Koonin, "CRISPR–Cas: Complex Functional Networks and Multiple Roles beyond Adaptive Immunity," *J Mol Biol*, vol. 431, no. 1, pp. 3–20, Jan. 2019, doi: 10.1016/J.JMB.2018.08.030.

[3] A. Kumaran *et al.*, "Advancements in CRISPR-Based Biosensing for Next-Gen Point of Care Diagnostic Application," *Biosensors 2023, Vol. 13, Page 202*, vol. 13, no. 2, p. 202, Jan. 2023, doi: 10.3390/BIOS13020202.

[4] C. C.; Liu, Y. Dai, C. C. Liu, and Y. Dai, "Application of CRISPR Cas Systems for Biosensing," *Biosensors 2023, Vol. 13, Page 672*, vol. 13, no. 7, p. 672, Jun. 2023, doi: 10.3390/BIOS13070672.

[5] J. E. van Dongen and L. I. Segerink, "Building the Future of Clinical Diagnostics: An Analysis of Potential Benefits and Current Barriers in CRISPR/Cas Diagnostics," *ACS Synth Biol*, vol. 14, no. 2, pp. 323–331, Feb. 2025, doi: 10.1021/ACSSYNBIO.4C00816/ASSET/IMAGES/LARGE/SB4C00816_0004.JPEG.

[6] Z. Shang *et al.*, "Systematically Investigating CRISPR/Cas12a Fluorescent Biosensor for Sensitive and Specific Single Nucleotide Variants Detection," *J Fluoresc*, pp. 1–9, May 2025, doi: 10.1007/S10895-025-04360-5/FIGURES/5.

[7] Z. Huang, J. Fang, M. Zhou, Z. Gong, and T. Xiang, "CRISPR-Cas13: A new technology for the rapid detection of pathogenic microorganisms," *Front Microbiol*, vol. 13, p. 1011399, Oct. 2022, doi: 10.3389/FMICB.2022.1011399/XML.

[8] J. Carte, R. Wang, H. Li, R. M. Terns, and M. P. Terns, "Cas6 is an endoribonuclease that generates guide RNAs for invader defense in prokaryotes," *Genes Dev*, vol. 22, no. 24, pp. 3489–3496, Dec. 2008, doi: 10.1101/GAD.1742908,.

[9] J. K. Nuñez, A. S. Y. Lee, A. Engelman, and J. A. Doudna, "Integrase-mediated spacer acquisition during CRISPR-Cas adaptive immunity," *Nature*, vol. 519, no. 7542, pp. 193–198, Mar. 2015, doi: 10.1038/NATURE14237,.

[10] J. K. Nuñez, L. B. Harrington, P. J. Kranzusch, A. N. Engelman, and J. A. Doudna, "Foreign DNA capture during CRISPR-Cas adaptive immunity," *Nature*, vol. 527, no. 7579, pp. 535–538, Nov. 2015, doi: 10.1038/NATURE15760,.

[11] L. Deng, R. A. Garrett, S. A. Shah, X. Peng, and Q. She, "A novel interference mechanism by a type IIIB CRISPR-Cmr module in Sulfolobus," *Mol Microbiol*, vol. 87, no. 5, pp. 1088–1099, Mar. 2013, doi: 10.1111/MMI.12152;WGROUP:STRING:PUBLICATION.

[12] P. Samai, N. Pyenson, W. Jiang, G. W. Goldberg, A. Hatoum-Aslan, and L. A. Marraffini, "Co-transcriptional DNA and RNA cleavage during type III CRISPR-cas immunity," *Cell*, vol. 161, no. 5, pp. 1164–1174, May 2015, doi: 10.1016/j.cell.2015.04.027.

[13] J. R. Elmore *et al.*, "Bipartite recognition of target RNAs activates DNA cleavage by the Type III-B CRISPR–Cas system," *Genes Dev*, vol. 30, no. 4, pp. 447–459, Feb. 2016, doi: 10.1101/GAD.272153.115,.

[14] M. A. Estrella, F. T. Kuo, and S. Bailey, “RNA-activated DNA cleavage by the Type III-B CRISPR–Cas effector complex,” *Genes Dev*, vol. 30, no. 4, pp. 460–470, Feb. 2016, doi: 10.1101/GAD.273722.115,.

[15] M. Kazlauskiene, G. Tamulaitis, G. Kostiuk, Č. Venclovas, and V. Siksnys, “Spatiotemporal Control of Type III-A CRISPR-Cas Immunity: Coupling DNA Degradation with the Target RNA Recognition,” *Mol Cell*, vol. 62, no. 2, pp. 295–306, Apr. 2016, doi: 10.1016/j.molcel.2016.03.024.

[16] W. Han *et al.*, “A type III-B CRISPR-Cas effector complex mediating massive target DNA destruction,” *Nucleic Acids Res*, vol. 45, no. 4, pp. 1983–1993, Feb. 2017, doi: 10.1093/NAR/GKW1274,.

[17] C. R. Hale, A. Cocozaki, H. Li, R. M. Terns, and M. P. Terns, “Target RNA capture and cleavage by the Cmr type III-B CRISPR–Cas effector complex,” *Genes Dev*, vol. 28, no. 21, p. 2432, Nov. 2014, doi: 10.1101/GAD.250712.114.

[18] R. H. J. Staals *et al.*, “RNA Targeting by the Type III-A CRISPR-Cas Csm Complex of Thermus thermophilus,” *Mol Cell*, vol. 56, no. 4, pp. 518–530, Nov. 2014, doi: 10.1016/j.molcel.2014.10.005.

[19] L. You *et al.*, “Structure Studies of the CRISPR-Csm Complex Reveal Mechanism of Co-transcriptional Interference,” *Cell*, vol. 176, no. 1–2, pp. 239-253.e16, Jan. 2019, doi: 10.1016/j.cell.2018.10.052.

[20] O. Niewoehner *et al.*, “Type III CRISPR–Cas systems produce cyclic oligoadenylate second messengers,” *Nature 2017 548:7669*, vol. 548, no. 7669, pp. 543–548, Jul. 2017, doi: 10.1038/nature23467.

[21] K. S. Makarova, V. Anantharaman, N. V. Grishin, E. V. Koonin, and L. Aravind, “CARF and WYL domains: Ligand-binding regulators of prokaryotic defense systems,” *Front Genet*, vol. 5, no. APR, 2014, doi: 10.3389/FGENE.2014.00102,.

[22] J. S. Athukoralage, S. Graham, S. Grüschow, C. Rouillon, and M. F. White, “A Type III CRISPR Ancillary Ribonuclease Degrades Its Cyclic Oligoadenylate Activator,” *J Mol Biol*, vol. 431, no. 15, pp. 2894–2899, Jul. 2019, doi: 10.1016/j.jmb.2019.04.041.

[23] J. S. Athukoralage, S. Graham, C. Rouillon, S. Grüschow, C. M. Czekster, and M. F. White, “The dynamic interplay of host and viral enzymes in type iii crispr-mediated cyclic nucleotide signalling,” *Elife*, vol. 9, Apr. 2020, doi: 10.7554/ELIFE.55852,.

[24] A. Nemudraia *et al.*, “Sequence-specific capture and concentration of viral RNA by type III CRISPR system enhances diagnostic,” *Nature Communications 2022 13:1*, vol. 13, no. 1, pp. 1–12, Dec. 2022, doi: 10.1038/s41467-022-35445-5.

[25] A. Santiago-Frangos *et al.*, “Intrinsic signal amplification by type III CRISPR-Cas systems provides a sequence-specific SARS-CoV-2 diagnostic,” *Cell Rep Med*, vol. 2, no. 6, Jun. 2021, doi: 10.1016/j.xcrm.2021.100319.

[26] S. N. Zakiyyah *et al.*, “CRISPR-Cas13a-powered electrochemical biosensors for RNA-based disease diagnostic and monitoring,” *Sensors and Actuators Reports*, vol. 10, p. 100358, Dec. 2025, doi: 10.1016/J.SNR.2025.100358.

[27] J. A. Steens *et al.*, “SCOPE enables type III CRISPR-Cas diagnostics using flexible targeting and stringent CARF ribonuclease activation,” *Nature Communications 2021 12:1*, vol. 12, no. 1, pp. 1–12, Aug. 2021, doi: 10.1038/s41467-021-25337-5.

[28] A. Ghouneimy, A. Mahas, T. Marsic, R. Aman, and M. Mahfouz, “CRISPR-Based Diagnostics: Challenges and Potential Solutions toward Point-of-Care Applications,” *ACS Synth Biol*, vol. 12, no. 1, p. 1, Jan. 2022, doi: 10.1021/ACSSYNBIO.2C00496.

[29] A. Roda and M. Guardigli, “Analytical chemiluminescence and bioluminescence: Latest achievements and new horizons,” *Anal Bioanal Chem*, vol. 402, no. 1, pp. 69–76, Jan. 2012, doi: 10.1007/S00216-011-5455-8/FIGURES/3.

[30] M. C. Dell’Oca *et al.*, “Spotlight on G-Quadruplexes: From Structure and Modulation to Physiological and Pathological Roles,” *Int J Mol Sci*, vol. 25, no. 6, Mar. 2024, doi: 10.3390/IJMS25063162,.

[31] W. Li *et al.*, “Insight into G-quadruplex-hemin DNAzyme/RNAzyme: adjacent adenine as the intramolecular species for remarkable enhancement of enzymatic activity,” *Nucleic Acids Res*, vol. 44, no. 15, pp. 7373–7384, Sep. 2016, doi: 10.1093/NAR/GKW634.

[32] X. Mao *et al.*, “Activity modulation and allosteric control of a scaffolded DNAzyme using a dynamic DNA nanostructure,” *Chem Sci*, vol. 7, no. 2, pp. 1200–1204, Jan. 2016, doi: 10.1039/C5SC03705K.

[33] I. Willner, B. Shlyahovsky, M. Zayats, and B. Willner, “DNAzymes for sensing, nanobiotechnology and logic gate applications,” *Chem Soc Rev*, vol. 37, no. 6, pp. 1153–1165, May 2008, doi: 10.1039/B718428J.

[34] T. Li, F. Lohmann, and M. Famulok, “Interlocked DNA nanostructures controlled by a reversible logic circuit,” *Nat Commun*, vol. 5, no. 1, pp. 1–8, Sep. 2014, doi: 10.1038/NCOMMS5940;TECHMETA=123;SUBJMETA=606,631,639,92,925,926;KWRD=COMPUTATIONAL+CHEMISTRY,DNA+NANOTECHNOLOGY.

[35] F. Costantini *et al.*, “Biomolecular Monitoring Tool Based on Lab-on-Chip for Virus Detection,” *Biosensors (Basel)*, vol. 13, no. 5, p. 544, May 2023, doi: 10.3390/BIOS13050544/S1.

[36] D. M. F. Prazeres, J. P. Conde, V. Chu, and J. P. Conde, “Detection of Chemiluminescence Using an Amorphous Silicon Photodiode,” *IEEE Sens J*, vol. 7, no. 3, pp. 415–416, Mar. 2007, doi: 10.1109/JSEN.2006.890144.

[37] G. De Cesare, M. Gavesi, F. Palma, and B. Riccò, “A novel a-Si:H mechanical stress sensor,” *Thin Solid Films*, vol. 427, no. 1–2, pp. 191–195, Mar. 2003, doi: 10.1016/S0040-6090(02)01223-3.

[38] D. Knipp, P. G. Herzog, and H. Stiebig, “Stacked amorphous silicon color sensors,” *IEEE Trans Electron Devices*, vol. 49, no. 1, pp. 170–176, Jan. 2002, doi: 10.1109/16.974764.

[39] D. Caputo, G. De Cesare, C. Fanelli, A. Nascetti, A. Ricelli, and R. Scipinotti, “Amorphous silicon photosensors for detection of ochratoxin a in wine,” *IEEE Sens J*, vol. 12, no. 8, pp. 2674–2679, 2012, doi: 10.1109/JSEN.2012.2198462.

[40] M. Mirasoli *et al.*, “Multiwell cartridge with integrated array of amorphous silicon photosensors for chemiluminescence detection: Development, characterization and comparison with cooled-CCD luminograph,” *Anal Bioanal Chem*, vol. 406, no. 23, pp. 5645–5656, Jun. 2014, doi: 10.1007/S00216-014-7971-9/FIGURES/8.

[41] X. Zhang *et al.*, “Impact of NH4+ on the catalytic activity of G-quadruplex/hemin DNAzyme for chemiluminescent sensing,” *Anal Bioanal Chem*, pp. 1–10, Apr. 2025, doi: 10.1007/S00216-025-05842-Y/TABLES/2.

# *Chapter 6*

***Borealis** - Biofilm Onboard Radiation Exposure Assessment Lab In Space*

---

## 6.1 Introduction

The BOREALIS mission (Biofilm Onboard Radiation Exposure Assessment Lab In Space) is an innovative 6U CubeSat project funded by the Italian Space Agency (ASI) within the ALCOR program. Developed through a collaboration between the University of Bologna's CIRI Aerospace, the School of Aerospace Engineering at Sapienza University of Rome, and Kayser Italia Srl, the mission aims to investigate the biological responses of microbial biofilms to the combined stressors of microgravity and ionizing radiation in orbit [1].

Microbial biofilms are sessile microbial communities embedded within an extracellular polymeric matrix, displaying emergent characteristics such as enhanced resilience to environmental stress, altered patterns of gene expression, and cooperative metabolic interactions [2]. These properties, often absent in planktonic cells, make biofilms particularly relevant for space biology. In spacecraft environments, biofilms can compromise crew health, promote biocontamination, and accelerate material degradation, while simultaneously offering promising avenues for biotechnological exploitation [3]. Understanding their adaptive mechanisms under extraterrestrial conditions is therefore critical both for mitigating mission risks and for exploring potential applications in long-term space exploration [4].

Recent biofilm experiments conducted aboard the International Space Station (ISS), such as the Space Biofilms Project and the ESA BIOFILMS experiment, have been essential in characterizing microbial growth in microgravity to ensure the safety of long-duration space missions. The Space Biofilms Project, which has included both bacterial (*Pseudomonas aeruginosa*) and fungal (*Penicillium rubens*) components, characterized changes in mass, thickness, and gene expression compared to Earth-based controls [5], [6]. Interestingly, studies on *P. aeruginosa* have shown that in microgravity, biofilms can develop unique structures, such as a "column-and-canopy" morphology, not typically seen on Earth [7]. Furthermore, researchers are actively testing mitigation strategies; one recent finding demonstrated that liquid-infused, textured surfaces were remarkably effective, reducing biofilm formation of *P. aeruginosa* by about 86% in space, performing even better than on Earth [8]. Other ongoing investigations, like the Polymicrobial Biofilm Growth and Control study, are focusing on the complex behavior of multi-species biofilms and the efficacy of various antimicrobial materials (like copper or silver-based disinfectants) to prevent corrosion and risks to astronaut health on critical systems [9], [10]. However, the ISS presents significant experimental limitations: the massive number of scientific experiments conducted on board severely restricts the time and resources available for microbiology research. Additionally, due to its low Earth orbit, the ISS only exposes experiments to relatively low levels of space radiation.

For this reason**,** using CubeSats (small, standardized satellites) is becoming an increasingly attractive and cost-effective option, as they can provide dedicated experimental platforms and reach orbits with higher radiation doses, making them highly valuable for advanced space microbiology studies [11].

The use of nanosatellite platforms for biological research has been progressively demonstrated in a series of pioneering missions (Table 6.1).

***Table 6.1.*** *Microorganisms employed in biological experiments previously conducted in CubeSat missions.*

| Mission | Organism(s) | Objective |
|---|---|---|
| **GeneSat-1** | *E. coli* (GFP) | Bacterial growth/metabolism with GFP |
| **PharmaSat** | *S. cerevisiae* | Yeast response to antifungal drug |
| **O/OREOS SESLO** | *B. subtilis* spores | Survival, germination, metabolic activity |
| **SporeSat** | *C. richardii* spores | Gravity effects on spore reproduction |
| **EcAMSat** | *E. coli* (WT & ΔrpoS) | Antibiotic response in microgravity |
| **BioSentinel** | *S. cerevisiae* | DNA damage response to deep-space radiation |

Among these, PharmaSat (NASA Ames, 2009) [12], a 3U CubeSat, investigated yeast cell responses to antifungal treatments in microgravity, providing one of the first demonstrations of in-orbit pharmacological testing. SporeSat (NASA Ames, 2014) [13], also a 3U CubeSat, employed *Ceratopteris richardii* spores as biological sensors to study the role of gravity perception and calcium signaling in plant cells. More recently, BioSentinel [14], a 6U CubeSat launched in 2022 aboard Artemis I, was designed to assess the long-term biological impact of deep-space radiation on *Saccharomyces cerevisiae*. Collectively, these missions established CubeSats as viable platforms for autonomous biological experimentation. Within this context, BOREALIS constitutes a novel step forward, as the first CubeSat specifically dedicated to investigating microbial biofilms under combined microgravity and radiation stress, supported by real-time *in situ* imaging.

BOREALIS is equipped with a miniaturized lab-on-chip payload integrated with a miniaturized microscope, enabling real-time monitoring of genetically engineered microorganisms cultivated in biofilm form.

Its mission profile features dual-phase orbital operations: an initial phase in Low Earth Orbit (LEO), at approximately 700 km of altitude, to evaluate microgravity-driven effects, followed by operations in Medium Earth Orbit (MEO), at approximately 2000 km, to investigate responses under increased ionizing radiation. This dual-orbit design allows the decoupling of environmental stressors while simultaneously serving as a technological demonstration of complex orbital maneuvers executed by a nanosatellite platform (Figure 6.1).

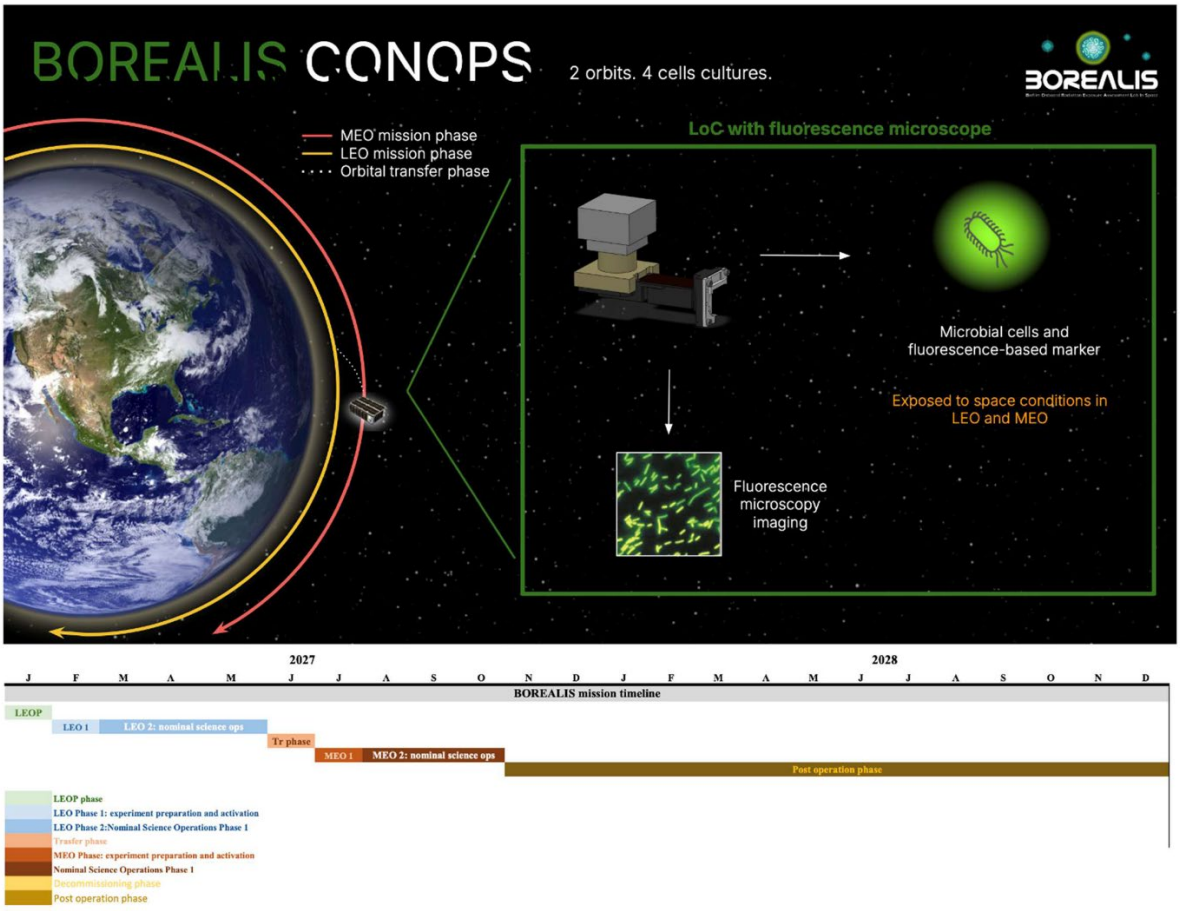


***Figure 6.1**. BOREALIS CONOPS. Reprinted from NARDI, Lorenzo, et al. "Integrating Model-Based Systems Engineering into CubeSat development: a case study of the BOREALIS mission.", Aerospace, 2025, 12.3: 256, published by MDPI, Basel, Switzerland, under the Creative Commons Attribution (CC BY 4.0) license.*

Adopting a lab-on-chip as the main payload offers clear benefits, such as reduced sample needs, faster analysis, and greater efficiency through automation. While these systems are well established in biomedical research on Earth, their application in space has only recently expanded [15]. Notable milestones include NASA's LOCAD-PTS tested on the ISS in 2006, the MinION sequencer flown between 2016 and 2017, and the "IN SITU Bioanalysis" project, which enabled cortisol

monitoring in orbit. More recently, the AstroBio CubeSat (ABCS) launched in 2022, successfully demonstrated chemiluminescence-based technologies, laying the foundation for future integrated systems supporting the BOREALIS payload [16].

Our laboratory covers part of the biological perspective of the BOREALIS project, pursuing three primary objectives:

- To characterize bacterial biofilm growth and structural adaptation under the simultaneous influence of microgravity and ionizing radiation;
- To evaluate radioprotective strategies, including both passive shielding and pharmacological countermeasures such as melanin-based nanoparticles;
- To investigate the generation and biological impact of secondary radiation particles produced by cosmic ray interactions with spacecraft materials.

Ultimately, BOREALIS is expected to advance current knowledge on microbial adaptation to extraterrestrial environments, inform the development of effective countermeasures against biofilm-associated risks, and broaden the role of CubeSats as autonomous laboratories for space biology. Its results will not only address fundamental biological questions but also contribute to the safe and sustainable realization of long-duration human missions to the Moon, Mars, and beyond.

Currently, the BOREALIS project is in the phases A/B of the CubeSat mission, in which feasibility of our proposed approach is to be demonstrated by developing a breadboard of the payload and executing biofilm formation and observeation experiments on it.

The activity described herein concerns the development of analytical protocols for biofilm formation in microfluidic format and the provision of inputs for the payload breadboard design.

## 6.2 Materials and methods

### 6.2.1 Bacterial strains

For the biological component of the BOREALIS mission, two microbial models were selected: *Escherichia coli BL21 (DE3)* and *Pseudomonas aeruginosa (Schroeter) Migula 10145* ™, representing respectively a probiotic and a pathogenic organism.

*E. coli* was chosen as a probiotic model system. Its use is supported by clinical evidence demonstrating relevant health-promoting properties [17]. In particular, randomized, controlled, double-blind trials on human subjects have shown that *E. coli*-based probiotics can reduce symptoms

associated with constipation and inflammatory bowel disease. Moreover, their administration has proven to be equally effective as mesalazine in preventing relapse in patients with ulcerative colitis [18]. The availability of such data makes *E. coli* a well-characterized and safe organism, suitable for inclusion in biological payloads intended to address host-microbe interactions and microbial resilience in space environments.

Conversely*, P. aeruginosa* was selected as a pathogenic model organism, primarily because of its clinical importance and its pronounced ability to form biofilms. *P. aeruginosa* is currently recognized as one of the most threatening bacterial species worldwide, not only due to the increasing prevalence of multidrug-resistant strains but also because of its diverse repertoire of virulence traits that aggravate infection outcomes [19]. A key factor in its pathogenicity is its capacity to develop biofilms, which provide physical and biochemical protection from antimicrobial agents and host immune responses, thereby contributing to chronic and persistent infections in immunocompromised individuals. Importantly, *P. aeruginosa* biofilm formation has been repeatedly documented in spaceflight conditions, including on the International Space Station, demonstrating a marked propensity to establish structured biofilms [20]. While no CubeSat mission to date has directly employed *P. aeruginosa*, the accumulated evidence highlights its relevance as a spaceflight microbial model.

Based on these considerations, the BOREALIS mission employs both *E. coli* and *P. aeruginosa* to explore the contrasting behaviors of a probiotic and a pathogenic species under space conditions.

*Escherichia coli BL21 (DE3)* was engineered with the red-emitting protein (mCherry), whereas commercial *Pseudomonas aeruginosa (Schroeter) Migula 10145GFP* ™ shows a costituive expression of the green fluorescence protein (GFPmut3). Figure 6.2 illustrates the plasmids carried by the two bacterial strains, which express distinct fluorescent proteins. Notably, both plasmids confer resistance to ampicillin, important for ensuring continuous expression of the fluorescent proteins.

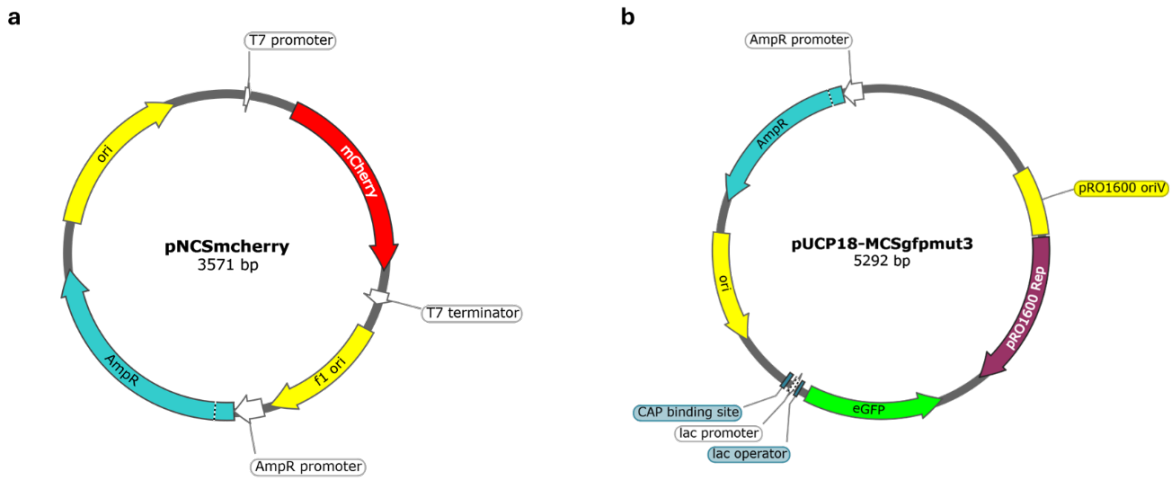


***Figure 6.2.*** *(a) Plasmid for mCherry expression in E. coli BL21, and (b) plasmid for GFPmut3 expression in P. aeruginosa.*

Green fluorescent proteins (GFPs) have become indispensable tools in molecular and cellular biology. The first GFP was identified in 1962 in the jellyfish *Aequorea victoria* by Osamu Shimomura [21]. The fluorescence originates from an intrinsic chromophore, formed by cyclization of residues Ser65, Tyr66, and Gly67, together with dehydrogenation of Tyr66 [22]. Its maturation requires only molecular oxygen. Spectroscopic studies revealed that wild-type GFP (wtGFP) shows two main absorption bands: one at 397 nm (neutral chromophore) and a weaker one at 470 nm (anionic form). In both cases, emission occurs at 504 nm, consistent with an excited-state proton transfer [23].

To improve folding efficiency and optical properties, numerous GFP variants have been generated by mutagenesis. Among them, GFPmut3 was selected to be used in the BOREALIS activities. Published in 1996 and derived from *Aequorea victoria*, GFPmut3 is a rapidly maturing, weakly dimeric variant carrying two substitutions (S65G, S72A). These mutations enhance folding efficiency at 37 °C, leading to stronger fluorescence, higher expression levels and solubility [24]. GFPmut3 absorbs maximally at 501 nm and emits at 511 nm (Table 6.2, Figure 6.3a).

To complement GFPmut3 with a spectrally distinct marker, mCherry was chosen. This red fluorescent protein, published in 2004 and derived from *Discosoma sp.*, is a rapidly maturing monomer with low acid sensitivity [25]. Its absorption and emission maxima are 587 nm and 610 nm, respectively, providing a robust red-shifted signal that pairs well with eGFP (Table 6.2, Figure 6.3b).

*Table 6.2. Fluorescence characteristics of the selected proteins.*

| Protein | Excitation (nm) | Emission (nm) | Ext. coeff. ($M^{-1}cm^{-1}$) | QY | Brightness |
|---|---|---|---|---|---|
| **eGFP** | 501 | 511 | 39000 | 0.60 | 23.0 |
| **mCherry** | 587 | 610 | 72000 | 0.22 | 15.8 |

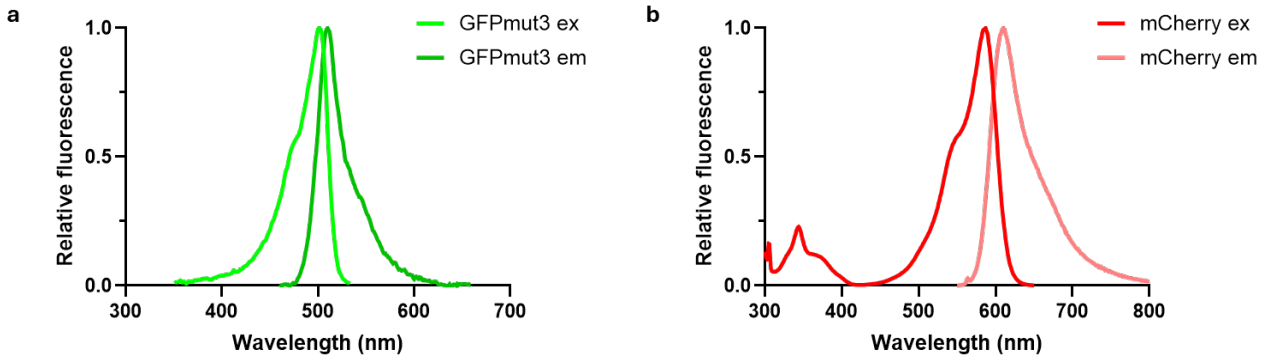


*Figure 6.3. Fluorescence spectra of the proteins (a) GFPmut3 and (b) mCherry.*

### 6.2.2 Microorganism long-term conservation

Various biological CubeSats have been developed and launched by NASA. Among them, GeneSat-1, PharmaSat, O/OREOS SESLO, SporeSat, EcAMSat, and BioSentinel used live microorganisms to perform science investigations in space.

One of the crucial aspects for successful scientific outcome of the mission is to long-term preserve cells viability, during satellite integration and pre-experiment mission phases. To reach this goal, several approaches have been employed (Table 6.3).

***Table 6.3.*** *Conservation strategies in previously conducted CubeSat experiments.*

| Mission | Organism | Conservation | Key Result |
|---|---|---|---|
| **GeneSat-1** | *E. coli* | 10 °C in PBS buffer | Slower growth |
| **PharmaSat** | *S. cerevisiae* | 6–16 °C | Slower growth |
| **O/OREOS** | *B. subtilis* | Desiccated (14–97 days) | Slower/abnormal after long-term |
| **SporeSat** | Fern spores | — | Activation failed |
| **EcAMSat** | *E. coli* | Stasis buffer (8 weeks) | Successful reactivation |
| **BioSentinel** | *S. cerevisiae* | Desiccated (15–21 months) | No reactivation |

In preparation for the BOREALIS mission, protocols were optimized for the long-term conservation of *E. coli* and *P. aeruginosa* on agar-based media in the form of small tablets. The optimized procedure is outlined below.

Bacterial cultures were first grown overnight at 37 °C under shaking, using LB (Luria-Bertani) addictioned with ampicillin (300 μg $mL^{-1}$) medium. Subsequently, 50 μL of undiluted culture, optical density at 600 nm ($OD_{600}$) of 2.0 were dispensed and spread onto agar plates and then incubated overnight at 37°C to promote a thin film formation, covering the agar surface completely (Figure 6.4a). On the following day, plates were dried under sterile laminar airflow for 24 h and then stored at room temperature in the dark. To verify bacterial viability after desiccation, a small tablet (4 mm diameter) (Figure 6.4b) with the surface-dried bacterial cells, identical to those later used as cell reservoirs in the mission payload, was removed and inoculated into fresh medium. The culture was incubated overnight at 37°C with vigorous agitation, and optical density was measured the next day to confirm bacterial growth. The same verifying procedure was followed two times per month in order to evaluate long-term bacterial viability in this dessicated format (Figure 6.4c).

This drying method is simple, rapid, and does not require vacuum pumps. Moreover, it is adaptable to any type or size of support, since the agar medium can be poured into different formats. The resulting desiccated agar with surface-attached cells had a thickness of approximately 0.7 – 0.8 mm and conserved the cell viability for at least nine months. The long-term conservation of bacteria on agarized medium offers several advantages. It eliminates the need to maintain cells at low temperature, which is particularly critical during the integration and launch phases of the mission when no active temperature control is available for the CubeSat. It also removes the requirement to keep dehydrated cells at extremely low humidity, a condition that proved difficult to control during preliminary tests with trehalose-assisted lyophilization.

Given the variability observed in long-term viability under these conditions, the agar tablet format was ultimately adopted as a more reliable and robust preservation strategy for spaceflight applications.

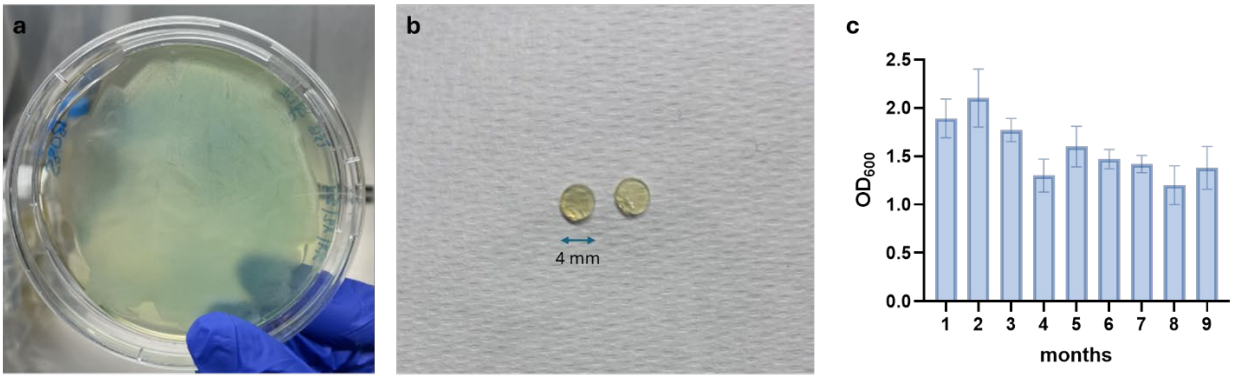


***Figure 6.4.*** *(a) Dried bacteria on agar support, (b) tablets to be used in the microfluidic device as cell reservoir, and (c) overnight $OD_{600}$ measurements showing long-term viability of bacterial cells on agar tablets over nine months.*

### 6.2.3 Microorganism Reactivation

The experiment involves rehydrating the bacterial cells from the tablet using liquid LB medium with ampicillin. This liquid medium provides a suitable environment for cell recovery, allowing the bacteria to resume growth and reach sufficient density to begin biofilm formation once in the microfluidic chip. The stability of ampicillin in liquid LB medium was evaluated over a period of nine months (compatible with the mission timeline), with the medium stored both at room temperature and at 4°C to simulate conditions that could be encountered during the entire space mission. As shown in Figure 6.5, the antibiotic-containing medium was tested by inoculating both ampicillin-resistant and wild-type bacteria (without antibiotic resistance), and growth was assessed via overnight $OD_{600}$ measurements. The results indicate that ampicillin remains stable in solution and effectively kills the non-resistant bacteria over the testing period. It is also observed that at 4°C the stability is slightly better, although overall it is comparable to that at room temperature. These findings confirm that the medium remains stable and suitable for storage at different temperatures.

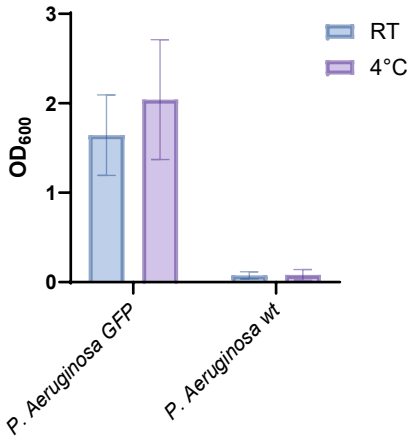


***Figure 6.5.*** *Average $OD_{600}$ of ampicillin-resistant and wild-type cells inoculated once per month over nine months in LB medium with ampicillin stored at room temperature (RT) and 4°C.*

The influence of oxygen was also examined. While bacteria can form biofilms in low-oxygen environments, the chromophore of the fluorescent protein does not mature in the absence of oxygen, preventing fluorescence [26]. Fluorescence microscopy clearly showed that only a small fraction of cells were able to express GFP correctly during the experiment, which was further confirmed by fluorescence analysis of the recirculating medium, yielding extremely low values. (Figure 6.6a). This issue was addressed by designing a container for the liquid nutrient medium with a gas-permeable membrane (Breathe-Easy® sealing membrane, Sigma-Aldrich), allowing efficient oxygenation through exchange with the external environment (Figure 6.6b). Produced via 3D printing, the container features a frame with its two faces formed by the gas-permeable membrane, providing a large surface area for efficient oxygen exchange to support chromophore maturation and biofilm formation (Figure 6.6c).

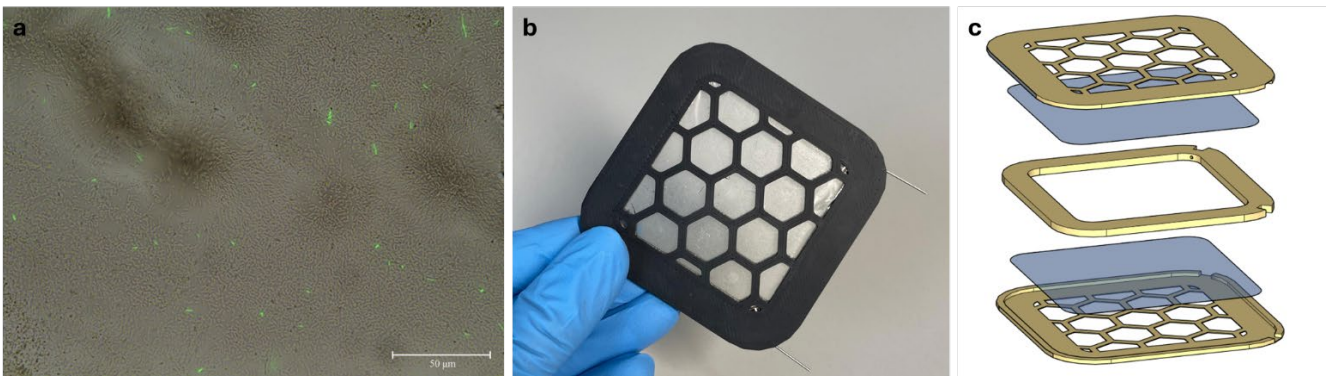


***Figure 6.6.*** *(a) Merged image showing biofilm and GFP expression under oxygen-limited conditions, (b) 3D-printed medium container with the gas-permeable membrane and, (c) exploded model of the nutrient reservoir.*

### 6.2.4 Biofilm formation under flow

Biofilms were cultivated under flow conditions to more accurately replicate the dynamic environments encountered by bacteria in natural and host-associated systems. Flow facilitates continuous nutrient supply, efficient waste removal, and the establishment of spatial concentration gradients, while modulating bacterial motility, adhesion, extracellular polymeric substance production, and quorum sensing. Microfluidic platforms enable precise microscale control of these parameters, allowing high-throughput, reproducible, and real-time analysis of biofilm development, structure, and dispersal [27]. Biofilm formation typically comprises several stages: (1) reversible attachment, (2) irreversible attachment, (3) maturation, and (4) dispersal (Figure 6.7). The transition from reversible to irreversible attachment is achieved when planktonic bacteria closely approach a surface and withstand the shear forces exerted by the flow. This approach thus provides a physiologically relevant and experimentally versatile model, superior to static culture conditions.

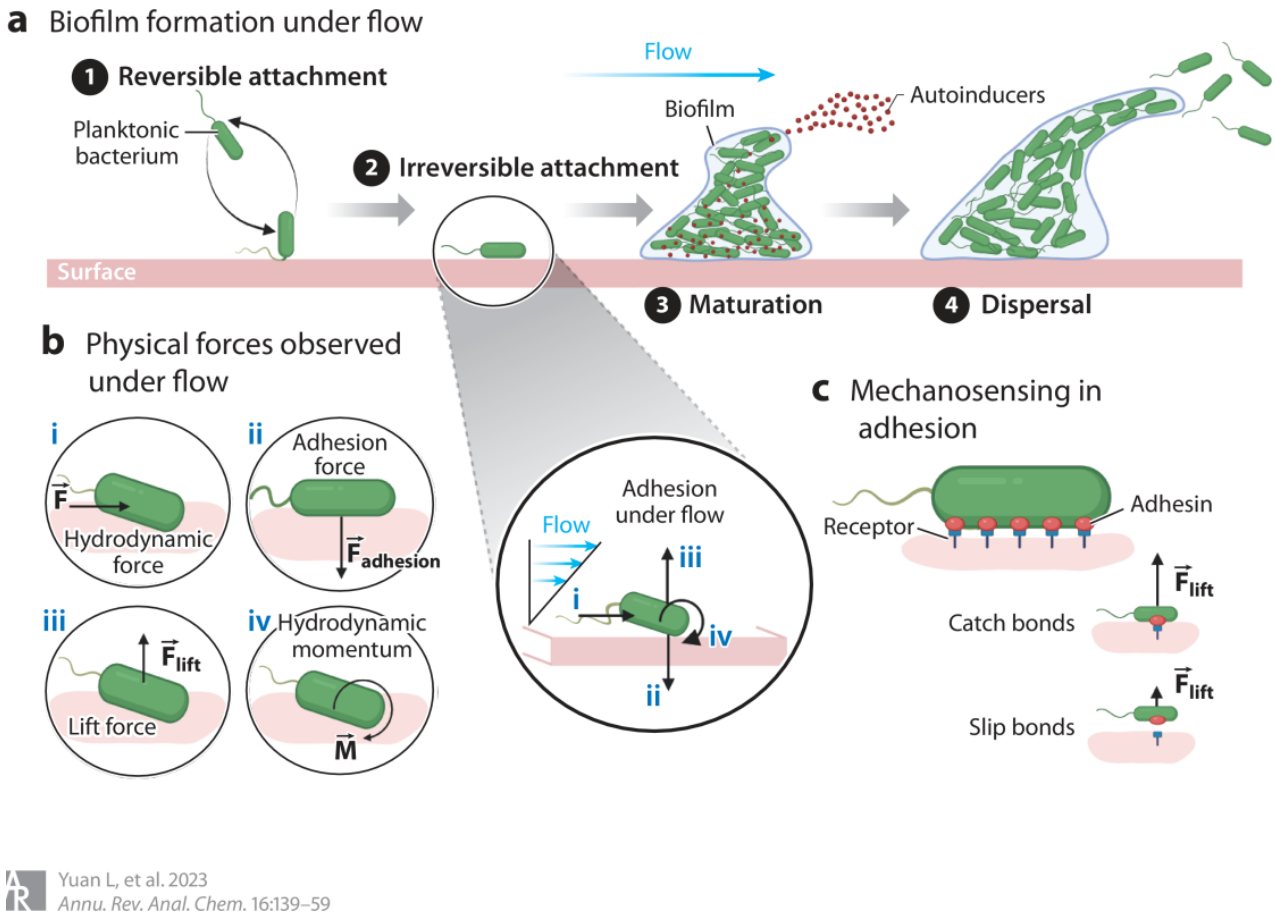


Yuan L, et al. 2023
*Annu. Rev. Anal. Chem.* 16:139–59

***Figure 6.7****. Schematic of biofilm formation under flow. Biofilm development involves reversible and irreversible attachment, maturation, and dispersal. Flow generates hydrodynamic forces that challenge surface adhesion, which bacteria resist using adhesins and flagella. Adapted from Yuan et al., Microfluidics for Biofilm Studies, Annual Review of Analytical Chemistry, 2023, under CC BY 4.0.*

### 6.2.5 Microfluidic system

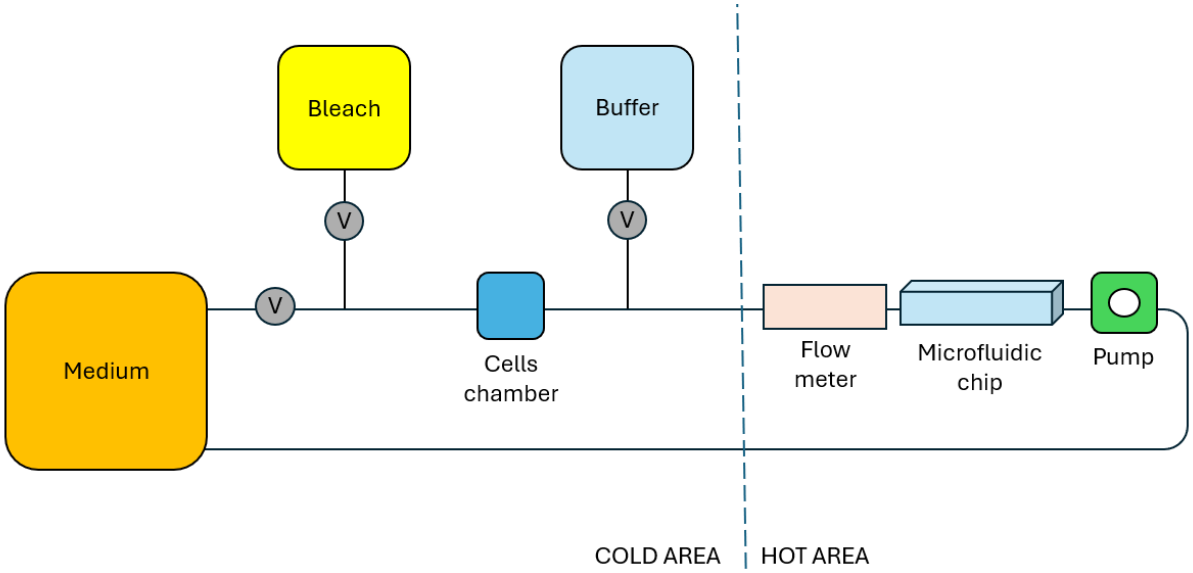


***Figure 6.8.*** *Schematic representation of the microfluidic system.*

Figure 6.8 depicts the microfluidic architecture designed for biofilm cultivation within the CubeSat. A reservoir containing LB medium supplemented with ampicillin is integrated with a gas-permeable membrane to ensure adequate oxygenation. Two additional reservoirs are incorporated: one containing commercial bleach, intended for chip sterilization upon completion of the experiment, and another containing phosphate buffer saline (PBS, 0.01 mol $L^{-1}$ pH 7.4), delivered to the chip prior to fluorescence measurements to avoid interference of planktonic cells above the biofilm. The inflow and outflow of these reservoirs are regulated by three valves, while a flow meter provides continuous monitoring of fluid dynamics within the system.

Upon activation of the miniaturized peristaltic pump, the nutrient medium is directed into a chamber housing an agar tablet with desiccated cells, thereby enabling their rehydration and resuspension. Following approximately two hours of incubation, the planktonic cells are transferred into the microfluidic chip and allowed to adhere to the channel walls for an additional two hours. Subsequently, medium recirculation is initiated at a controlled flow rate of 100 µL $min^{-1}$, thereby supporting biofilm development under flow conditions for a duration of 36 hours. The microfluidic chip is maintained within the temperature-controlled section of the system and supported by a heater adjustable to 37 °C to promote biofilm growth, while the cell chamber is independently supported by a separate heater, also adjustable to 37 °C, to sustain bacterial rehydration during the experiment; the remaining components of the system are not subjected to heating.

Figure 6.9 shows the microfluidic setup developed in the laboratory for conducting all biofilm formation experiments. The system consists of a microfluidic chip connected to the small bacterial sample chamber maintained at 37 °C inside a portable incubator. It also includes a gas-permeable cartridge containing the nutrient medium with the antibiotic, and a peristaltic pump operated by an electrically powered controller.

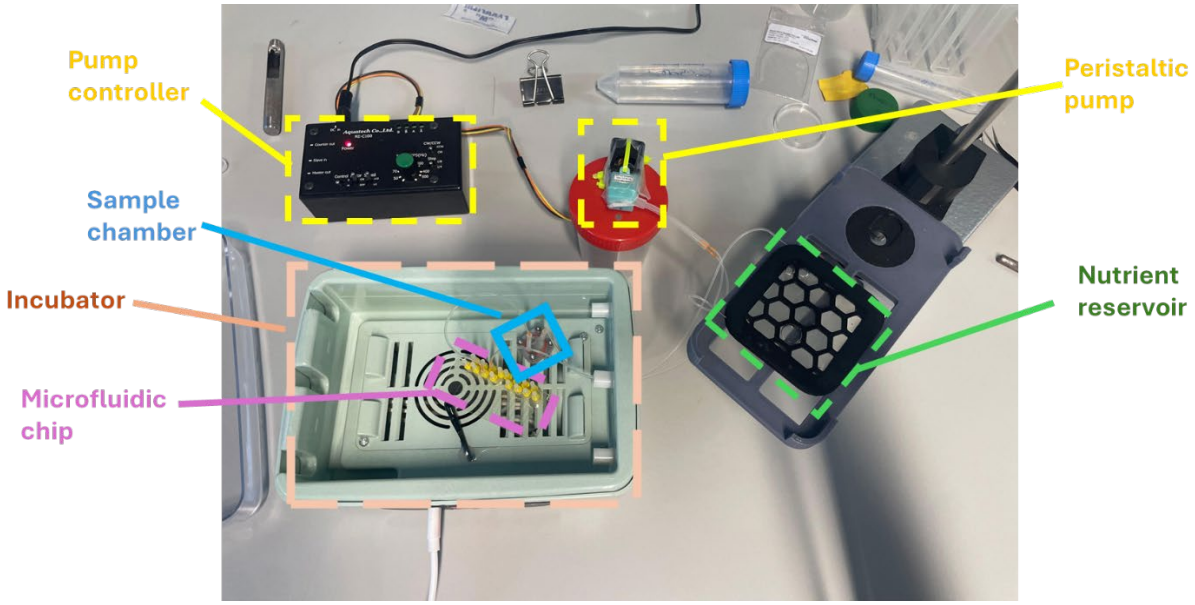


***Figure 6.9.*** *Microfluidic setup designed and assembled in the laboratory to conduct all biofilm formation assays.*

The microfluidic chip was manufactured according to the design published by Bourguignon, Natalia, et al., with modifications [28]. The design involves eight channels with one inlet and one outlet for each one (Figure 6.10a). The microchannel design has 20 µL as a total internal volume. The channel height is 150 µm, and curved wave channels were designed to avoid cells' accumulations in square corners and the formation of bubbles. Microfluidic chip channels are enclosed between an ibiTreat tissue culture-treated surface to promote bacterial adhesion and an ibidi Bioinert surface, which is chemically modified to prevent any form of cell adhesion, even after protein coating (https://ibidi.com/). This approach was chosen to promote biofilm growth on the side closest to the microscope, thereby optimizing image acquisition by minimizing the focal distance between the lens and the sample. The two surfaces exhibited markedly different properties as substrates for biofilm development.

As demonstrated in Figure 6.10b, the adhesion-treated surface retained crystal violet (CV) following staining, indicative of biofilm formation, whereas the cell-repellent surface showed no measurable retention of the dye.

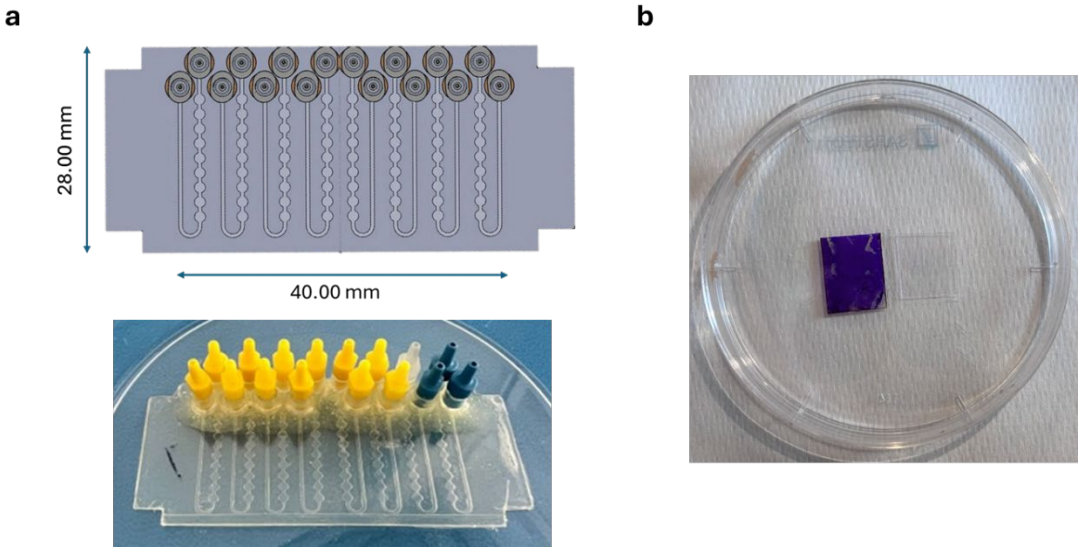


***Figura 6.10**. (a) Shows the microfluidic chip, while (b) show the CV staining for the adhesion-treated (left) and repellent (right) surfaces.*

## 6.3 Results and discussion

### 6.3.1 Optimization of experimental parameters

The results presented in this session refer only to *P. aeruginosa*, while the *E. coli* experiments are still ongoing.

In order to obtain the optimal biofilm within the microfluidic circuit, various growth parameters were optimised. Initially, different growth temperatures and times were tested to identify the most suitable ones applicable in the CubeSat. Only parameters compatible with the correct growth of microorganisms and the maturation of fluorescent proteins were selected. Among these, the best results were obtained by maintaining a temperature of 37°C for the entire duration of the experiment for a period of approximately 36 hours starting from the resuspension of the bacteria (Figure 6.11).

These parameters were optimized using the crystal violet (CV) staining assay, which enables quantitative assessment of bacterial biofilm formation [29], and by monitoring the fluorescence emission of bacteria within the biofilm.

The CV assay measures total biomass and is based on the ability of crystal violet dye to stain the cells and the extracellular polymeric substance (EPS) matrix of the biofilm whereas the use of fluorescence microscope (Nikon Eclipse C1, Nikon Corp., Tokyo, Japan) allows for the real-time observation and analysis of biofilm structure.

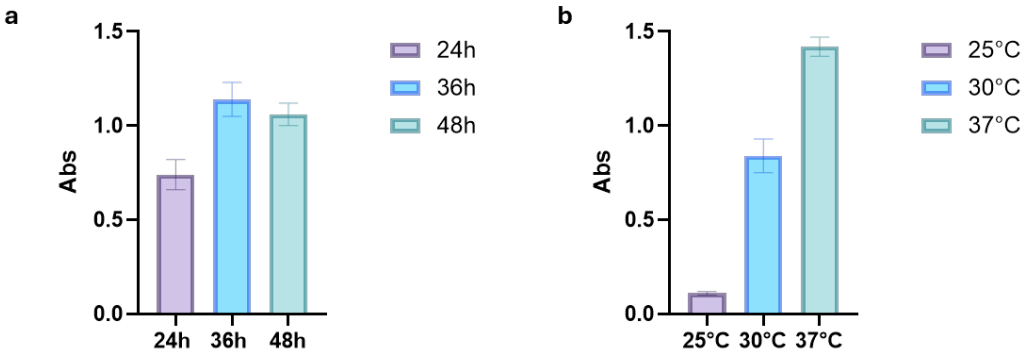


***Figure 6.11.*** *Absorbance values obtained with the crystal violet assay to assess P. aeruginosa biofilm growth as a function of (a) time and (b) temperature.*

### 6.3.2 Biofilm characterization

To assess the impact of hydrodynamic conditions on biofilm development, we compared growth under static conditions (Figure 6.12a) with growth in continuous flow (Figure 6.12b). Static cultures (flow rate of 0 µL $min^{-1}$), resulted in irregular and heterogeneous biofilm structures, with limited overall biomass accumulation. In contrast, biofilms cultivated under flow displayed markedly higher fluorescence intensity and more uniform coverage across the channel (Figures 6.12c and 6.12d). To demonstrate this, the fluorescence intensity along the dotted line spanning the full width of the well was analyzed. The resulting graph (Figure 6.12e), normalized for exposure time, further emphasizes the differences between the two conditions. In accordance with findings reported in the literature [28] and supported by our experimental results, we selected a flow rate of 100 µL $min^{-1}$ for subsequent experiments, as this condition consistently promoted both enhanced biomass accumulation and improved structural homogeneity compared to static growth.

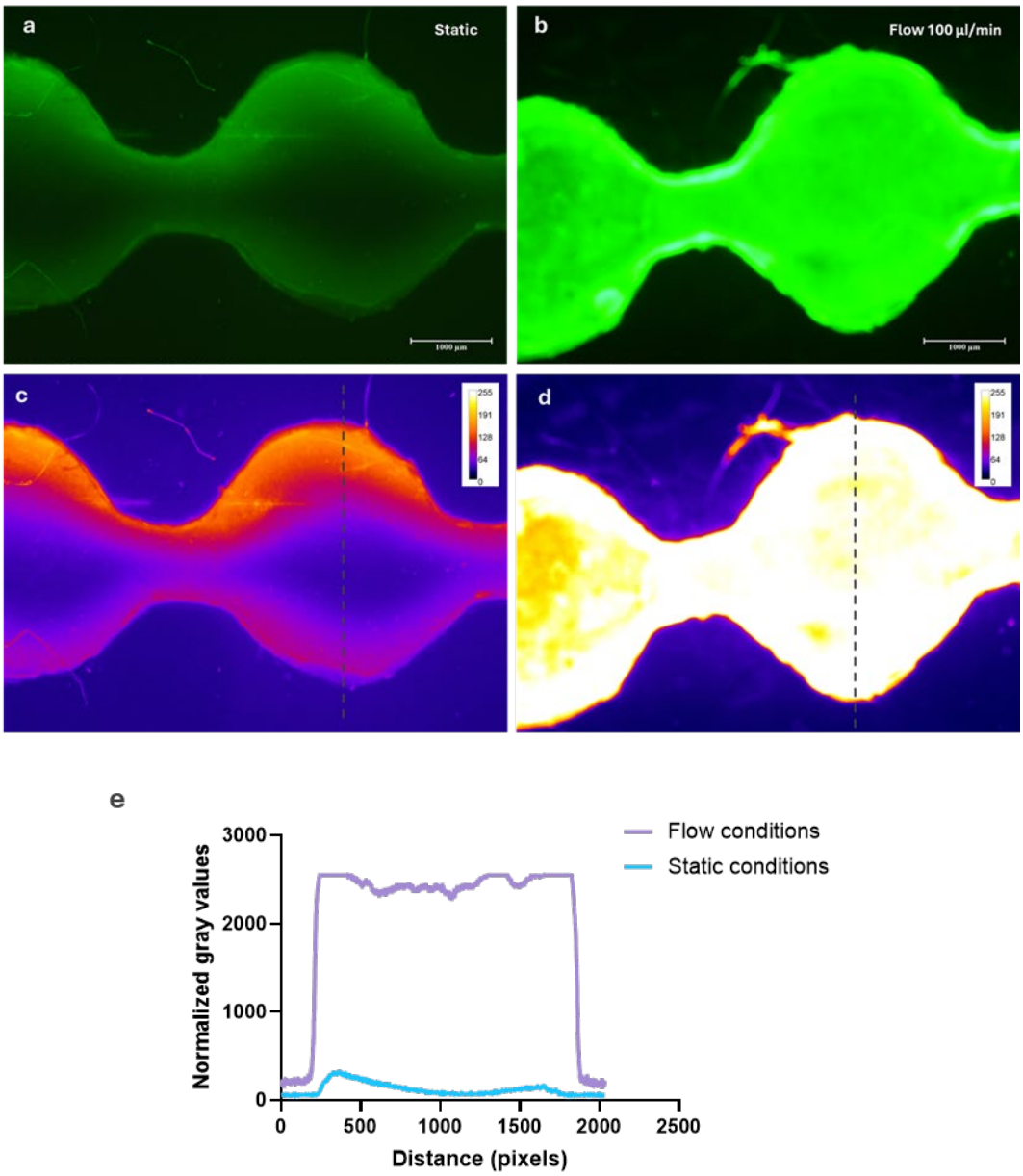


***Figure 6.12**. Fluorescence microscopy images of P. aeruginosa cells expressing GFP grown (a) under static conditions (4× magnification, 500 ms exposure time) and (b) under flow conditions (4× magnification, 100 ms exposure time). Panels (c) and (d) show the same fields as in (a) and (b), respectively, but emphasize the fluorescence intensity. The green channel was extracted from the original images, and a pseudo-colour scale was applied to visualise intensity variations. The intensity profile shown in graph (e) was obtained by analyzing the signal along the dotted line and normalizing it for the exposure times, highlighting the differences between the two conditions.*

The spatial distribution of the biomass was clearly shaped by the local hydrodynamic conditions: as shown in Figure 6.13b, in the lateral regions, where flow velocity was reduced, we observed a denser and more compact accumulation of cells forming thicker three-dimensional structures, demonstrated by an higher fluorescence intensity. In contrast, in the central portion of the channel, where the flow

was more uniform and exposed to higher shear stress, the biofilm appeared less developed, with thinner and more discontinuous pattern (Figure 6.13a). These observations indicate that velocity gradient generated by the channel geometry plays a key role in modulating biofilm architecture but, at the same time, in any cases, it enables us to obtain a homogeneous, consistent and reproducible biofilm.

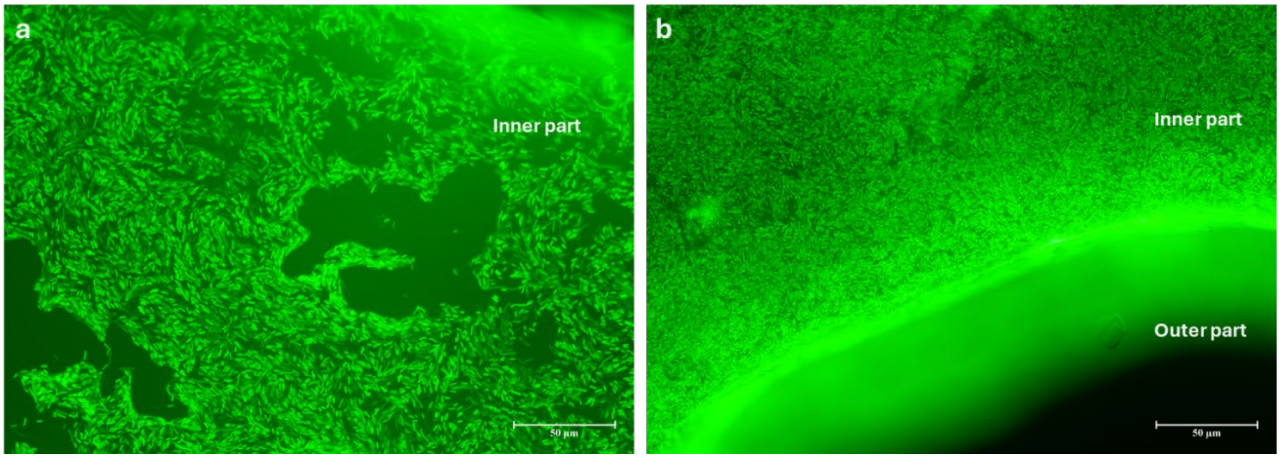


***Figure 6.13.*** *Fluorescence microscopy images of P. aeruginosa cells expressing GFP within the biofilm in the microfluidic channel. (a) Magnified view of the inner part of the channel (40× magnification, 10 ms exposure time) and (b) magnified view of the interface between the inner and outer parts of the channel (20× magnification, 10 ms exposure time). Excitation wavelength: 501 nm.*

### 6.3.3 Radioprotective melanin nanoparticles (NPs)

Melanin is a class of dark biopigments primarily responsible for photoprotection and pigmentation in living organisms [30]. Different types of melanin can be distinguished based on their origin and/or chemical precursor [31]. From a technological perspective, melanin can be extracted from natural sources, such as the ink of cuttlefish (*Sepia officinalis*). However, artificial melanin nanoparticles can also be synthesized in the laboratory. For instance, cuttlefish-derived melanin (*Sepia melanin*) exhibits properties analogous to those of polydopamine (PDA) nanoparticles (NPs) (Figures 6.14a and 6.14b) [32].

This project aims to evaluate the protective effect of PDA nanoparticles on bacteria exposed to the space environment. In the space environment, living organisms and materials are constantly exposed to a wide spectrum of radiation, including high-energy particles from cosmic rays and solar radiation [33]. Among these, ultraviolet (UV) radiation represents a major stress factor. While Earth's atmosphere effectively absorbs most harmful UV wavelengths, in space there is no protective shield, and UV-C radiation (100 – 280 nm) reaches its full intensity. UV-C is particularly damaging because

it induces direct DNA and RNA lesions, such as pyrimidine dimers, and promotes protein and membrane damage. For this reason, UV-C exposure in space is considered a critical challenge for microbial survival, material degradation, and the design of shielding technologies for spacecraft and habitats.

To test their impact throughout the entire duration of the experiment (from tablets to biofilm), PDA NPs [34], provided by Professor Montalti's group (Department of Chemistry "G. Ciamician – University of Bologna), were incorporated into the bacterial cultures. A concentration of 10 µg $mL^{-1}$ of PDA NPs was selected, expected to provide UV protection while minimizing oxidative stress. This choice aligns with prior studies demonstrating that low concentrations of these nanoparticles maintain cellular viability and antioxidant capacity [35], [36].

Briefly, a suspension of PDA NPs was added to an overnight bacterial culture ($OD_{600}$ = 2.0), thoroughly mixed, and subsequently spread onto agar plates. Following the previously described procedure, agar tablets containing the bacteria and PDA NPs were prepared for storage.

The protective effect of PDA nanoparticles (NPs) was assessed by exposing agar tablets to UV-C (254 nm) from a lamp emitting 1.63 mJ/s, placed 20 cm from the samples. Tablets were irradiated for 15, 30, and 45 minutes. As shown in Figure 6.14c, the presence of PDA NPs provided protection, preventing complete eradication of the bacterial cells after 45 min, whereas tablets without PDA NPs showed near-complete bacterial eradication. Notably, no significant differences were observed between 15 and 30 minutes of exposures, with or without PDA NPs, suggesting that the protective effect is evident only under prolonged irradiation. During the shorter exposures, bacteria likely survived due to the agar's protective effect: in low-water conditions, UVC generates few reactive oxygen species (ROS), and cells attached to the tablet surface are better shielded.

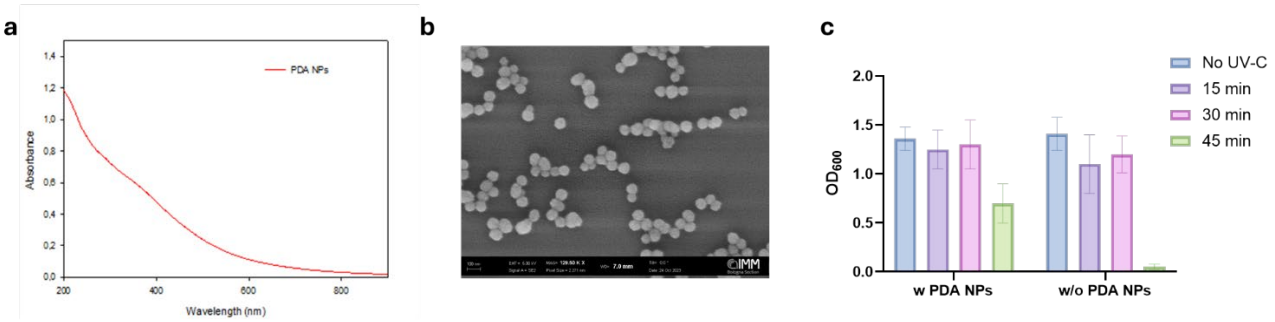


***Figure 6.14.*** *(a) Absorption spectrum and (b) SEM image of PDA NPs. (c) $OD_{600}$ of the overnight growth of the irradiated tablets.*

In summary, these preliminary results highlight the protective effect of PDA nanoparticles against UV-C irradiation on agar tablets with surface-attached *Pseudomonas aeruginosa* cells. However, further studies are needed to fully assess the impact of UV-C and to identify the optimal nanoparticles concentration for incorporation into the tablets. As this work is ongoing, definitive and fully reliable results are not yet available, but these findings provide a solid basis for future investigations.

## 6.4 Conclusions

All results presented so far were obtained using benchtop instrumentation. Specifically, biofilm development was monitored with a fluorescence detector, while total biomass was independently quantified through the crystal violet assay using a plate reader. For the sake of the project, the entire microfluidic system will be integrated within the CubeSat platform, where microbial biofilm formation detection will rely on two complementary approaches. The first is a portable fluorescence microscope, developed by Kayser Italia, positioned above the microfluidic chip and equipped with filters optimized for fluorescent proteins detection. The second is an array of amorphous silicon photosensors (a-Si:H), capable of converting incident light into an induced photocurrent, placed beneath the chip on the side opposite to the microscope. This dual-detection strategy is designed to provide both structural and quantitative information on biofilm growth under space-relevant conditions.

## 6.5 Acknowledgements

This research has received funding from Contract ASI No. 2024-2-I.0, Tender Identification Code (CIG) A0277F7460, Unique Project Code (CUP) F33C24000040005.

## 6.6 References

[1] L. Nardi *et al.*, “Integrating Model-Based Systems Engineering into CubeSat Development: A Case Study of the BOREALIS Mission,” *Aerospace 2025, Vol. 12, Page 256*, vol. 12, no. 3, p. 256, Mar. 2025, doi: 10.3390/AEROSPACE12030256.

[2] J. W. Costerton, Z. Lewandowski, D. E. Caldwell, D. R. Korber, and H. M. Lappin-Scott, “Microbial biofilms,” *Annu Rev Microbiol*, vol. 49, pp. 711–745, 1995, doi: 10.1146/ANNUREV.MI.49.100195.003431,.

[3] A. M. Diaz, W. Li, T. D. Irwin, L. M. Calle, and M. R. Callahan, “Investigation of Biofilm Formation and Control for Spacecraft-An Early Literature Review,” 2019.

[4] K. S. Landry, J. M. Morey, B. Bharat, N. M. Haney, and S. S. Panesar, “Biofilms—Impacts on Human Health and Its Relevance to Space Travel,” *Microorganisms 2020, Vol. 8, Page 998*, vol. 8, no. 7, p. 998, Jul. 2020, doi: 10.3390/MICROORGANISMS8070998.

[5] “NASA OSDR: SPACE BIOFILMS.” Accessed: Oct. 16, 2025. [Online]. Available: https://osdr.nasa.gov/bio/repo/data/payloads/Space%20Biofilms

[6] L. Zea *et al.*, “Design of a spaceflight biofilm experiment,” *Acta Astronaut*, vol. 148, pp. 294–300, Jul. 2018, doi: 10.1016/J.ACTAASTRO.2018.04.039.

[7] P. Flores, J. Luo, D. W. Mueller, F. Muecklich, and L. Zea, “Space biofilms – An overview of the morphology of Pseudomonas aeruginosa biofilms grown on silicone and cellulose membranes on board the international space station,” *Biofilm*, vol. 7, p. 100182, Jun. 2024, doi: 10.1016/J.BIOFLM.2024.100182.

[8] P. Flores, S. A. McBride, J. M. Galazka, K. K. Varanasi, and L. Zea, “Biofilm formation of Pseudomonas aeruginosa in spaceflight is minimized on lubricant impregnated surfaces,” *NPJ Microgravity*, vol. 9, no. 1, pp. 1–14, Dec. 2023, doi: 10.1038/S41526-023-00316-W;SUBJMETA.

[9] “ESA - Material matters.” Accessed: Oct. 16, 2025. [Online]. Available: https://www.esa.int/Science_Exploration/Human_and_Robotic_Exploration/Material_matters

[10] “Polymicrobial Biofilm Growth and Control during Spaceflight (Bacterial Adhesion and Corrosion) - NASA Science.” Accessed: Oct. 16, 2025. [Online]. Available: https://science.nasa.gov/biological-physical/investigations/bacterial-adhesion/

[11] “ESA - CubeSats.” Accessed: Oct. 16, 2025. [Online]. Available: https://www.esa.int/Enabling_Support/Preparing_for_the_Future/Discovery_and_Preparation/CubeSats

[12] A. J. Ricco *et al.*, “PHARMASAT: DRUG DOSE DEPENDENCE RESULTS FROM AN AUTONOMOUS MICROSYSTEM-BASED SMALL SATELLITE IN LOW EARTH

ORBIT", Accessed: Oct. 27, 2025. [Online]. Available: http://www.nasa.gov/mission_pages/smallsats

[13] W. W. A. W. Salim *et al.*, "SPORESAT: A NANOSATELLITE PLATFORM LAB-ON-A-CHIP SYSTEM FOR INVESTIGATING GRAVITY THRESHOLD OF FERN-SPORE SINGLE-CELL CALCIUM ION CURRENTS".

[14] A. J. Ricco, S. R. S. Maria, R. P. Hanel, and S. Bhattacharya, "BioSentinel: A 6U Nanosatellite for Deep-Space Biological Science," *IEEE Aerospace and Electronic Systems Magazine*, vol. 35, no. 3, pp. 6–18, Mar. 2020, doi: 10.1109/MAES.2019.2953760.

[15] J. Maule *et al.*, "Rapid culture-independent microbial analysis aboard the International Space Station (ISS)," *Astrobiology*, vol. 9, no. 8, pp. 759–775, Oct. 2009, doi: 10.1089/AST.2008.0319;SUBPAGE:STRING:ABSTRACT;REQUESTEDJOURNAL:JOURNAL:AST;JOURNAL:JOURNAL:AST;WGROUP:STRING:PUBLICATION.

[16] D. Calabria *et al.*, "AstroBio-CubeSat: A lab-in-space for chemiluminescence-based astrobiology experiments," *Biosens Bioelectron*, vol. 226, p. 115110, Apr. 2023, doi: 10.1016/J.BIOS.2023.115110.

[17] M. Möndel *et al.*, "Probiotic E. coli treatment mediates antimicrobial human β-defensin synthesis and fecal excretion in humans," *Mucosal Immunol*, vol. 2, no. 2, pp. 166–172, Mar. 2009, doi: 10.1038/MI.2008.77.

[18] C. Zimmer and C. Dorea, "Enumeration of Escherichia coli in Probiotic Products," *Microorganisms 2019, Vol. 7, Page 437*, vol. 7, no. 10, p. 437, Oct. 2019, doi: 10.3390/MICROORGANISMS7100437.

[19] M. Hanot, E. Lohou, and P. Sonnet, "Anti-Biofilm Agents to Overcome Pseudomonas aeruginosa Antibiotic Resistance," *Pharmaceuticals 2025, Vol. 18, Page 92*, vol. 18, no. 1, p. 92, Jan. 2025, doi: 10.3390/PH18010092.

[20] M. T. T. Thi, D. Wibowo, and B. H. A. Rehm, "Pseudomonas aeruginosa Biofilms," *International Journal of Molecular Sciences 2020, Vol. 21, Page 8671*, vol. 21, no. 22, p. 8671, Nov. 2020, doi: 10.3390/IJMS21228671.

[21] O. SHIMOMURA, F. H. JOHNSON, and Y. SAIGA, "Extraction, purification and properties of aequorin, a bioluminescent," *J Cell Comp Physiol*, vol. 59, no. 3, pp. 223–239, Jun. 1962, doi:

10.1002/JCP.1030590302;JOURNAL:JOURNAL:15530809;WGROUP:STRING:PUBLICATION.

[22] A. B. Cubitt, R. Heim, S. R. Adams, A. E. Boyd, L. A. Gross, and R. Y. Tsien, "Understanding, improving and using green fluorescent proteins," *Trends Biochem Sci*, vol. 20, no. 11, pp. 448–455, Nov. 1995, doi: 10.1016/S0968-0004(00)89099-4.

[23] R. Y. Tsien, "The green fluorescent protein," *Annu Rev Biochem*, vol. 67, no. Volume 67, 1998, pp. 509–544, Jul. 1998, doi: 10.1146/ANNUREV.BIOCHEM.67.1.509/CITE/REFWORKS.

[24] B. P. Cormack, R. H. Valdivia, and S. Falkow, "FACS-optimized mutants of the green fluorescent protein (GFP)," *Gene*, vol. 173, no. 1, pp. 33–38, Jan. 1996, doi: 10.1016/0378-1119(95)00685-0.

[25] N. C. Shaner, R. E. Campbell, P. A. Steinbach, B. N. G. Giepmans, A. E. Palmer, and R. Y. Tsien, "Improved monomeric red, orange and yellow fluorescent proteins derived from Discosoma sp. red fluorescent protein," *Nat Biotechnol*, vol. 22, no. 12, pp. 1567–1572, Dec. 2004, doi: 10.1038/NBT1037;KWRD=LIFE+SCIENCES.

[26] R. Heim, D. C. Prasher, and R. Y. Tsien, "Wavelength mutations and posttranslational autoxidation of green fluorescent protein," *Proc Natl Acad Sci U S A*, vol. 91, no. 26, pp. 12501–12504, Dec. 1994, doi: 10.1073/PNAS.91.26.12501.

[27] L. Yuan, H. Straub, L. Shishaeva, and Q. Ren, "Microfluidics for Biofilm Studies," *Annual Review of Analytical Chemistry*, vol. 16, no. Volume 16, 2023, pp. 139–159, Jun. 2023, doi: 10.1146/ANNUREV-ANCHEM-091522-103827/CITE/REFWORKS.

[28] N. Bourguignon, V. Kamat, M. Perez, K. Mathee, B. Lerner, and S. Bhansali, "New dynamic microreactor system to mimic biofilm formation and test anti-biofilm activity of nanoparticles," *Appl Microbiol Biotechnol*, vol. 106, no. 7, pp. 2729–2738, Apr. 2022, doi: 10.1007/S00253-022-11855-9/TABLES/1.

[29] "Quantitative and Qualitative Assessment Methods for Biofilm Growth: A Mini-review - PubMed." Accessed: Oct. 01, 2025. [Online]. Available: https://pubmed.ncbi.nlm.nih.gov/30214915/

[30] A. Menichetti, D. Mordini, and M. Montalti, "Melanin as a Photothermal Agent in Antimicrobial Systems," *International Journal of Molecular Sciences 2024, Vol. 25, Page 8975*, vol. 25, no. 16, p. 8975, Aug. 2024, doi: 10.3390/IJMS25168975.

[31] A. Mavridi-Printezi, M. Guernelli, A. Menichetti, and M. Montalti, “Bio-Applications of Multifunctional Melanin Nanoparticles: From Nanomedicine to Nanocosmetics,” *Nanomaterials 2020, Vol. 10, Page 2276*, vol. 10, no. 11, p. 2276, Nov. 2020, doi: 10.3390/NANO10112276.

[32] K. Y. Ju, Y. Lee, S. Lee, S. B. Park, and J. K. Lee, “Bioinspired Polymerization of Dopamine to Generate Melanin-Like Nanoparticles Having an Excellent Free-Radical-Scavenging Property,” *Biomacromolecules*, vol. 12, no. 3, pp. 625–632, Mar. 2011, doi: 10.1021/BM101281B.

[33] G. Horneck, D. M. Klaus, and R. L. Mancinelli, “Space microbiology,” *Microbiol Mol Biol Rev*, vol. 74, no. 1, pp. 121–156, Mar. 2010, doi: 10.1128/MMBR.00016-09.

[34] A. Menichetti, D. Mordini, and M. Montalti, “Polydopamine Nanosystems in Drug Delivery: Effect of Size, Morphology, and Surface Charge,” *Nanomaterials 2024, Vol. 14, Page 303*, vol. 14, no. 3, p. 303, Feb. 2024, doi: 10.3390/NANO14030303.

[35] N. T. Le Na, B. T. Van Khanh, P. Xuan Huy, H. T. M. Nhung, N. Thi Van Anh, and N. D. Thang, “Melanin biomaterial effectively eliminates bacteria from water and synergistically induces melanoma-cell death during X-ray irradiation,” *Materials Technology*, vol. 36, no. 5, pp. 261–269, Apr. 2021, doi: 10.1080/10667857.2020.1747808.

[36] L. N. Nguyen Thi *et al.*, “Protective effect of melanin nanoparticles created from squid ink against irradiation on human keratinocytes,” *J Nanostructure Chem*, vol. 14, no. 3, pp. 233–244, Jun. 2024, doi: 10.1007/S40097-022-00513-1/FIGURES/7.

# *Chapter 7*

## *Conclusions and future perspectives*

This doctoral work has provided an in-depth exploration of biosensor technology, underscoring its remarkable potential to impact different areas such as clinical diagnostics, food safety, and astrobiology.

The success of glucose sensors and lateral flow tests since the 1980s has spurred a transition in biosensing research toward developing compact, user-friendly diagnostic devices. By investigating the principles, development methods, and applications of biosensors, this thesis contributes to the evolving landscape of this technology. Significant advances in biosensor technology have been driven by the creation of innovative sensing platforms, the incorporation of novel materials such as paper and hydrogels, and the application of advanced fabrication methods including wax printing and 3D printing. Additionally, the exploration of state-of-the-art signal transduction mechanisms, such as chemiluminescence and electrochemiluminescence, has played a crucial role in enhancing device sensitivity, specificity, and overall performance. The knowledge acquired from these developments continues to inform efforts to optimize biosensors for practical, real-world applications.

Despite these achievements, numerous research opportunities remain. The rapid progress in fields such as nanotechnology, materials science, and biotechnology provides a fertile ground for further improvements in biosensor functionality. Moreover, integrating biosensors into wearable devices opens possibilities for continuous, real-time monitoring across multiple contexts. Biosensors are also gaining attention in astrobiology, where they hold promise for detecting biomarkers and monitoring environmental conditions in extraterrestrial settings.

Finally, translating these technologies from laboratory prototypes to commercially viable products necessitate addressing practical challenges related to miniaturization, reproducibility, and cost efficiency. Looking ahead, future research must strive to bridge this gap, transforming promising biosensor innovations into practical solutions that directly benefit society. Ultimately, biosensors are not merely scientific tools, they are instruments of progress, driving us toward a healthier, safer, and more sustainable world.